

**Widely tunable on-chip microwave circulator for
superconducting quantum circuits**

by

Benjamin J. Chapman

B.A., Dartmouth College, 2009

M.S., University of Colorado, 2015

A thesis submitted to the
Faculty of the Graduate School of the
University of Colorado in partial fulfillment
of the requirements for the degree of
Doctor of Philosophy
Department of Physics

2017

This thesis entitled:
Widely tunable on-chip microwave circulator for superconducting quantum circuits
written by Benjamin J. Chapman
has been approved for the Department of Physics

Konrad W. Lehnert

John Price

Date _____

The final copy of this thesis has been examined by the signatories, and we find that both the content and the form meet acceptable presentation standards of scholarly work in the above mentioned discipline.

Chapman, Benjamin J. (Ph.D., Physics)

Widely tunable on-chip microwave circulator for superconducting quantum circuits

Thesis directed by Prof. Konrad W. Lehnert

This thesis develops theory for and experimentally demonstrates a new way to break Lorentz reciprocity—the symmetry, in an electrical network, under exchange of source and detector. The approach is based on the sequential application of frequency conversion and delay; as frequency and time are Fourier duals, these operations do not generally commute. We apply this method in the construction of an on-chip superconducting microwave circulator, a critical component for the unidirectional routing of quantum information in superconducting networks. The device requires neither permanent magnets nor microwave control tones, allowing on-chip integration with other superconducting circuits without expensive control hardware. Isolation in the device exceeds 20 dB over a bandwidth of tens of MHz, and its insertion loss is small, reaching as low as 0.9 dB at select operation frequencies. Furthermore, the device is linear with respect to input power for signal powers up to many hundreds of fW ($\approx 10^3$ circulating photons), and the direction of circulation can be dynamically reconfigured. We demonstrate its tunability with operation at a selection of frequencies between 4 and 6 GHz. Given the current status of quantum error-correction and architectures for quantum information processing with superconducting circuits, such scalable non-reciprocal devices will almost certainly be necessary for construction of a superconducting quantum computer intended to be more than a proof-of-principle.

Dedication

For my sister, Ellie, and my parents, Frankie and Bill.

Acknowledgements

I benefited from the help of a great many people during the course of this thesis. It would be impractical to recognize now all of those sources of support; I am blessed with thoughtful colleagues and friends, and singularly blessed in family. Here there is space only to acknowledge those that have been central to this project.

First, I would like to thank my undergraduate advisors, Alex Barnett and Miles Blencowe, as well as the NMR group at Schlumberger-Doll Research, in particular Pabitra Sen and Martin Hürlimann, for their encouragement to attend graduate school and their patience with a fledgling physicist.

I am also obliged to two of our group's former graduate students, Will Kindel and Adam Reed, for speaking with me about joining Konrad's lab, and helping me learn the basics of microwave engineering. When I arrived, I was fortunate to begin work immediately on the circulator project with post-doc Joe Kerckhoff. I am indebted to Joe not only for the rich intellectual ground in which the work is planted, but also for his mentorship.

Collaboration with the Quantum Devices group at NIST gave a tangible form to our many hours of design. Leila Vale fabricated the circuits and Gene Hilton and Ben Mates shared their expertise in superconducting circuit layout. Kent Irwin and Dale Li also shared with us their considerable experience in this field.

Much of the device design and testing was done in the last two years, with help from my lab mate Eric Rosenthal. Eric's creativity and energy have amplified our progress on the project. More broadly, I would like to acknowledge all of my lab mates. The open culture of ideas, the readiness

of others to offer help or advice, and the general sense of camaraderie make it a pleasure to work here.

Finally, I would like to thank my advisor Konrad. It's difficult for me to express how grateful I am for the chance to work with him. Rather than attempt in this public setting, I will just say "Konrad: thank you."

Contents

Chapter

1	Introduction	1
2	Quantum information processing	6
2.1	The road to quantum computation	7
2.2	Quantum error correction and hardware architectures	8
2.3	Circuit quantum electrodynamics	10
3	Lorentz reciprocity	15
3.1	The scattering matrix	16
3.2	The Lorentz reciprocity theorem	18
3.3	Methods for breaking Lorentz reciprocity	20
3.3.1	Magneto-optic devices	20
3.3.2	Nonlinear devices	22
3.3.3	Active devices	23
3.3.4	Connection with time-reversal symmetry	27
3.4	Common non-reciprocal devices	28
3.4.1	Gyrators	28
3.4.2	Isolators	29
3.4.3	Circulators	29

4	Theory of operation	31
4.1	Model system	31
4.2	Superconducting implementation	34
4.2.1	Multiplying elements	34
4.2.2	Delays	37
4.2.3	Assembly of the full circulator	38
4.3	Circuit analysis	40
5	Circulator Layout	45
5.1	Design philosophy	45
5.2	The Nb/ AlO_x /Nb trilayer process	46
5.2.1	Josephson junctions in the trilayer process	48
5.2.2	SQUID arrays in the trilayer process	49
5.2.3	Additional wiring layers	51
5.2.4	Best practices for trilayer process layout	52
5.3	Design considerations	54
5.3.1	Capacitor design	54
5.3.2	Use of normal metal	56
5.3.3	Bias line design	58
5.4	Design iterations	61
5.4.1	Generation I.	61
5.4.2	Generation II.	64
5.4.3	Generation III.	69
5.4.4	Generation IV.	73
6	Experimental results	77
6.1	Experimental setup	77
6.2	Tune-up procedure	77

6.3	Performance	81
6.4	Discussion	86
6.4.1	Device limitations and deviation from theoretical models	86
6.4.2	Comparison with the fourth-generation, version b device	89
6.4.3	Filtering, attenuation, and power-consumption considerations, in the context of scaling	91
7	Conclusion and Outlook	94
	Bibliography	98
	Appendix	
A	Graph theory eigenfrequency analysis for a half-circulator	110
B	Design rules of the NIST Nb trilayer process	115
C	Measurement details	119
D	Calibration of network parameter measurements	121
D.1	Transmission calibration	121
D.2	Reflection calibration	121
D.3	Calibration of group delay	122

Tables

Table

3.1	Symbols and scattering matrices for three common non-reciprocal devices	28
5.1	Layer stackup for the NIST niobium trilayer process	47
5.2	Design features and performance of the first-generation circulator	63
5.3	Design features and performance of the second-generation circulator	65
5.4	Design features and performance of the third-generation circulator	71
5.5	Design features and performance of the fourth-generation circulator	75
5.6	Design features and performance of the alternate design of the fourth-generation circulator	75
6.1	Power budget for an active circulator	93
B.1	Design rules of the NIST niobium trilayer process	115

Figures

Figure

1.1	A single-mode Fabry-Perot cavity exhibits a fundamental challenge of precision measurement: isolating the experimental system from the environment, while maintaining the ability to rapidly control or measure it	2
2.1	The path to fault-tolerant quantum computation	7
2.2	Signal-routing of a circulator	12
2.3	Schematic illustrating a simplified measurement setup for readout of a superconducting qubit in the circuit quantum electrodynamics architecture	13
3.1	Diagram illustrating a bounded network which electromagnetic signals can enter or exit through guided modes	16
3.2	Faraday rotation and optically active media	21
3.3	Requirements for non-reciprocity in cascades of linear systems	23
4.1	Model system which demonstrates gyration with frequency-conversion and delay	32
4.2	Superconducting lumped-element implementation of multipliers and delays	35
4.3	Model system realized as a lumped-element network of capacitors and dynamically tunable inductors	39
4.4	Schematic for a circuit analysis of the circulator	41
5.1	Josephson junctions in the Niobium trilayer process	48

5.2	Layer stack-up of SQUIDs in the Niobium trilayer process	50
5.3	Layout of SQUIDs in the Niobium trilayer process	51
5.4	Capacitor design	55
5.5	Effect of normal metal on the stability of a circulator’s resonant modes	57
5.6	Bridge circuit design	59
5.7	Optical micrograph of the first-generation circulator	62
5.8	Hysteresis in the first-generation circulator with respect to sweep-direction of bias currents	63
5.9	AC modulation of the first-generation circulator	66
5.10	Optical micrograph of the second-generation circulator	67
5.11	Performance of the second-generation circulator	68
5.12	Angular dependence of the “edge” feature in the second-generation circulator	70
5.13	Optical micrograph of the third-generation circulator	72
5.14	Performance of the third generation circulator	73
5.15	Optical micrograph of the fourth-generation circulator	74
5.16	Optical micrograph of the alternate design of the fourth-generation circulator	76
6.1	Experimental schematic for circulator measurements	78
6.2	Measurements of the circulator’s tunable resonant-delay	79
6.3	A dynamically reconfigurable circulator	80
6.4	Scattering parameter measurements	82
6.5	Circulator tunability	84
6.6	Circulator theory and experiment	87
6.7	Scattering parameters of the fourth-generation circulator, version b	89
6.8	Performance of the fourth-generation circulator, version b	90
7.1	Schematic for a lossless broadband superconducting circulator	96

A.1 Analytical circuit analysis of a half circulator 111

C.1 Detailed experimental schematic 119

List of Symbols

The tables below catalogue the symbols used throughout this thesis. They are organized by the chapters in which the symbols are introduced (and not the chapters in which the symbols appear). For example, k_B is introduced as Boltzmann's constant in Chapter 2 and appears only in the table of symbols for Chapter 2, despite being used in later chapters as well. Although efforts were made to keep notation unambiguous, some symbols are used to represent different quantities in different chapters.

Chapter 1

T_l	transmission of the left mirror in Fig. 1.1
T_r	transmission of the right mirror in Fig. 1.1
a	annihilation operator for the cavity mode in Fig. 1.1
a_{in}	incoming field in Fig. 1.1
a_{out}	outgoing field in Fig. 1.1
κ	external coupling rate for the cavity mode in Fig. 1.1
ω_c	resonant frequency of the the cavity mode in Fig. 1.1

Chapter 2

k_B	Boltzmann's constant
T	temperature
\hbar	Planck's constant divide by 2π
ω	frequency scale for a weakly anharmonic microwave resonator

ω_q	transmon qubit frequency (frequency separation between the ground and first excited states of the transmon)
ω_r	frequency of the microwave resonator coupled to the transmon qubit
a	annihilation operator for the microwave resonator coupled to the transmon qubit
σ_z	Pauli z operator for the transmon qubit
χ	frequency scale for the dispersive coupling between the transmon qubit and the microwave resonator

Chapter 3

Ω_s	surface that bounds the network in Fig. 3.1
μ	mode index for the guided modes in Fig. 3.1
$E_{T,\mu}$	component of the electric field tangential to the waveguide carrying the μ^{th} guided mode
$H_{T,\mu}$	component of the magnetic field tangential to the waveguide carrying the μ^{th} guided mode
$e_{T,\mu}$	component of the electric field tangential to the waveguide carrying the μ^{th} guided mode with transverse dependence
$h_{T,\mu}$	component of the magnetic field tangential to the waveguide carrying the μ^{th} guided mode with transverse dependence
a_μ	complex amplitude of the wave travelling into the network in the μ^{th} waveguide
b_μ	complex amplitude of the wave travelling out of the network in the μ^{th} waveguide
β_μ	propagation constant for the μ^{th} guided mode
$\delta_{\mu\nu}$	the Kronecker delta
P	the net power entering the network in Fig. 3.1

\mathbf{S}	the scattering matrix
\mathbf{a}'	excitation state of a first hypothetical scattering process
\mathbf{a}''	excitation state of a second hypothetical scattering process
\mathbf{b}'	output state of a first hypothetical scattering process
\mathbf{b}''	output state of a second hypothetical scattering process
\mathbf{E}'	electric field of a first hypothetical scattering process
\mathbf{E}''	electric field of a second hypothetical scattering process
\mathbf{H}'	magnetic field of a first hypothetical scattering process
\mathbf{H}''	magnetic field of a second hypothetical scattering process
$\boldsymbol{\mu}(\mathbf{H})$	magnetic permeability tensor
$\boldsymbol{\epsilon}(\mathbf{E})$	electric permittivity tensor
ω	frequency of the harmonic fields
A	a general linear system
B	a second general linear system
h_A	impulse response of A
h_B	impulse response of B
u	initial state of a linear system
y	intermediate state of a linear system
z	final state of a linear system
$t, 't', \eta, \eta', \xi$	various variables for time
h_{BA}	impulse response for the composite-system formed by the cascade of systems A and B
h_{AB}	impulse response for the composite-system formed by the cascade of systems B and A
ω_i	resonant frequency of the i^{th} mode in a system of parametrically-coupled resonant modes

κ_i	linewidth of the i^{th} mode in a system of parametrically-coupled resonant modes
H_I	interaction Hamiltonian for a system of parametrically coupled modes in the resolved sideband limit
θ	phase of the beamsplitter interaction between modes i and j
a_i	annihilation operator for the i^{th} mode in a system of parametrically-coupled resonant modes

Chapter 4

ω_p	frequency of the input microwave field
Ω	frequency of bias signal for the multiplying elements
θ	phase of a multiplying element's bias signal
τ	duration of the delay provided by the delay element
l_+	inductance of one pair of inductors in a tunable inductive bridge
l_-	inductance of a second pair of inductors in a tunable inductive bridge
δ	imbalance parameter for a tunable inductive bridge
l_0	base inductance parameter for a tunable inductive bridge
c	capacitance of the capacitor in Fig. 4.2b
Φ_u	uniform magnetic flux created by an off-chip magnetic coil, used to tune an inductive bridge realized with SQUIDs
Φ_g	gradiometric magnetic flux created by an on-chip bias line, used to tune an inductive bridge realized with SQUIDs
Z_0	characteristic impedance of a transmission line
ω	angular frequency of an input microwave tone
i	$\sqrt{-1}$
l	inductance of an N SQUID array threaded by magnetic flux Φ
N	number of SQUIDs in an array with inductance l

Φ	flux threading the SQUIDs in an array with inductance l
φ_0	reduced flux quantum $\hbar/(2e)$
I_0	Josephson junction critical current
ϕ	phase of the gradiometric bias flux
δ_0	amplitude of the sinusoidally varying imbalance parameter δ
α	$\pi\Phi_u/\Phi_0$
β	$\pi\Phi_g/\Phi_0$
Φ_0	the flux quantum $2\pi\varphi_0 = h/(2e)$
J_n	the n^{th} Bessel function of the first kind
\angle	phase (of a complex number)
ω_0	resonant frequency of the resonant delay
I_i	current through port i
ϕ_i	branch flux across port i
$I_{1,e}$	even current through the left port
$I_{1,o}$	odd current through the left port
$I_{r,e}$	even current through the right port
$I_{r,o}$	odd current through the right port
$\phi_{1,e}$	even branch flux through the left port
$\phi_{1,o}$	odd branch flux through the left port
$\phi_{r,e}$	even branch flux through the right port
$\phi_{r,o}$	odd branch flux through the right port
I_+	co-rotating current through ports q and p
I_-	counter-rotating current through ports q and p
ϕ_+	co-rotating branch flux through ports q and p
ϕ_-	counter-rotating branch flux through ports q and p
A, B, C, D	block matrices
Y	admittance matrix

\mathbf{S}_o	odd scattering matrix
\mathbf{S}_e	even scattering matrix
\mathbf{U}	unitary (change-of-basis) matrix that transforms between numbered ports and left/right, even/odd ports

Chapter 5

ϵ_r	relative permittivity of the silicon wafer in the NIST Nb trilayer process
T_c	transition temperature of a superconductor
L	inductance of a superconducting loop
B_0	magnitude of a magnetic field
w	width of a microstrip
e	electron charge
Q	quality factor
l	length of a resistor parallel to the direction of current flow
ξ_c	“clean” coherence length
l_n	mean free path
v_F	Fermi velocity
ξ_d	“dirty” coherence length
I_n	critical current of an SNS tunnel junction
R_n	room-temperature resistance of an SNS junction
l_ϕ	inelastic scattering length
E_J	Josephson energy of an SNS junction
R	low-temperature resistance of an SNS junction
Ω	frequency of the on-chip gradiometric flux lines
I_{ind}	current induced in the microwave lines by the RF bias signals
M_A	mutual inductance between a bias line and a large circuit loop
M_a	mutual inductance between a bias line a SQUID loop

A	area of a large circuit loop
a	area of a SQUID loop
\mathcal{E}	EMF around a large circuit loop
I_g	current amplitude in the on-chip bias line
p	participation ratio for the large circuit loop
Z_A	impedance of the large circuit loop
I_s	critical current of a SQUID
B_g	magnetic field created by the shielded, on-chip bias line
r	distance from the shielded bias line
ϵ	separation between the inner and outer lines in the shielded configuration
Φ_g^{edge}	amplitude of gradiometric flux where the “edge” feature appears

Chapter 6

$\tilde{\Phi}_u$	effective uniform magnetic flux used for the predictions in Fig. 6.2
R	reflection coefficient
T	transmission coefficient
g	frequency splitting of the circulator’s resonant modes
S_I^{AN}	sideband noise power caused by amplitude fluctuations of the gradiometric flux
S_I^{PN}	sideband noise power caused by phase fluctuations of the gradiometric flux
$I_{1\text{dB}}$	signal current in the device at its 1 dB compression point
S_I	Johnson noise current spectral density
n	photons of added noise

Chapter 7

Z_m	impedance transformer in Fig. 7.1
T	modulation period $2\pi/\Omega$

Appendix A

I_i	current in the i^{th} element of Fig. A.1
V_i	voltage in the i^{th} element of Fig. A.1
\mathbf{V}_b	vector of branch voltages
\mathbf{V}_c	vector of chord voltages
\mathbf{I}_b	vector of branch currents
\mathbf{I}_c	vector of chord currents
r	resistance of the resistors in Fig. A.1
l_1	inductance of the first kind of inductors in Fig. A.1
l_2	inductance of the second kind of inductors in Fig. A.1
c	capacitance of the capacitors in Fig. A.1
\mathbf{F}	matrix relating chord currents to branch currents through Kirchoff's current law
\mathbf{Z}_b	matrix of branch impedances
\mathbf{Z}_c	matrix of chord impedances
s	Laplace variable
s_i	i^{th} eigenfrequency of the circuit

Appendix C

T_n	Noise temperature of the input lines
-------	--------------------------------------

Appendix D

R_{bal}	measured reflection of the circulator when all bridges are balanced
G	gain of the reflection measurement chain
Γ_{bal}	reflection coefficient of the circulator when all bridges are balanced
\mathbf{S}_{bal}	scattering matrix of the circulator when all bridges are balanced

l	effective inductance of one arm of an inductive bridge in the circulator's balanced (unbiased) state
R_{op}	measured reflection during operation
Γ_{op}	reflection coefficient during operation
τ	duration of the circulator's resonant delay
τ_d	electrical delay of the measurement chain

Chapter 1

Introduction

The idea to use quantum systems for computation was first proposed in the 1980s by notable scientists such as Feynman [1, 2] and Deutsch [3, 4]. The notion gained major traction in 1994 when Peter Shor showed how such a machine could efficiently factor composite integers [5]. (The RSA encryption scheme [6]—a widely utilized encryption method for commerce and other forms of sensitive communication—is founded on the difficulty of this task.) Factoring large composite integers is but one example from a list of difficult problems that could be solved by these efforts: others include efficient search algorithms [7], quantum chemistry and catalyst design [8, 9, 10], and communication whose security is guaranteed by physical laws [11]. For these reasons, efforts to create analog and digital quantum computers, quantum simulators, and quantum annealers span many realms of physics.

Across all of the proposed platforms for constructing a quantum computer, one of the key challenges is engineering a quantum system which is both well isolated from its environment (to protect it from dissipation and decoherence) *and* rapidly measurable (and controllable). This challenge is not unique to problems specific to quantum computing; rather, its roots extend into the theory of quantum measurements. According to Heisenberg, measurements of a system are perturbing, as illustrated famously (and controversially) by his microscope thought experiment [12].

The problem is also present in purely classical systems. Heuristically, oscillators that interact weakly with their environment respond slowly to control fields, and oscillators that respond quickly to control fields rapidly dissipate energy into their environment. This is no conspiracy: from the

perspective of the oscillator, the experimentalist is a part of the environment.

To illustrate this issue more quantitatively, consider a system formed by a single electromagnetic mode in a Fabry-Perot cavity, where the left mirror is perfectly reflective (vanishing transmission) and the right mirror has a transmission T_r (Fig. 1.1). The quantum Langevin equations

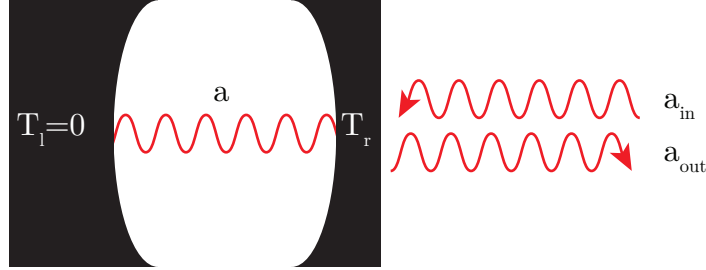


Figure 1.1: A single electromagnetic mode in a Fabry-Perot cavity, characterized by the annihilation operator a . The left mirror is perfectly reflective, and the right mirror has transmission T_r , which couples the cavity mode to an incoming field a_{in} and an outgoing field a_{out} .

that describe the time-evolution of the cavity field a and the outgoing field a_{out} are [13]

$$\dot{a} = i\omega_c a - \frac{\kappa}{2}a + \sqrt{\kappa}a_{in} \quad (1.1)$$

$$a_{out} = \sqrt{\kappa}a - a_{in}. \quad (1.2)$$

Here, ω_c is the frequency of the cavity mode, and κ is a rate determined by T_r which describes the coupling between the cavity and the incoming and outgoing fields a_{in} and a_{out} .

In this example, the cavity mode is the system of interest, which an experimentalist may hope to study via measurements of the outgoing field a_{out} . The prospects for that aspiration can be understood by examination of two limiting cases, in which the transmission of the right mirror is small or large.

When T_r approaches 0, the coupling rate κ also vanishes. This is beneficial from the perspective of isolating the system of interest from its environment: the dynamics of the cavity mode, given in Eq. (1.1), are now uncoupled from the external field a_{in} . Unfortunately, the experimentalist has also forfeited the ability to infer the state of the cavity from measurements of the outgoing field a_{out} (Eq. (1.2)).

In the opposite limit where T_r is large, κ may become non-negligible with respect to the cavity frequency ω_c . The outgoing field now contains considerable information about the state of the cavity mode. The cost of this encoding, however, is that the time-evolution of the cavity mode is now subject to the “slings and arrows” of the environment, in the form of the incoming field a_{in} .

The link between the environment’s effect on the cavity mode (through a_{in}) and the cavity mode’s radiation into the environment (through a_{out}) is an instance of the fluctuation-dissipation theorem [14, 15]. The right mirror’s transmission creates dissipation in the cavity mode (which may be measured and recorded by an experimentalist) but also causes fluctuations in the mode, driven by the incoming field.

As an aside, we note that in this example, measurement of the cavity state requires that it decays into a propagating mode. This is not a general requirement for measurement of a quantum system. For example, quantum non-demolition measurements [16, 17] allow measurement without dissipation [18]. Measurements are not necessarily accompanied by dissipation; they are accompanied by disturbance.

Returning to the measurement of the cavity mode, the examined limiting cases of large and small κ suggest that our measurement dilemma cannot be resolved by optimization of the cavity’s parameters. The solution is external, and involves directing the outgoing field a_{out} to the measurement apparatus, while ensuring that the incoming field a_{in} is supplied by a very cold bath. In a classical analysis, this strategy can protect the cavity mode from its environment, while still allowing an experimentalist to study the state of the mode. Quantum mechanically, vacuum fluctuations persist even at zero temperature. But the influence of these vacuum fluctuations on the cavity’s dynamics are small compared to, for example, the black-body radiation of the measurement apparatus.

In the vacuum of free-space, however, Maxwell’s equations make this kind of directional signal routing impossible. Practically, an interaction between electromagnetic waves and matter is required to separate signals based on their direction of propagation. Devices which do so are called non-reciprocal, in reference to their violation of Lorentz reciprocity [19]. In the context of

quantum networks, non-reciprocal devices serve a variety of purposes beyond the fundamental one described above. For example, they enable protocols for the generation of remote entanglement [20, 21, 22] and proposals for the construction of rich quantum many-body systems [23] that rely on directional signal routing, and allow for the use of quantum-limited reflection amplifiers [24, 25]. Such applications impose a strict set of design constraints: for quantum measurements, the ideal non-reciprocal device has no loss and no added noise. These requirements make familiar non-reciprocal devices like diodes and op-amps unsuitable for use with quantum systems.

More broadly, enforcing the unidirectional flow of energy and information is a critical signal processing primitive in a variety of networks. A common use in telecommunication networks, for instance, is antennae duplexing, in which the incoming and outgoing signals from an antenna are separated, allowing for simultaneous transmission and reception. Given their utility, it should come as no surprise that commercial non-reciprocal devices have been developed across the electromagnetic spectrum, and are widely used in a variety of experimental contexts. For example, in experiments on quantum superconducting circuits—one of the most promising platforms for the development of a quantum computer—non-reciprocal devices are ubiquitous. State-of-the-art commercial non-reciprocal devices, however, are constructed with large permanent magnets and gyrotropic media, precluding their miniaturization for on-chip applications, as well as their construction with superconducting materials.

The optimal architecture for a quantum computer built with superconducting circuits is very much still an open research question. The surface code, though, is one of the leading contenders, and would require over a hundred million physical qubits to accomplish the task [26].¹ As each of these qubits must be simultaneously shielded from its environment and controlled in hardware, the need for a scalable non-reciprocal technology is pressing.

To address that need we have developed an alternative method for routing propagating electromagnetic fields with minimal loss or added noise, which uses no permanent magnets and can be

¹ This estimate is for a computer that could execute a practical quantum computation—in this case, Shor’s algorithm on an integer with 600 digits—in approximately one day.

integrated on-chip with superconducting circuits in a scalable way. In this thesis we describe the design, construction, and measurement of a non-reciprocal device which is based on this method.

Design goals for the circuit were set with a superconducting qubit application in mind, and in the context of modular quantum networks. But the device will also find use in other low-temperature microwave networks, especially ones which require high measurement efficiency. Examples include rapid single flux quantum logic [27]; microwave kinetic inductance detectors [28], transition edge sensors [29] and other astronomical detector arrays; dark-matter searches [30]; and tests of Lorentz invariance with high-quality microwave resonators [31].

The structure of the thesis is as follows: Ch. 2 gives a brief overview of quantum information processing, and efforts to process quantum information with superconducting circuits, broadly referred to as circuit quantum electrodynamics. The assumptions and consequences of the Lorentz reciprocity theorem are discussed in Ch. 3, along with other proposals and demonstrations for creating non-reciprocal devices. Ch. 4 describes the theory of operation for our device, and Ch. 5 describes its realization as a superconducting circuit, as well as relevant layout considerations. Experimental results are summarized in Ch. 6. Finally, conclusions and an outlook for the work are presented in Ch. 7.

Chapter 2

Quantum information processing

The enormous computational power of a quantum processor has attracted interest from a variety of subfields within physics and other disciplines. In the atomic domain, work is underway to store quantum bits of information (qubits) in the electronic states of trapped ions and Rydberg atoms. Notable solid-state platforms include nitrogen (and other) vacancy centers, in which information is encoded in the composite spin of the vacancy; semiconductor quantum dots, where the qubit is formed by the singlet state and the projection-less triplet state of two confined electron spins; and superconducting circuits, where information is stored in the ground or first excited state of an anharmonic microwave circuit. Many other platforms are also being investigated (optical, NMR, etc); Refs. [32, 33] provide a high-level overview of these approaches. Even within the experimental systems noted above, there exist a variety of ways to encode a bit of quantum information.¹ More exotic proposals also exist, in which the braiding of topological excitations with non-Abelian statistics provides the basis for computation [37]. While the listed platforms and physical realizations of a qubit are intended to be representative of the field's breadth, they are far from exhaustive.

¹ For example, some researchers in the field of superconducting circuits use microwave resonators as the memory elements, and construct the computational basis $\{|0\rangle = |\alpha\rangle + |-\alpha\rangle, |1\rangle = |i\alpha\rangle + |-i\alpha\rangle\}$ with even superpositions of coherent states $|\alpha\rangle$ —so-called cat codes [34], named for the cat states [35] that comprise them. Other resonator-based schemes also exist; Ref. [36] provides an overview and comparison of several prominent codes.

2.1 The road to quantum computation

Across all of these platforms, however, the ultimate goal of fault-tolerant quantum computation is shared. Fig. 2.1, from Ref. [38], illustrates one conception of the path to this goal.

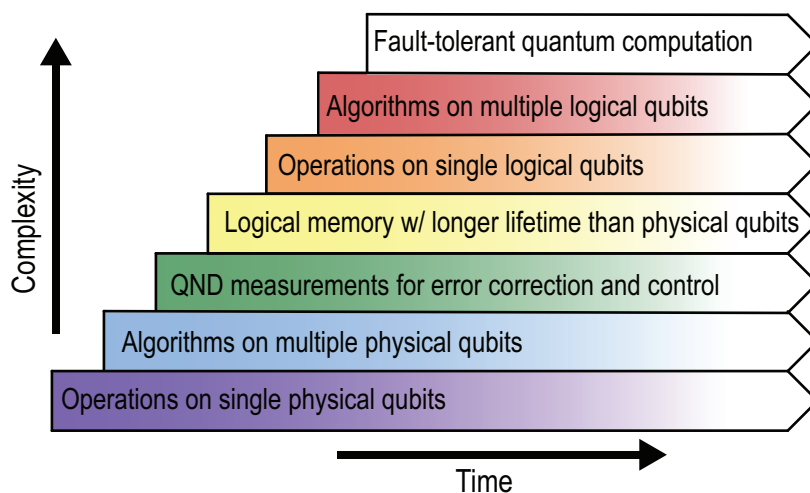


Figure 2.1: One conception for the path to fault-tolerant quantum computation, divided into seven steps. The y-axis of the graphic illustrates the relative complexity of each stage—advancing along the path requires mastery of the previous steps. The x-axis, time, indicates that active efforts to improve at each stage are ongoing. After [38].

The first step involves operations (also known as gates) on single physical qubits. This is followed by algorithms (long sequences of gates) on multiple physical qubits. Completing these initial two steps requires satisfaction of the first five DiVincenzo criteria [39] (a list of five necessary conditions for constructing a quantum computer, plus two additional conditions for quantum communication). Following this is a more advanced stage, requiring quantum non-demolition (QND) measurements of qubits and advanced control. This stage enables, for example, QND measurements of error syndromes like parity, and the stabilization of arbitrary quantum states. Demonstrations of this third stage have been made with trapped-ions [40], Rydberg atoms [41], Nitrogen vacancy centers [42], and superconducting qubits [43, 44, 45].

The fourth step is the creation of a logical memory with a lifetime that exceeds the physical qubits which comprise it. This step, which entails encoding information redundantly among mul-

multiple physical qubits and actively correcting for errors in that encoding, is critical, as it allows the preservation of quantum information for timescales long enough to enable meaningful computation. Two groups have demonstrated this stage with superconducting circuits [46, 47].

The final two stages—operations on single logical qubits and algorithms on multiple logical qubits—mirror the initial two stages of the progression, but for logical qubits in place of physical qubits. One caveat for these steps: they must be completed without degrading the lifetime of the logical qubits. The first demonstrations of operations on single logical qubits [48, 49] were made this year with superconducting circuits. As of yet, no experimental platforms have demonstrated the sixth stage.

Naturally, the different experimental platforms have their specific affordances and drawbacks. The purpose of Fig. 2.1 is not to compare progress among subfields, but rather to emphasize the commonalities among the different approaches, highlight the progress that the field as a whole has made, and motivate superconducting circuits as a *viable* platform for quantum information processing. Indeed its promise as a subfield has attracted interest outside the academic realm: a variety of private enterprises (IBM, Google, Rigetti Computing, DWAVE Systems, etc.) are now actively engaged in the construction of a superconducting quantum computer.

2.2 Quantum error correction and hardware architectures

As efforts in industry and academic settings look forward and plan their ascent to the upper echelon's of Fig. (2.1), their hardware requirements will depend strongly on the architectures they employ, especially in the context of error correction. A detailed review of these proposals is beyond the scope of this thesis, but a brief overview is helpful in estimating the hardware resources required for a fault-tolerant quantum computer.

It is now widely accepted that error correction will occupy a majority of the resources of a fault-tolerant quantum computer [38]. One approach to error-correction involves the use of stabilizer codes [50, 51, 52], in which a logical qubit is formed by redundantly encoding information in a register of entangled physical qubits. The Steane code, for example, can be implemented with

seven physical qubits in its register [51]. Under the assumption that error rates are sufficiently low such that at most one error occurs during each pass of the code, errors are detected by measuring collective properties of the register (the eponymous “stabilizer operations”). Additional gates can then be applied to correct the error, if needed.

The assumption that errors occur singly is, however, quite stringent. For the range of currently conceivable error rates, its satisfaction requires that the protocol be nested, such that each element in the error correcting register is itself a logical qubit, stabilized by its own register, which could itself be composed of logical qubits, and so on. As the stabilizer codes are also fairly operation intensive—that is, they drastically increase the number of gates required to implement an algorithm—stabilizer codes are recognized as a feasible but challenging way to perform error correction.

A more recent but related approach is known as the surface code, in which identical physical qubits are arranged in a rectangular array, which forms a surface [53, 26]. Connecting groups of four nearby qubits in a particular way allows rapid measurements of their parity to detect errors. The advantages of this approach are its flat hierarchy, which can be easily scaled once demonstrations of a unit cell are made, and its relatively relaxed requirements for single-qubit error rates (with respect to the stabilizer codes, for example). The drawbacks, however, are that a very large number of qubits (current estimates are on the order of 10^8 or 10^9 physical qubits for a modest quantum computation [26]) are required to reach a fault-tolerant level with the protocol, and that these benefits do not become substantial in systems with less than hundreds or thousands of physical qubits [38]. Nonetheless, efforts to demonstrate proofs-of-principle are already underway at Google [46] and IBM [54]. Ref. [55] gives a good overview and summary of the technical challenges relevant to this architecture.

A third strategy, which may be called the modular approach, is based on networks of nested modules, which rely heavily on hierarchy. In this scheme, information is stored in memory qubits which interact with the greater network via intermediate communication qubits. Computation is performed via manipulations of the communication qubits, which distributes entanglement across

the network. In some sense, this strategy represents the antithesis of the surface code approach: its affordances are the capability to test and iterate individual modules and processes, and possibly a lower requirement of physical qubits, at the cost of increased architectural and process complexity.

Ultimately, as with the choice of experimental platforms, selection of the optimal architecture for fault-tolerant quantum computing is an open question. But while the precise structure is yet to be determined, it seems clear that the necessary hardware resources will be immense.

2.3 Circuit quantum electrodynamics

To provide a more concrete notion of these hardware needs, we specialize now to a discussion of quantum information processing with superconducting circuits. Detailed reviews on this subject may be found elsewhere [56, 57]. Here we provide only an informal introduction, intended to give context for the design of a scalable circulator for superconducting quantum circuits.

The qubits in this platform are usually formed by slightly anharmonic electromagnetic oscillators. At sufficiently low temperatures, $k_B T < \hbar\omega$, the quantized energy levels in these circuits are resolvable. Here, k_B is Boltzmann's constant, T is the temperature of the environment, \hbar is Planck's constant over 2π , and ω is a frequency scale for the anharmonic oscillator. Modern dilution refrigerators allow for experiments at temperatures in the tens of mK, which makes the energy available from the thermal bath about ten times less than a photon at 5 GHz. Hence, the oscillators are designed to have resonant frequencies in the microwave range, typically between 1 and 20 GHz.

Like atoms, superconducting qubits come in a variety of forms. Most, though, can be modelled as a network of capacitors, inductors, and Josephson junctions. The Josephson junction [58] provides a dissipationless nonlinearity to the circuit, which breaks the harmonic spacing of its energy levels and allows individual transitions to be addressed with coherent microwave tones. A qubit can then be created by restricting attention to a pair of energy eigenstates (typically, the two lowest energy levels).

Readout of such a qubit, in the circuit quantum electrodynamics (cQED) scheme [59], is

accomplished by dispersively coupling the qubit to a microwave cavity.² In the dispersive limit, the cavity’s resonant frequency is dressed by the state of the qubit, and a transmission measurement of the cavity can therefore indicate the state of the qubit in a QND manner [60, 61].

For a transmon³ in the dispersive limit, the effective Hamiltonian that governs the qubit-cavity system is given by [62]

$$\begin{aligned} H &= \hbar\omega_q\sigma_z + \hbar(\omega_r + \chi\sigma_z)\hat{a}^\dagger\hat{a}, \\ &= \hbar\left(\omega_q + \chi\hat{a}^\dagger\hat{a}\right)\sigma_z + \hbar\omega_r\hat{a}^\dagger\hat{a}. \end{aligned} \tag{2.1}$$

Here ω_q is the qubit frequency (the difference between the ground and first excited states of the transmon), ω_r is the resonator’s frequency, \hat{a} is the annihilation operator for the cavity, σ_z is the Pauli z operator for the qubit, and χ is the dispersive shift—a parameter that characterizes the coupling between the qubit and the cavity. In the first line of Eq. (2.1), the Hamiltonian is factored to make explicit the qubit-state-dependent dressing of the cavity’s resonant frequency.

The same effect, however, also dresses the qubit frequency by an amount proportional to the photonic occupation in the cavity, as shown in the second line of Eq. (2.1). This allows the qubit to act as a photon counter/detector [22], and reveals the importance of controlling the photonic occupation in the cavity: a “hot” cavity, occupied by a high-temperature thermal state, will contain a broad distribution of Fock states, effectively broadening the qubit transition. This effect is so pronounced that superconducting qubits have become the most sensitive thermometers in these experiments. Measurable reductions in qubit coherence are observed with average cavity-photon occupations of 10^{-3} [63].⁴

In this light, one can see that the need to enforce the directional propagation of signals in cQED measurements arises directly from the Hamiltonian in Eq. (2.1). To probe the state of the qubit, electromagnetic waves departing the resonant cavity must be directed to a microwave

² Typically a distributed resonator formed, for example, by a quarter-wave transmission line, or a literal (three-dimensional) metal cavity.

³ One example, chosen from a selection of different superconducting qubits (see, for example, Sec. 2 in Ref. [57]).

⁴ As an aside, it may be noted that in some implementations this scheme is inverted, and a microwave resonator serves as the memory element, while a qubit such as the transmon provides a dispersive nonlinearity that allows individual transitions in the resonator to be addressed [64]. This is advantageous as coherence times in microwave cavities currently exceed those in superconducting qubits [65].

receiver. At the same time, however, electromagnetic waves propagating toward the cavity should originate from a cold bath—in practice, a 50 Ohm resistor to ground, well-thermalized at the base of a dilution refrigerator—to avoid dephasing the qubit.

Experimentally, this uni-directional signal flow is enforced by non-reciprocal circuit elements known as circulators and isolators. Isolators are impedance-matched two port devices which transmit a signal incident on one of their ports, but absorb signals incident on their other port. Circulators are impedance-matched n -port devices with three or more ports ($n \geq 3$), which transmit signals incident on port $m \leq n$ to port $1 + (m \text{ modulo } n)$: they “circulate” an incident signal, directing it out of one of the two adjacent ports.

Fig. 2.2 depicts this process for an $n = 3$ port circulator. In Fig. 2.2a, a signal incident on the circulator’s first port is transmitted to its second port. In Fig. 2.2b, a signal incident on port 2 is routed to port 3. Fig. 2.2c shows a signal incident on port 3 directed to port 1. A circulator may be configured as an isolator by terminating all but two adjacent ports in 50 Ohms.

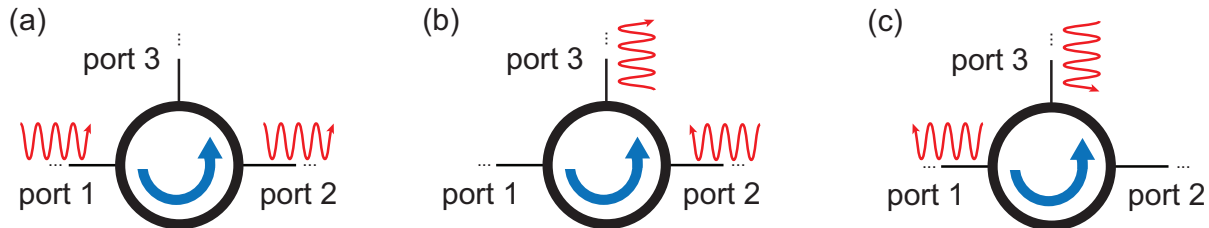


Figure 2.2: Schematic displaying the way in which an $n = 3$ port counter-clockwise circulator (circle with blue counter-clockwise arrow) routes incident fields. (a) A field incident on the circulator’s first port is transmitted out the second port. (b) A field incident on the second port is routed out the third port. (c) A field incident on the third port is routed out the first port.

To illustrate how circulators and isolators are utilized in the cQED architecture, Fig. 2.3 shows a simplified experimental schematic for readout of a superconducting qubit coupled to a resonant cavity. To reduce the thermal population of states in the qubit-cavity system, the devices are mounted at the base of a dilution refrigerator. In the readout procedure, a signal generator at room temperature first creates a microwave tone which propagates to the base of the refrigerator

and impinges on the weakly-coupled port of the resonant cavity (depicted as a Fabry-Perot cavity in Fig. 2.3). The tone then traverses the cavity, and a portion of its power exits out the second, strongly-coupled cavity port. Here the tone is transmitted through an isolator and directed by a circulator to a “quantum” reflection amplifier, where the signal is reflected with gain of approximately 20 dB. Here, “quantum” is used to mean an amplifier with added noise approximately equal to half a photon [66]—for example, a Josephson parametric amplifier [24] or a Josephson parametric converter [25]. Next, the circulator routes the tone through a second isolator, is amplified a second time by a high-electron mobility transistor (HEMT) amplifier, and finally propagates up the fridge for further room-temperature amplification and digitization. In various schemes, the phase or amplitude of the transmitted tone can be made to encode the state of the qubit, via the interaction described in Eq. (2.1).

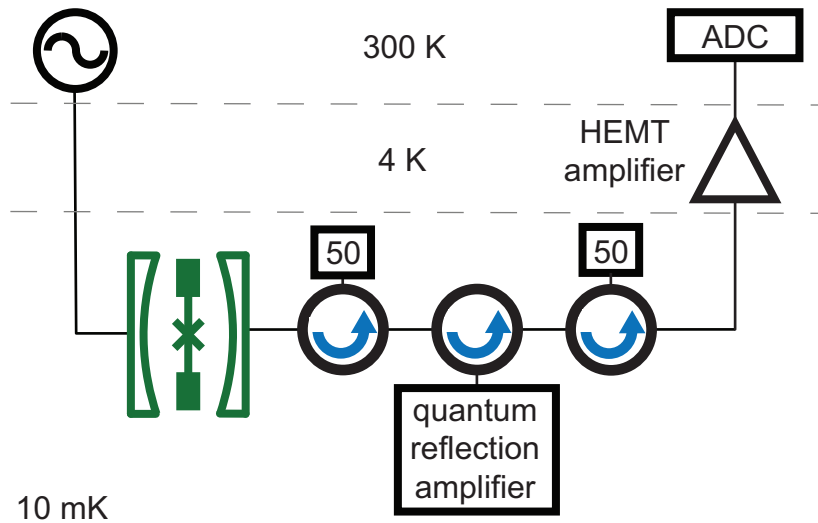


Figure 2.3: Simplified experimental schematic illustrating readout of a superconducting qubit in a dilution refrigerator. Signal filtering and attenuation, and control lines of the reflection amplifier, are omitted for clarity. The superconducting qubit (green cross with capacitive paddles) is situated inside a microwave resonant cavity (illustrated graphically by the green Fabry-Perot resonator) with two ports. A measurement of the transmission through the cavity can encode the state of the qubit. Circulators and isolators are used to direct the signal that exits the cavity out to a detector, while ensuring that the reverse-propagating signals originate from a cold-bath (and are not, for example, carrying the Johnson noise of the HEMT amplifier, or the strong pump tones in the reflection amplifier).

In this measurement, the signal routing capabilities of circulators are used in several ways, as evidenced by the multiple circulators employed in the readout of a single qubit. The first circulator, configured as an isolator, directs reflected signals and the strong pump tones powering a quantum reflection amplifier into a cold bath (serving as an entropy dump), while supplying the strongly coupled port of the qubit/cavity system with Johnson noise from this cold bath. The second circulator separates the incoming and outgoing signals for a quantum reflection amplifier, transforming that one-port device into a usable amplifier. A third circulator, again configured as an isolator, directs the Johnson noise emitted by the HEMT amplifier into an entropy dump, and replaces it with the Johnson noise from a cold bath.

It should be emphasized that the schematic in Fig. 2.3 illustrates the need for three circulators in a relatively simple single-qubit experiment. Experiments with multiple qubits, or additional requirements for directional signal routing, will employ more circulators. For example, a recent demonstration of the generation of remote entanglement between two superconducting qubit/cavities, using a third qubit/cavity as a detector, employed seven circulators [22]. Even with multiplexed readout and broadband (several GHz) circulators, a surface code quantum computer with modest capabilities [26] could still easily require millions of circulators.

Chapter 3

Lorentz reciprocity

First observed in optical systems, where it is referred to as Helmholtz reciprocity, Stokes-Helmholtz reciprocity, or the principle of reversibility, Lorentz reciprocity can be summarized colloquially as “if I can see you, you can see me” [67, 68]. In a more general sense, Lorentz reciprocity is the electromagnetic version of a symmetry common to a variety of physical systems, which implies that the response at point a due to an impulse at b is identical to the response at b due to an impulse at a . The prevalence of reciprocity theorems stems from the invariance of many systems under time-reversal [69].

As in the electromagnetic case, breaking reciprocity can be of fundamental scientific interest and great technological use. Efforts to generate non-reciprocity are therefore also underway in, for example, acoustical and mechanical systems [70, 71]. Connections between non-reciprocity and the one-way propagation of edge-states in topological systems have also been observed, and are driving research in topological acoustics [72, 73], metamaterials [74], and non-reciprocal devices based on the quantum Hall effect [75, 76, 77].

In the electromagnetic context, Lorentz reciprocity is essentially a statement about the time-reversibility of Maxwell’s equations [19], which occurs under certain assumptions: in a framework where electromagnetic fields propagate in guided modes into and out of a bounded network at ports, Lorentz reciprocity implies that the scattering between a pair of ports is invariant upon exchange of the source port and the detection port [78, 79]. This statement can be proven and expressed succinctly in a scattering matrix formalism, which we now introduce, following Ref. [80].

3.1 The scattering matrix

Consider a bounded region of space, enclosed by the surface Ω_s , which contains a linear electrical network with time-independent components (Fig. 3.1). Energy can be exchanged between the network and the environment (the region outside Ω_s) only through lossless and reciprocal waveguides, which we refer to as ports. (We assume the surface is sufficiently large such that radiative modes may be neglected, and shaped such that each waveguide is normal to Ω_s).

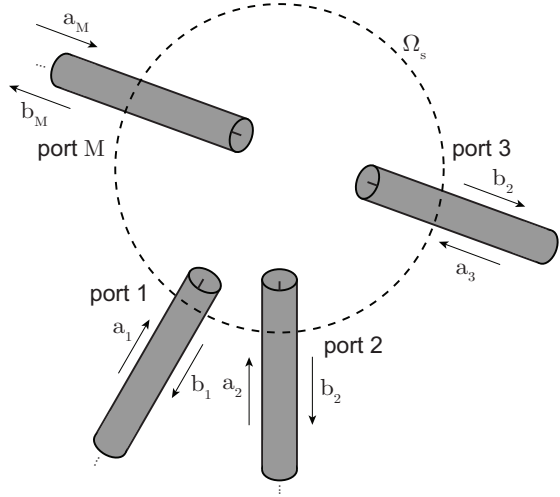


Figure 3.1: Model of an electrical network as a region of space bounded by the surface Ω_s . Electromagnetic signals can propagate into and out of the network in guided modes, referred to as ports. After [80].

For each waveguide, we imagine a coordinate system with the z -axis oriented along the waveguide, and directed into Ω_s . These waveguides carry guided modes which are eigensolutions of Maxwell's equations, propagating in the $+\hat{z}$ and $-\hat{z}$ directions. The components of the electromagnetic fields tangential to Ω_s have the form

$$\begin{aligned}\mathbf{E}_{T,\mu}(x, y, z) &= \left(a_\mu e^{-i\beta_\mu z} + b_\mu e^{i\beta_\mu z} \right) \mathbf{e}_{T,\mu}(x, y), \\ \mathbf{H}_{T,\mu}(x, y, z) &= \left(a_\mu e^{-i\beta_\mu z} - b_\mu e^{i\beta_\mu z} \right) \mathbf{h}_{T,\mu}(x, y).\end{aligned}\tag{3.1}$$

Here μ is the mode index, a_μ and b_μ are the complex amplitudes of the waves travelling into and out of the network, and β_μ is the propagation constant. The modes are normalized such that

$$\int_{\Omega_s} (\mathbf{e}_\mu \times \mathbf{h}_\nu^*) d\mathbf{A} = 2\delta_{\mu\nu}, \quad (3.2)$$

where * indicates complex conjugation and $\delta_{\mu\nu}$ is the Kronecker delta.

Eq. (3.2) has two interesting consequences. First, at the surface Ω_s the tangential components of the fields have the simple form

$$\begin{aligned} \mathbf{E}_T &= \sum_{\mu} (a_{\mu} + b_{\mu}) \mathbf{e}_{T,\mu}, \\ \mathbf{H}_T &= \sum_{\mu} (a_{\mu} - b_{\mu}) \mathbf{h}_{T,\mu}, \end{aligned} \quad (3.3)$$

which is useful in deriving one of the principal consequences of the Lorentz reciprocity theorem for networks.

Second, the power P carried into the network is just the difference of the wave power entering the surface and the wave power exiting the surface:

$$\begin{aligned} P &= \sum_{\mu} (|a_{\mu}|^2 - |b_{\mu}|^2) \\ &= \mathbf{a}^{*t} \mathbf{a} - \mathbf{b}^{*t} \mathbf{b}. \end{aligned} \quad (3.4)$$

Here in the second line we've introduced a vector notation \mathbf{a} and \mathbf{b} for the complex amplitudes a_{μ} and b_{μ} , and superscript t indicates vector transposition.

Our assumption that Ω_s encloses a passive and linear network ensures that the vector \mathbf{b} is completely determined by \mathbf{a} . If this were not the case, the network could scatter an excitation \mathbf{a} into distinct outputs \mathbf{b} and \mathbf{b}' . The linearity of the network implies that a null excitation ($\mathbf{0} = \mathbf{a} - \mathbf{a}$) could therefore scatter into $\mathbf{b} - \mathbf{b}'$. Eq. (3.4) shows that the power carried out of the network in this event is non-zero, in violation of the assumption that Ω_s encloses a passive network.

As the network is assumed to be linear, there is thus a unique matrix \mathbf{S} which maps \mathbf{a} to \mathbf{b} :

$$\mathbf{S}\mathbf{a} = \mathbf{b}. \quad (3.5)$$

The matrix element $S_{\mu\nu}$ is the ratio of the outgoing field at port μ to the incident field at port ν . The matrix \mathbf{S} is known as the scattering matrix, for its description of how the network bounded by Ω_s scatters incident fields.

3.2 The Lorentz reciprocity theorem

Consider two scattering processes, with excitation states \mathbf{a}' , \mathbf{a}'' , output states \mathbf{b}' , \mathbf{b}'' , and their corresponding fields \mathbf{E}' , \mathbf{E}'' and \mathbf{H}' , \mathbf{H}'' . With no electromagnetic sources, the time-harmonic form of Maxwell's equations for the fields of the first scattering process is

$$\nabla \times \mathbf{E}' = -i\omega\boldsymbol{\mu}(\mathbf{H}')\mathbf{H}', \quad (3.6)$$

$$\nabla \times \mathbf{H}' = i\omega\boldsymbol{\epsilon}(\mathbf{E}')\mathbf{E}'. \quad (3.7)$$

Here $\boldsymbol{\mu}(\mathbf{H})$ and $\boldsymbol{\epsilon}(\mathbf{E})$ are the magnetic permeability and electrical permittivity tensors of the media in Ω_s . Taking the inner product $[\cdot]$ of Eq. (3.6) with \mathbf{H}'' and Eq. (3.7) with \mathbf{E}'' and summing them yields

$$\mathbf{H}'' \cdot (\nabla \times \mathbf{E}') + \mathbf{E}'' \cdot (\nabla \times \mathbf{H}') = i\omega [\mathbf{E}'' \cdot \boldsymbol{\epsilon}(\mathbf{E}')\mathbf{E}' - \mathbf{H}'' \cdot \boldsymbol{\mu}(\mathbf{H}')\mathbf{H}']. \quad (3.8)$$

Repeating this procedure with the second scattering process yields the same result, with interchanged primes. When the two equations are subtracted, one obtains

$$\nabla \cdot (\mathbf{E}' \times \mathbf{H}'' - \mathbf{E}'' \times \mathbf{H}') = i\omega [\mathbf{E}'' \cdot \boldsymbol{\epsilon}(\mathbf{E}')\mathbf{E}' - \mathbf{E}' \cdot \boldsymbol{\epsilon}(\mathbf{E}'')\mathbf{E}'' - \mathbf{H}'' \cdot \boldsymbol{\mu}(\mathbf{H}')\mathbf{H}' + \mathbf{H}' \cdot \boldsymbol{\mu}(\mathbf{H}'')\mathbf{H}'']. \quad (3.9)$$

A vector identity for the divergence of the cross-product of two vectors was used to simplify the left-hand side of this expression. It may be further simplified to have a vanishing right-hand side, if the two following conditions are met:

- (1) $\boldsymbol{\epsilon}$ and $\boldsymbol{\mu}$ are symmetric tensors: $\boldsymbol{\epsilon} = \boldsymbol{\epsilon}^t$ and $\boldsymbol{\mu} = \boldsymbol{\mu}^t$.
- (2) $\boldsymbol{\epsilon}$ and $\boldsymbol{\mu}$ describe linear media.

To see this, consider one of the terms on the right-hand side:

$$\begin{aligned}
\mathbf{E}'' \cdot \boldsymbol{\epsilon}(\mathbf{E}')\mathbf{E}' &= \mathbf{E}'' \cdot \boldsymbol{\epsilon}\mathbf{E}' \\
&= (\mathbf{E}'' \cdot \boldsymbol{\epsilon}\mathbf{E}')^t \\
&= (\mathbf{E}''^t \boldsymbol{\epsilon}\mathbf{E}')^t \\
&= (\mathbf{E}'^t \boldsymbol{\epsilon}^t \mathbf{E}'') \\
&= (\mathbf{E}' \cdot \boldsymbol{\epsilon}\mathbf{E}'') \\
&= \mathbf{E}' \cdot \boldsymbol{\epsilon}(\mathbf{E}'')\mathbf{E}''.
\end{aligned} \tag{3.10}$$

Here we've used the linearity of $\boldsymbol{\epsilon}$ in the first line and the fact that scalars are invariant under transposition in the second line. The second to last line follows from the symmetry of $\boldsymbol{\epsilon}$. A magnetic term can be similarly commuted, to obtain the Lorentz reciprocity theorem:

$$\nabla \cdot (\mathbf{E}' \times \mathbf{H}'' - \mathbf{E}'' \times \mathbf{H}') = 0. \tag{3.11}$$

Eq. (3.11) gains a clear physical interpretation when it is expressed in the scattering matrix formalism. Integrating it over the volume enclosed by Ω_s and applying the divergence theorem yields

$$\int_{\Omega_s} (\mathbf{E}' \times \mathbf{H}'' - \mathbf{E}'' \times \mathbf{H}') \cdot d\mathbf{A} = 0. \tag{3.12}$$

When the modal expansions in Eq. (3.4) are substituted into Eq. (3.12), the minus sign ensures that the cross-terms add constructively, while the other terms add destructively:

$$\begin{aligned}
0 &= 2 \sum_{\mu, \nu} (b'_\nu a''_\mu - a'_\mu b''_\nu) \int_{\Omega_s} \mathbf{e}_\mu \times \mathbf{h}_\nu d\mathbf{A}, \\
&= \mathbf{b}^t \mathbf{a}'' - \mathbf{a}^t \mathbf{b}'', \\
&= \mathbf{a}^t (\mathbf{S}^t - \mathbf{S}) \mathbf{a}''
\end{aligned} \tag{3.13}$$

Here we've used the orthogonality condition in Eq. (3.2) and the definition of the scattering matrix in Eq. (3.5). As \mathbf{a}' and \mathbf{a}'' are arbitrary, the scattering matrix must be symmetric:

$$\mathbf{S} = \mathbf{S}^t. \tag{3.14}$$

This symmetry ensures that the scattering between a pair of ports is invariant under exchange of the source port and the detection port: $S_{\mu\nu} = S_{\nu\mu}$.

3.3 Methods for breaking Lorentz reciprocity

Concepts for non-reciprocal devices may be broadly divided into categories, based upon which assumption of the Lorentz reciprocity theorem they violate.

3.3.1 Magneto-optic devices

Virtually all the circulators and isolators currently used in cQED experiments are constructed with magneto-optic materials. A common example of this is the Faraday-effect [81], in which left and right circularly polarized fields propagating in a gyrotropic material (which is biased by a magnetic field parallel to the propagation direction) have different group velocities. Careful choice of the propagation length and or magnetic field strength therefore allows the polarization of the field to be rotated by the desired angle.

Critically, the polarization's sense of rotation depends only on the orientation of the magnetic field, and not on the direction of propagation. Fig. 3.2a and Fig. 3.2b illustrate this process. The effect, from the perspective of an observer receiving the propagating field, is therefore a propagation-direction-dependent rotation of the polarization. The observer's perspective is relevant here as this represents the perspective of a detector receiving the propagating field, and Lorentz reciprocity is an invariance upon exchange of source and detector.

In optical applications, this phenomenon is combined with a pair of polarizers to create an isolator. In the microwave domain, it is commonly used to couple signals (non-reciprocally) between orthogonally-polarized waveguides, realizing a circulator. Ref. [83] provides a detailed description of ferrite-junction circulators that operate via the Faraday effect.

The Faraday effect may be contrasted with a similar (and reciprocal) phenomenon in optically active materials [81], in which the chirality of the crystal structure rotates the polarization of the propagating field. This causes the polarization vector's sense of rotation to reverse when the

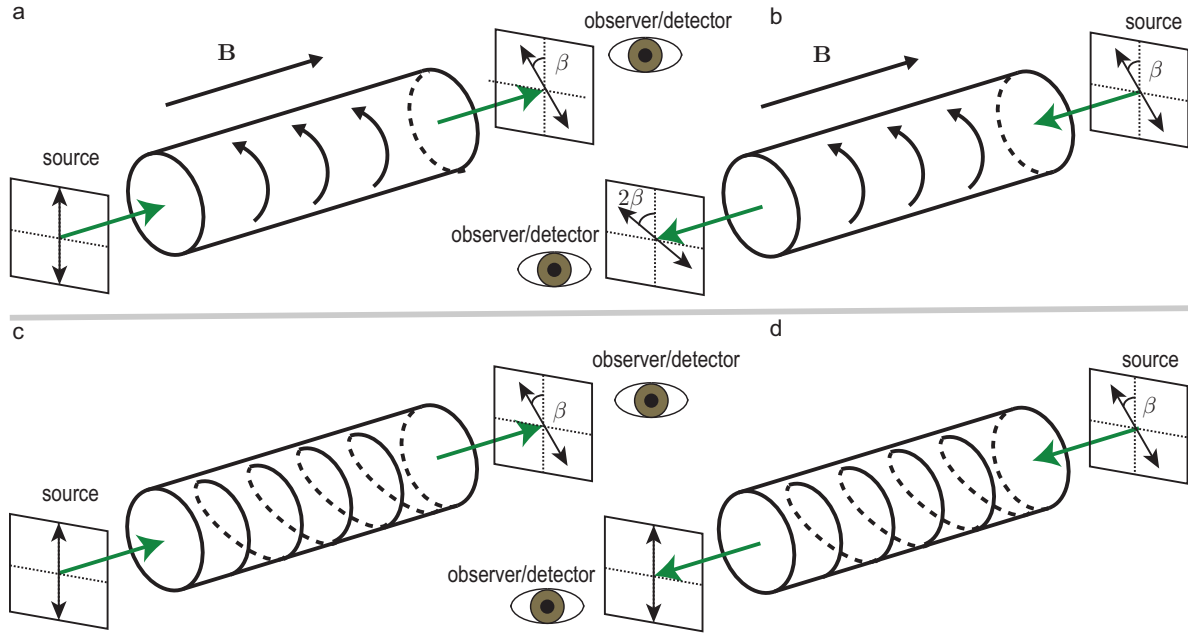


Figure 3.2: Faraday rotation and a seemingly similar but distinct phenomenon observed in optically active media. (a) An electromagnetic wave propagating from left to right through a Faraday-active medium in the presence of an applied on-axis magnetic field \mathbf{B} . From the perspective of an observer (or a detector) receiving the field, the polarization of the wave rotates clockwise by an angle β . (b) If the signal is reflected and propagates back through the medium (from right to left), the observer perceives a counter-clockwise rotation of the wave’s polarization by the same angle β . Transmission is non-reciprocal. (c) A wave propagating left to right through an optically active medium, where a material chirality (depicted as a helix) determines the sense of rotation. An observer receiving the wave perceives a clockwise rotation of the polarization. (d) Reflection of the wave and right to left propagation results in the same clockwise rotation of the polarization, and reciprocal transmission. After [82].

propagation direction is inverted, in the same way that pushing or pulling on a right-handed screw will induce clockwise or counter-clockwise rotation. From the perspective of an observer receiving the propagating field, however, the rotation-direction is independent of the propagation direction, as depicted in Fig. 3.2c and Fig. 3.2d.

Magneto-optic devices are unconstrained by reciprocity because the permeability tensor $\boldsymbol{\mu}$ is not symmetric in the presence of a static magnetic field. This leads to a non-vanishing right-hand side of Eq. (3.9), and a breakdown of the reciprocity theorem.

With respect to the design needs of superconducting qubit applications, magneto-optic non-

reciprocal devices are attractive in that they may have broad operation bandwidths, low (but not vanishing) insertion loss on the order of several tenths of a dB, and they are passive devices. Their drawbacks include their roughly 10 cubic cm volumes, and their reliance on large permanent magnets, which makes them difficult to miniaturize (despite many efforts [84, 85, 86, 87, 88, 89]) and integrate with superconducting circuits, and precludes the elimination of their insertion loss by replacing their metallic components with superconductors.

3.3.2 Nonlinear devices

Nonlinear devices can break reciprocity because the intensity-dependence of their material properties prevents the cancellation of terms like

$$\mathbf{E}'' \cdot \epsilon(\mathbf{E}')\mathbf{E}' - \mathbf{E}' \cdot \epsilon(\mathbf{E}'')\mathbf{E}''.$$
 (3.15)

As in the case of magneto-optic devices, this leads to a non-vanishing right-hand side of Eq. (3.9).

In practice, this is leveraged by introducing some kind of spatial asymmetry into the design of the device. A simple example of this is a finite-length rectangular waveguide which is filled by distinct dielectrics on its two ends [90]. The device is reciprocal, but careful choice of the dielectrics and the relative fractions of the waveguide that they fill makes the spatial profile of the electric field dependent on the propagation direction of an incident signal. By positioning a nonlinear resonator at a location within the waveguide where the intensity of the electric field is strong when a signal is incident on one port of the waveguide but weak when a signal is incident on its other port, a propagation-direction-dependent loss-channel can be introduced to the system—usually by arranging the frequency-pulling of the nonlinear resonator to move the resonator in or out of resonance with the incident signal. Different implementations of this general scheme have resulted in a variety of realizations for optical diodes constructed with silicon [91, 92, 93, 90].

The advantages of this approach include ease of miniaturization, and compatibility with superconducting circuits and fabrication methods. The disadvantages are an inherent restriction on linearity (such schemes only work when higher-power incident fields or pump tones activate a

material nonlinearity), and typically narrow operation bandwidths.

3.3.3 Active devices

Given the intimate connection between reciprocity and time-reversal, it seems intuitive that active devices—that is, devices with parameters that vary in time—could break reciprocity. This can be seen explicitly with a simple example of two general cascaded linear systems A and B , which we describe following Ref. [94], and depict in Fig. 3.3. The impulse responses of A and B are denoted h_A and h_B , and u , z , and y describe the input, intermediate, and output states of the system.

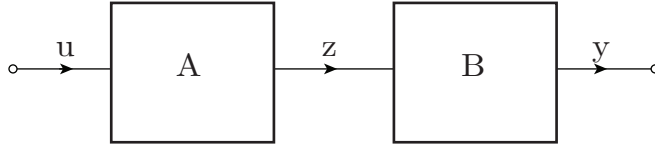


Figure 3.3: A cascade of two linear systems. The impulse response of the composite system is non-reciprocal when the impulse responses of the individual systems are time-dependent. After [94].

The output y can be written in terms of the input u and the impulse responses h_A and h_B :

$$y(t) = \int_{-\infty}^{\infty} h_B(t, \eta) z(\eta) d\eta \quad (3.16)$$

$$z(t) = \int_{-\infty}^{\infty} h_A(t, \xi) u(\xi) d\xi. \quad (3.17)$$

Eliminating z in Eq. (3.16) yields

$$y(t) = \int_{-\infty}^{\infty} \left[\int_{-\infty}^{\infty} h_B(t, \eta) h_A(\eta, \xi) d\eta \right] u(\xi) d\xi, \quad (3.18)$$

and the bracketed term in that expression may be identified as the impulse response h_{BA} of the composite system BA .

When A and B are time-invariant systems, their impulse responses depend only on the difference of their arguments,

$$h_{BA} = \int_{-\infty}^{\infty} h_B(t - \eta) h_A(\eta - \xi) d\eta. \quad (3.19)$$

Changing integration variables to $t' = t - \xi$ and $\eta' = \eta - \xi$, Eq. (3.19) becomes

$$h_{BA} = \int_{-\infty}^{\infty} h_B(t' - \eta') h_A(\eta') d\eta'. \quad (3.20)$$

which is a convolution. In this form (or from the convolution theorem), it is clear that the system is reciprocal: $h_{BA} = h_{AB}$. For the time-dependent case, though, h_{BA} is not in general equal to h_{AB} .

The dependence of reciprocity on time-invariance is reflected in the arguments of Sec. 3.1 and Sec. 3.2, which respectively assume passive networks and harmonic fields. Efforts in the 1960s extended these arguments to time-dependent systems, and showed that reciprocity also places symmetry and time-invariance constraints on the scattering matrices of time-variable networks [95]. Since then, a variety of schemes have been developed for generating non-reciprocity with actively modulated circuits. We do not attempt a complete catalogue of them here, and instead limit discussion to two particular approaches.

3.3.3.1 Parametric coupling of resonant modes in the resolved sideband limit

The first of these involves the parametric coupling of resonant modes in the resolved sideband limit, which is a widely used strategy in radio frequency [96, 97], superconducting microwave [82, 98, 99, 100, 101], electroacoustic [102], electromechanical [103, 104, 105], and optomechanical [106, 107] devices. Excepting the circulator discussed in this thesis, most state-of-the-art non-reciprocal circuits for superconducting circuits are implemented with this approach.

An excellent conceptual description of this strategy is given in Ref. [108], which provides a graph-theoretical description for the Langevin equations of parametrically coupled resonant systems. Rather than reproduce that treatment here, we attempt a succinct and general summary of the concept.

Consider a system of two or more resonant modes (frequencies $\{\omega_i\}$ and linewidths $\{\kappa_i\}$) in the resolved sideband limit. By this, we mean the frequencies in the set $\{\omega_i\}$ are separated by many times their respective linewidths, and that the linewidths of each resonator are narrower than all

the resonant frequencies. Now imagine a parametric interaction, which allows variation of a system parameter to shift the frequencies of the resonant modes $\{\omega_i\}$ by approximately their linewidths $\Delta\omega_i \approx \kappa_i$. Varying this parameter at the difference frequency $\omega_i - \omega_j$ between a pair of modes induces a beam-splitter interaction, allowing excitations to be exchanged between the two resonant systems:

$$H_I \propto e^{i\theta} a_i a_j^\dagger + e^{-i\theta} a_i^\dagger a_j. \quad (3.21)$$

Here, a_i is the annihilation operator of the i^{th} resonant mode, and θ is the phase of the parametric interaction. In practice, this phase can be adjusted by tuning the phase of the electrical signal which is controlling the parametric interaction.

Examination of Eq. (3.21) shows that the phase of the beamsplitter interaction depends on the direction in which excitations are exchanged. For example, if the phase $\theta = \pi/2$, excitations which originate in mode i and are transferred to mode j will be π out of phase with excitations which originate in mode j and are transferred to mode i . If desired, a frequency diplexer can then be used to route the different resonant modes out separate physical ports of the device.

There is a complication, though, in generating non-reciprocity in this way: the phase reference of the parametric interaction is arbitrary. Said another way, a gauge may always be chosen in which the phase θ is zero, making the beamsplitter interaction reciprocal. This difficulty may be resolved with the introduction of another parametric interaction between modes i and j (or to a third mode k). Experimentally, this can be accomplished by cascading a duplicate of the original device in series with the original [101]. The second parametric interaction also has a phase, and while its phase reference is also arbitrary, the difference between the phases of the two parametric interactions is a gauge-invariant.

A description of this approach can also be couched in the language of geometric phases created by synthetic magnetic fields [109, 110, 111, 102, 99, 107]. In that framework, the coupled resonant modes are viewed as nodes of a lattice, with a hopping interaction determined by the system's parametric modulation. The phase of the parametric modulation sets a Peierls's phase [112], and

a Berry curvature (synthetic vector potential) is quantified by the total Peierls’s phase acquired in the circumnavigation of one plaquette of the lattice.

The affordances of using parametrically coupled modes to generate non-reciprocity are the relative simplicity of the circuit designs, and a wide versatility in function: in addition to realizing elementary non-reciprocal devices such as isolators [103] and circulators [99, 100], the parametric interaction can also be used to drive parametric down-conversion, enabling processes like directional amplification [98, 99, 100, 113]. This flexibility, and the ability to dynamically switch between the various modes of operation, has led some groups to refer to these devices as “field-programmable,” in reference to multi-function field-programmable gate arrays [100]. The major drawback inherent to this method is its reliance on resonant modes in the resolved sideband limit, which constrain the device’s bandwidth. A second drawback, in some situations, is the frequency-conversion which accompanies some implementations of this approach [99, 100].

3.3.3.2 Frequency conversion and delay

A second approach for the generation of non-reciprocity with active devices is enabled via successive translations in frequency and time, or in other words, a combination of frequency conversion and delay. As frequency and time are Fourier duals, successive translations in these quantities do not, in general, commute. Signals traversing a network in which a series of these translations are made may encounter them in a different time-ordering, depending on the port of the network at which they arrive. Such a dependence on propagation direction violates Lorentz reciprocity.

The promise of generating non-reciprocity in this way was first observed in the 1960s, in cascades of symmetric lattices with dual arms of time-varying inductors and capacitors [114]. In these networks, a tank circuit resonance provides the delay, and the active modulation of the circuit elements create frequency sidebands on the input signal. In more recent years, the idea has been leveraged in a general-purpose circulator proposal which is amenable for implementation in superconducting circuits [115]. The realization of that proposal is the subject of this thesis. Related proposals in the microwave [116], millimeter [?], and optical [117, 118, 119, 120] domains

have utilized the same concept with non-resonant delays.

The affordances of the frequency-conversion and delay approach are a general absence of bandwidth constraints, stemming from the potential to implement the approach without any resonant physics. Related to this, resonant-based implementations are in general not subject to the constraints of the resolved sideband-limit, allowing low-frequency modulation of the active components. This is an especially attractive feature for superconducting circuits, where high-bandwidth dilution-refrigerator lines are a precious resource.

Its drawbacks are the care required in coherently erasing (or otherwise suppressing) sidebands created by the frequency converting elements, and the general circuit complexity which is sometimes needed for this task. An additional drawback, which is also common to circuits based on the parametric coupling of resonant modes, or in general any active device, is the power consumption of the control signals. This is not a problem for some applications, but in a cryogenic setting additional heat loads on the mixing chamber of a dilution refrigerator are an important consideration, especially in light of the large number of circulators which may be required in a superconducting fault-tolerant quantum computer.

3.3.4 Connection with time-reversal symmetry

As reciprocity arises in physical systems which are invariant under time-reversal, another way to classify non-reciprocal systems is via the mechanism by which they break this invariance. This perspective is utilized in recent demonstrations [107] and proposals [121, 122, 123], which break Lorentz reciprocity with judicious use of dissipation, referred to as reservoir engineering.

Generating non-reciprocity, however, does not in general require dissipation, or a complete absence of time-reversal symmetry. For example, many approaches break Lorentz reciprocity by coupling electromagnetic fields to matter with an interaction that is odd under time-reversal. Examples of this are magnetic fields, as in circulators built with gyrotropic media and quantum Hall effect circulators [75, 76, 77]; linear momentum [124, 125, 126, 127], for example through dispersion engineering [125, 126, 127] or radiation pressure in an optomechanical interaction [124]; and

angular momentum [96, 70, 115], for example, by coupling electromagnetic fields to non-degenerate clockwise and counter-clockwise propagating modes in a ring resonator. The degeneracy of these modes can then be lifted with physical rotation, as in a Sagnac interferometer [128] (or in acoustic demonstrations, with the motion of the acoustic medium [70]). It may also be lifted in other ways, such as active modulation of circuit parameters, which can simulate a sense of rotation [115] or a synthetic gauge field [96].

3.4 Common non-reciprocal devices

As both Lorentz reciprocity and scattering matrices have now been discussed, we introduce in this section the scattering matrix description of several common non-reciprocal devices. Tab. 3.1 shows the microwave circuit symbols and scattering matrices for a gyrator, an isolator, and a circulator.

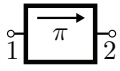
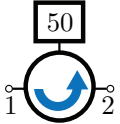
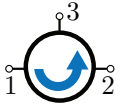
	gyrator	isolator	circulator
microwave circuit symbol			
ideal scattering matrix	$\begin{bmatrix} 0 & 1 \\ -1 & 0 \end{bmatrix}$	$\begin{bmatrix} 0 & 0 \\ 1 & 0 \end{bmatrix}$	$\begin{bmatrix} 0 & 0 & 1 \\ 1 & 0 & 0 \\ 0 & 1 & 0 \end{bmatrix}$

Table 3.1: Symbols and scattering matrices for three common non-reciprocal devices

3.4.1 Gyrotors

Gyrators are impedance-matched two-port devices that transmit signals in the forward direction without changing their phase, but impart a π phase shift to signals transmitted in the reverse direction [78]. This action is visible in their scattering matrix: for a gyrator, S_{21} and S_{12} are π out of phase. Gyrotors were first proposed in 1948 by Tellegen as a hypothetical fifth element of basic circuit theory, supplementing the resistor, inductor, capacitor, and transformer [129]. Addition of

the gyrator to this set allows for the realization of passive non-reciprocal networks, and also reduces the number of basic circuit elements to three: the gyrator can replace the transformer and either the capacitor or the inductor.

In practice, gyrators are used frequently in the design of active filters, and in the construction of other non-reciprocal circuits, such as isolators and circulators. This can be done directly, by tying together the grounds of the gyrator's two ports and defining a third port as the differential voltage between them, resulting in a three-port circulator. Alternatively, the gyrator can be inserted between two beamsplitters (or microwave hybrids) to create a four-port circulator. This procedure is known as the Hogan construction of a circulator [130].

3.4.2 Isolators

Isolators are impedance-matched two-port devices that act as one-way valves for classical electromagnetic signals. Signals propagating in the forward direction through an isolator are transmitted unchanged, while signals propagating in the reverse direction are completely absorbed. This action is visible in the off-diagonal elements of the scattering matrix: $S_{21} = 1$, while $S_{12} = 0$.

Isolators are used in a variety of ways across the electromagnetic spectrum: in optical experiments, they are commonly employed as a way to prevent reflections in an optical network from disturbing the source laser. In telecommunication networks, where signals are frequently amplified and attenuated by many orders of magnitude, isolators serve as a way of protecting sensitive (and lower signal-amplitude) components in the network from amplifier reflections. More generally, as discussed in Ch. 1, isolators are of fundamental use in precision measurement.

3.4.3 Circulators

Circulators are impedance matched devices with three or more ports, that provide the directional signal routing needed for a variety of electromagnetic networks. As the scattering matrix in Tab. 3.1 shows, signals incident on one of the circulator's ports will be routed counter-clockwise around the device and transmitted out the subsequent port.

Circulators can be used to make isolators (by depositing the signal at all but two of the circulator ports into an entropy dump) or gyrators (by combining them with 180-degree microwave hybrids/beamsplitters). The need for a high-quality and scalable circulator which could supplant the ferrite-based commercial circulators currently used in superconducting qubit experiments is the motivation for this thesis.

Chapter 4

Theory of operation

The circulator presented in this thesis may be understood in terms of “synthetic rotation” created by the active modulation of the circuit, and analyzed rigorously with a lumped-element circuit theory or an input-output formalism [115]. Before performing a formal analysis we provide a complementary explanation for its operation based upon the frequency-domain dynamics of an analogous model system.

4.1 Model system

The model is a lumped-element network of multipliers and delays (Fig. 4.1a) which creates a gyrator (see Sec. 3.4.1). Gyration in the model system arises from the non-commutation of successive translations in frequency and time [116]: the multiplying circuits operate as frequency converters, translating an input signal up and down in frequency, and the delays translate fields forward in time. As frequency and time are Fourier duals, the time-ordering of these translations matters (the two operations do not generally commute). Transmission through the network thus depends on the propagation direction of the incident signal, breaking Lorentz reciprocity.

To see that non-reciprocity explicitly, frequency-phase diagrams are used to calculate the model’s scattering parameters. The diagrams follow an incident signal at frequency ω_p as it propagates through the device, tracking its amplitude, frequency, and phase in a frame rotating at ω_p .

The insets in Fig. 4.1a depict the way that the model system’s two constituent elements—

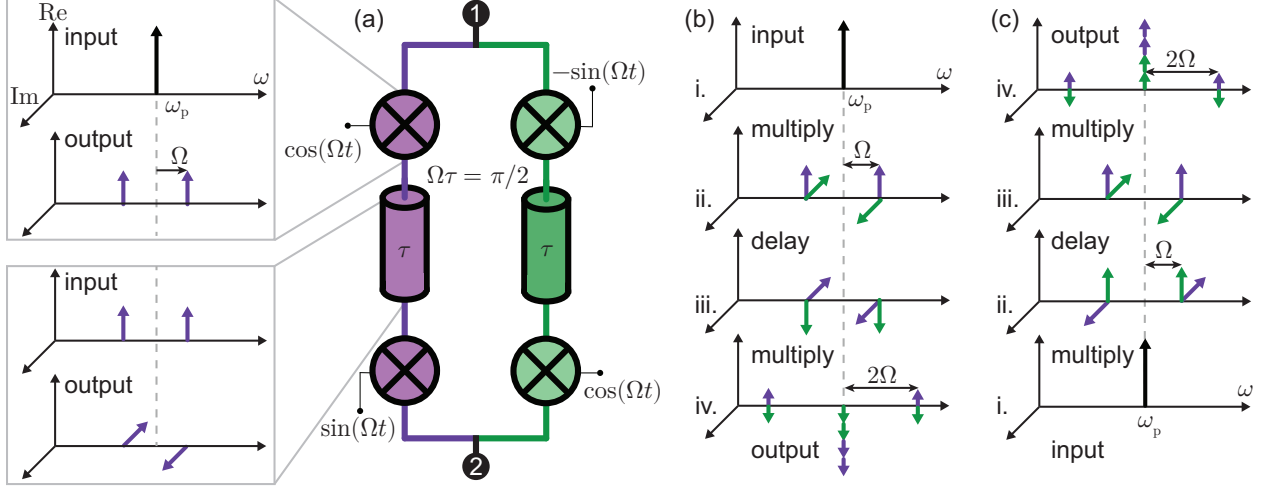


Figure 4.1: Conceptual diagram of non-reciprocity generated with frequency conversion and delay. (a) Lumped-element network that forms a gyrator. The insets show how fields are transformed by the network's two components: multiplying elements and delays. In the upper inset, an input field at frequency ω_p (top panel) is multiplied by $\cos(\Omega t)$ to create a field with spectral components at $\omega_p \pm \Omega$ (bottom panel). The real and imaginary axes of the plot shows the phase of these spectral components in a frame rotating at ω_p . In the lower inset, a delay of length $\tau = \pi / (2\Omega)$ advances (retards) the phase of spectral components at $\omega_p + \Omega$ ($\omega_p - \Omega$) by $\pi/2$. (b) Calculation of the forward-scattering parameter for the network in (a), by following an incident field at frequency ω_p as it propagates through the device. Purple (green) arrows indicate fields propagating in the left (right) arm of the network. Fields are forward transmitted with amplitude and frequency unchanged, but phase shifted by π . (c) Backward transmission through the network in (a). Fields are transmitted with amplitude, frequency, and phase unchanged.

multipliers and delays—transform input fields to output fields. In the multiplying elements, that transformation occurs via multiplication by a bias signal—in this case, $\cos(\Omega t)$. The trigonometric product-to-sum identity states

$$\cos(\omega_p t) \cos(\Omega t + \theta) = \frac{1}{2} \left(\cos([\omega_p + \Omega] t + \theta) + \cos([\omega_p - \Omega] t - \theta) \right), \quad (4.1)$$

which has a simple interpretation in the frequency domain: multiplication creates two sidebands, each detuned from ω_p by the bias frequency Ω . Importantly, the phases of these sidebands depend on the phase θ of the multiplier's bias signal. We choose a phase reference such that multiplication by $\cos(\Omega t)$ creates two sidebands with the same phase.

In the delay elements, inputs are transformed to outputs by way of a phase shift. In the

rotating frame, a delay of length $\tau = \pi/(2\Omega)$ leaves the phase of spectral components at ω_p unchanged, while advancing the phase of spectral components in the upper sideband $\omega_p + \Omega$ by $\pi/2$, and retarding the phase of components in the lower sideband $\omega_p - \Omega$ by $\pi/2$.

With the action of the multiplying and delay elements defined, calculation of the scattering parameters is straightforward. Forward transmission through the model system is shown in Fig. 4.1b. A signal incident on port 1 with frequency ω_p (Fig. 4.1b, i.) is first divided equally into the network's two arms. Fields in both arms encounter a first multiplying element, a delay, a second multiplying element, and are then recombined.

Critically, the modulation sidebands at $\omega_p \pm 2\Omega$ created in the network's two arms are π out of phase and interfere destructively at the device's output (Fig. 4.1b, iv). Conversely, the components at the frequency ω_p interfere constructively. Comparison of Fig. 4.1b, iv. with Fig. 4.1b, i. shows that the incident signal has been transmitted through the device with its frequency and amplitude unchanged, but its phase shifted by π . The scattering parameter S_{21} for the network is therefore -1 .

The reverse path is traced out in Fig. 4.1c, for a signal incident on the network's second port. As with forward transmission, destructive interference occurs at $\omega_p \pm 2\Omega$ (Fig. 4.1c, iv.). Likewise, this is accompanied by constructive interference at the frequency ω_p . Now, however, comparison of Fig. 4.1c, iv. with Fig. 4.1c, i. shows that the frequency, amplitude, and phase of the incident signal were unchanged by the network. Therefore, in contrast to the forward transmission, the backwards transmission is characterized by a scattering parameter $S_{12} = 1$. The network in Fig. 4.1a is thus described by the gyrator scattering matrix in Tab. 3.1, and forms an ideal gyrator.

In the model system, the convert-delay-convert process happens simultaneously in both arms of the network. Consequently, each arm is individually non-reciprocal. Alone, though, a single arm creates unwanted modulation sidebands. To create an ideal gyrator, two arms, with the bias signals of their multiplying elements separated in phase by $\pi/2$, are connected in parallel. This balanced architecture engineers destructive interference of the spectral components at $\omega_p \pm 2\Omega$.

Such a strategy for suppressing the creation of spurious sidebands, which we refer to as “co-

herent cancellation,” may be contrasted with that used in non-reciprocal devices that operate with the parametric coupling of resonant modes in the resolved-sideband limit, discussed in Sec. 3.3.3.1. In that scheme, parametric modulation of a resonant system creates sidebands at the parametric drive frequency, and a second resonant mode is used to enhance the density of states at the desired frequency, while simultaneously diminishing it at the undesired frequency. To work in the resolved sideband limit, however, the parametric modulation must be many times the resonant system’s linewidth. In microwave frequency implementations, this typically requires GHz modulation tones. In contrast, the coherent cancellation approach lifts the resolved-sideband constraint, and can therefore be used with lower-frequency control tones.

4.2 Superconducting implementation

We make use of the unique properties of superconducting circuitry to realize compact on-chip multiplier and delay elements. Specifically, Josephson junctions form widely tunable inductors, while vanishing conductor loss permits high-quality on-chip microwave resonators. Fig. 4.2 shows how a single arm of the model system (Fig. 4.2a) is made with a network of capacitors and dynamically tunable inductors (Fig. 4.2b).

4.2.1 Multiplying elements

The multiplying elements in the circuit representation are created with reactive bridge circuits (also known as symmetrical lattices [114]), built with two tunable pairs of nominally identical inductors l_+ and l_- arranged opposite one-another (gray box in Fig. 4.2b). Two differential ports are defined by the left-and-right and top-and-bottom bridge nodes. Importantly, the inductors tune in a coordinated fashion: when one pair of inductors increases, the other pair decreases. We parametrize this tuning with a base inductance l_0 and an imbalance variable δ , by writing

$$l_{\pm} = l_0 / (1 \pm \delta). \tag{4.2}$$

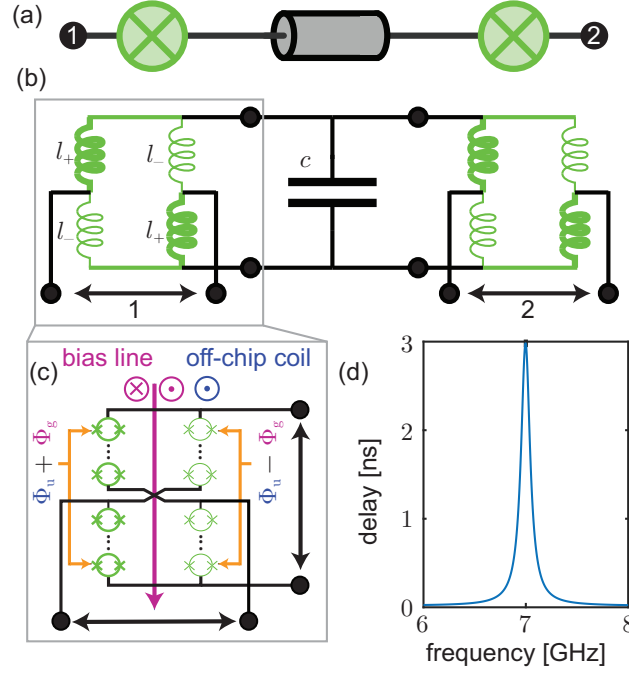


Figure 4.2: Multiplying elements and delays realized in a superconducting lumped-element circuit. (a) The model system (Fig. 4.1a) is constructed from two parallel instances of this network. (b) A lumped-element version of the network in (a), created with capacitors and tunable inductors arranged in a bridge geometry. (c) To create an inductive bridge circuit in a superconducting microwave environment, four series-arrays of SQUIDs are arranged in a figure-eight geometry, and tuned with an off-chip magnetic coil producing a uniform flux Φ_u and an on-chip bias line creating a gradiometric flux $\pm\Phi_g$. (d) Simulated group delay for the circuit in (b) when its ports are connected to 50 Ohm transmission lines. The bridge inductors are parametrized according to Eq. (4.2), with $c = 1$ pF, $l_0 = 1$ nH, and $\delta = 0.2$.

When a bridge is coupled to transmission lines of characteristic impedance Z_0 , its forward scattering parameter at angular frequency ω is

$$\begin{aligned}
 S_{21} &= \frac{2i\delta\omega l_0 Z_0}{-Z_0^2(1-\delta^2) - 2i\omega l_0 Z_0 + \omega^2 l_0^2} \\
 &= -\delta \frac{2i\omega l_0 Z_0}{(Z_0 + i\omega l_0)^2} + \mathcal{O}(\delta)^2.
 \end{aligned} \tag{4.3}$$

As the imbalance in the bridge determines its transmission, changing δ allows the circuit to act as a switch or a multiplying element [131, 132].

The bridge circuit's tunable inductors are realized with series-arrays of superconducting quan-

tum interference devices (SQUIDs), formed by the parallel arrangement of two Josephson junctions. Arrays are used in place of individual SQUIDs to increase the linearity of the inductors [115]. The inductance l of an N SQUID array depends on the magnetic flux Φ that threads through each SQUID [58]:

$$l = N \frac{\varphi_0}{2I_0} \left| \sec \left(\frac{\Phi}{2\varphi_0} \right) \right| + \mathcal{O}(I/I_0)^2. \quad (4.4)$$

Here $\varphi_0 = \hbar/2e$ is the reduced flux quantum, and the Josephson junctions in each SQUID are assumed to be identical with critical current I_0 and negligible geometric inductance. The SQUIDs are also assumed to be identical.

To realize the coordinated tuning of inductors described in Eq. (4.2), we arrange the SQUID arrays in a figure-eight geometry (Fig. 4.2c). Two flux controls determine the imbalance in the bridge. First, an off-chip coil threads a uniform magnetic flux Φ_u through all the SQUIDs. Second, an on-chip bias line, which bisects the figure-eight, threads a gradiometric flux Φ_g through the SQUIDs. SQUIDs on the left side of the bias line therefore experience an overall magnetic flux which is the sum of the uniform and gradiometric contributions, whereas SQUIDs to the right of the line are threaded by the difference of the uniform and gradiometric fluxes.

When the gradiometric bias line is driven with a sinusoidal current source at frequency Ω , the flux through the SQUIDs varies in time as $\Phi = \Phi_u \pm \Phi_g \cos(\Omega t + \phi)$. This process creates a bridge of inductors which tune according to Eq. (4.2), with a simple sinusoidal variation in the imbalance $\delta = \delta_0 \cos(\Omega t + \phi)$ and a rescaling of the base inductance l_0 . Such a periodic variation in δ makes SQUID bridges biased in this way into dissipationless multiplying elements. The precise mapping between the flux controls Φ_u & Φ_g and the circuit parameters l_0 & δ_0 is [133]

$$\begin{aligned} \delta_0 &= -2 \tan(\alpha) \frac{J_1(\beta)}{J_0(\beta)} + \mathcal{O}(\beta^2), \\ l_0 &= N \frac{\varphi_0}{2I_0} \frac{1}{\cos(\alpha) J_0(\beta)} + \mathcal{O}(\beta^2), \end{aligned} \quad (4.5)$$

with

$$\begin{aligned}\alpha &\equiv \pi \frac{\Phi_u}{\Phi_0}, \\ \beta &\equiv \pi \frac{\Phi_g}{\Phi_0},\end{aligned}\tag{4.6}$$

and J_n the n^{th} Bessel function of the first kind.

4.2.2 Delays

The second primitive needed for the model system is a delay, realized in our circuit with a resonant mode. Conveniently, the SQUIDs in the bridge circuits are inductive, so the addition of a single capacitor is enough to create a resonance. This resonance delays fields near its center frequency by a timescale τ characterized by the inverse of its linewidth. More quantitatively, when a harmonic field incident on port ν of a resonant network is scattered to port μ , it acquires a group delay $\tau = d\angle S_{\mu\nu}/d\omega$ [78]. Here ω is the frequency of the harmonic field, and $\angle S_{\mu\nu}$ is the phase of $S_{\mu\nu}$. Fig. 4.2d shows delay as a function of frequency, simulated for the resonant circuit in Fig. 4.2b. Fields near the circuit’s resonant frequency experience a delay of several nanoseconds. As a confirmation of these simulations, an analytical study of the same circuit was also made, using a graph theoretical approach [134, 135] to solve for the circuit’s eigenfrequencies with Kirchoff’s current and voltage laws. This is described in App. A.

Delays realized with resonant modes allow for a deeply sub-wavelength implementation, which is critical for the “coherent cancellation” approach. While these lumped-element delays are necessarily narrower in bandwidth than those created with, for example, a length of transmission line, their finite bandwidth is mitigated by the tunable inductance of the bridge circuits, which allows the frequency ω_0 of the resonant delay to be tuned (over several GHz) with the uniform magnetic flux Φ_u . As the multiplying elements are broadband [132], this tunability of the delay is inherited by the full circulator. Likewise, the duration τ of the delay depends on the imbalance in the bridges, and may be tuned with the gradiometric flux Φ_g , facilitating satisfaction of the requirement that $\tau = \pi/(2\Omega)$.

Tuning of the resonant delay takes a simple form when expressed in terms of the circuit parameters l_0 and δ_0 . When two of the arms in Fig. 4.2b are combined in parallel to create the fully assembled circuit, the resonant delay occurs at the frequency [115]

$$\omega_0 = \sqrt{\frac{4 - \delta_0^2}{2l_0c}}, \quad (4.7)$$

and its duration τ is approximately the inverse of the resonant mode's linewidth,

$$\tau \approx \frac{8Z_0c}{\delta_0^2}. \quad (4.8)$$

Here Z_0 is the characteristic impedance of the surrounding transmission lines.

4.2.3 Assembly of the full circulator

Construction of a superconducting version of the model system requires the parallel combination of two of the circuits shown in Fig. 4.2. This process is depicted Fig. 4.3, which shows the model system (Fig. 4.3a) alongside a lumped-element schematic of an equivalent network made with variable inductors and capacitors (Fig. 4.3b).

In principle, a circulator could be created from the gyrator shown in Fig. 4.3b using any of the methods detailed in Sec. 3.4.1. Alternatively, the same circuit could be designed without differential ports, where instead each of the four nodes define their own port via comparison to a common ground, as shown in Fig. 4.3c. Such a design allows direct realization of a four-port circulator, without any additional embedding network. The ideal scattering matrix for this four-port clockwise circulator is

$$\mathbf{S} = \begin{pmatrix} 0 & 1 & 0 & 0 \\ 0 & 0 & 1 & 0 \\ 0 & 0 & 0 & 1 \\ 1 & 0 & 0 & 0 \end{pmatrix}, \quad (4.9)$$

and reversing the direction of gyration also allows the same network to act as a counterclockwise circulator with scattering matrix \mathbf{S}^T . This device is the four-port version of the circulator described in Tab. 3.1.

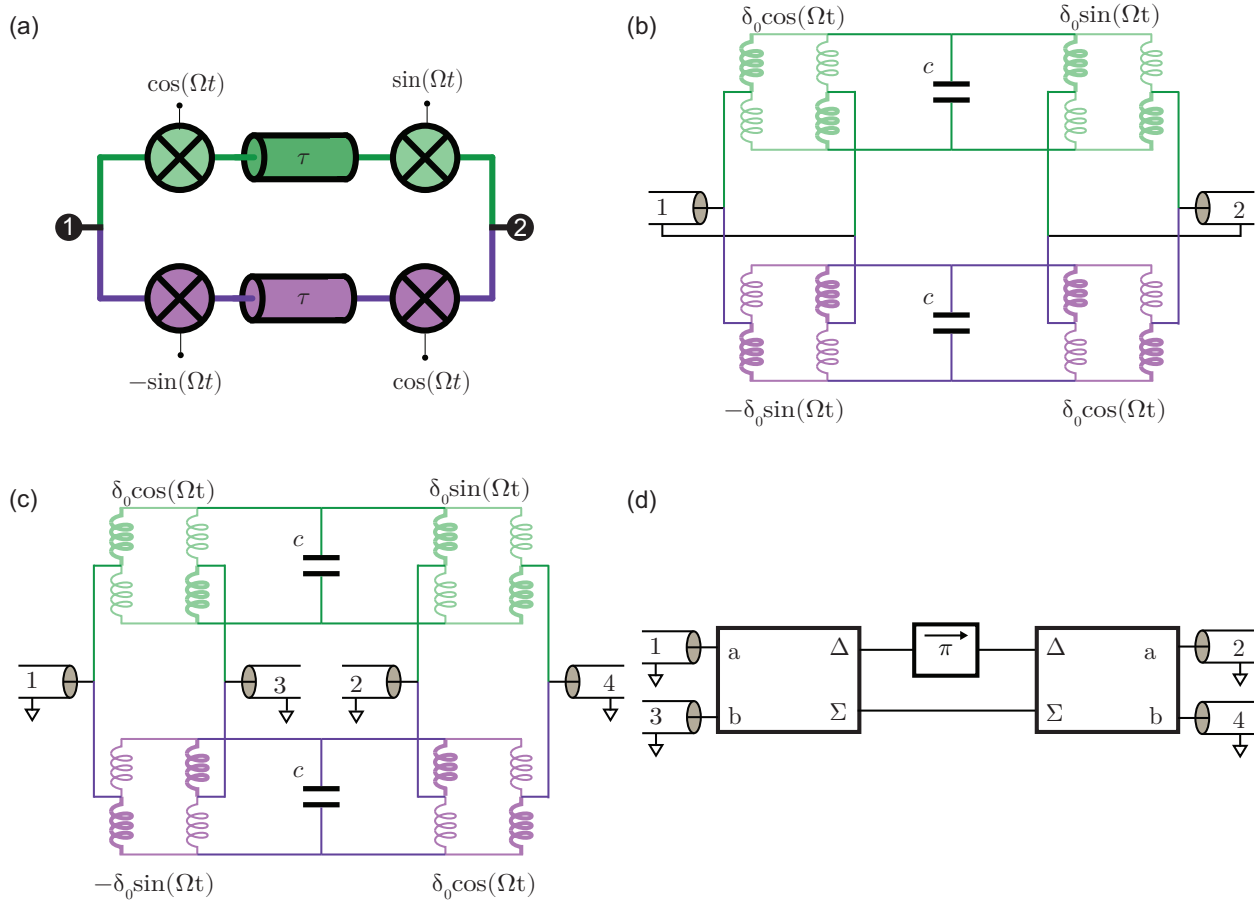


Figure 4.3: (a) The model system of Sec. 4.1 forms a gyator, which breaks Lorentz reciprocity with a combination of frequency conversion and delay. (b) A realization of the network shown in (a), made with tunable, reactive circuit elements. (c) When four ports are formed by comparing the nodes of the circuit in (b) to a common ground, the network forms a four port circulator. Circulation is accomplished through the interference of the common and differential modes of the “left” (ports 1 & 3) and “right” (ports 2 & 4) circuit ports. This is analogous to the circulation generated by a Hogan circulator (d), which comes from the interference between two arms of an interferometer, one of which contains a gyator, and the other of which is a direct short between ports.

The transformation between gyator and circulator can be understood in the following way: driving any one of the four ports in Fig. 4.3c involves simultaneously exciting the common and differential modes of the circuit. The gyrating differential mode is non-reciprocal, whereas the prompt scattering of the non-resonant common mode is reciprocal. The interference of these two scattering processes results in circulation [115].

In a sense, this method for realizing a four-port circulator is a virtual form of the Hogan construction [130] depicted in Fig. 4.3d. In (a physical implementation of) the Hogan construction, an incident signal is routed through a 180° hybrid and directed out its differential (Δ) and common (Σ) ports. The differential port leads to a gyrator and then to the differential port of a second hybrid, whereas the common port is directly connected to the second hybrid's common port. The result is an interferometer with two arms: the Δ arm contains a gyrator (and is therefore non-reciprocal), and the Σ arm is a direct connection between the two microwave beamsplitters, which is reciprocal. The circulator in Fig. 4.3c relies on the same interference effect, but in this case the two “arms” of the interferometer are not spatially separated. Instead, they are encoded in the even and odd excitations of ports 1 & 3 and 2 & 4. In both cases, however, the circulation is accomplished through the interference of a non-reciprocal (gyrating) signal pathway and a reciprocal signal pathway.

4.3 Circuit analysis

We have attempted in the preceding sections to establish intuition for how the circuit in Fig. 4.3c realizes a four-port circulator. To support that argument we now directly calculate the elements of its scattering matrix using circuit theory, following Ref. [115].

Consider the bridge circuit shown in Fig. 4.4a. The constitutive relations for this circuit are

$$\frac{1}{l} \begin{pmatrix} 1 & \delta(t) \\ \delta(t) & 1 \end{pmatrix} \begin{pmatrix} \phi_1(t) \\ \phi_q(t) \end{pmatrix} = \begin{pmatrix} I_1(t) \\ I_q(t) \end{pmatrix}. \quad (4.10)$$

The matrix on the left-hand side of Eq. (4.10) is the reluctance of the circuit. The reluctance matrix gives the current response I_i to an applied flux ϕ_i , defined as the time integral of the voltage at port i : $\phi_i \equiv \int_{-\infty}^t V_i(\tau) d\tau$. It is a sort of inverse inductance, what was historically called “magnetic resistance” before the term “reluctance” was coined by Heaviside [136].

When four of these circuits are connected together, in the manner shown in Fig. 4.4b, the

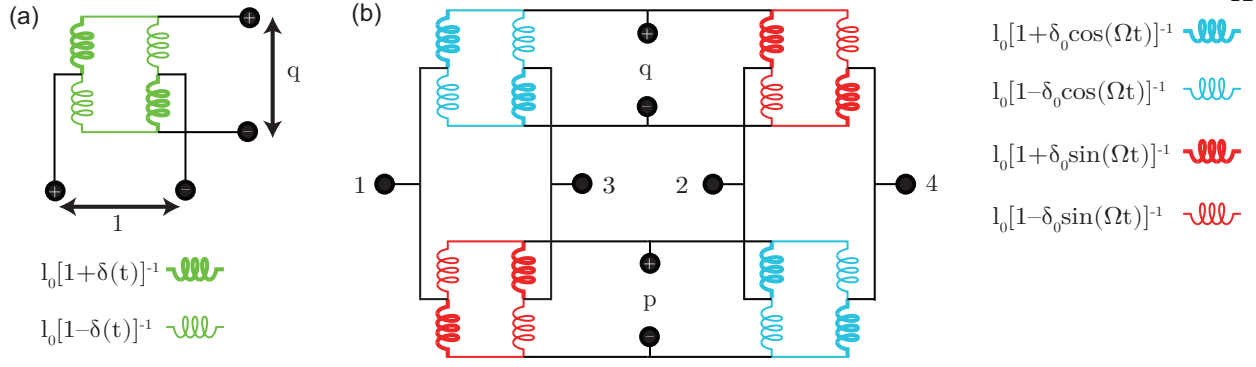


Figure 4.4:

constitutive equation for the network is

$$\frac{\delta_0}{l} \begin{pmatrix} 2/\delta_0 & 0 & \cos(\Omega t) & \sin(\Omega t) & -\cos(\Omega t) & -\sin(\Omega t) \\ 0 & 2/\delta_0 & \sin(\Omega t) & -\cos(\Omega t) & -\sin(\Omega t) & \cos(\Omega t) \\ \cos(\Omega t) & \sin(\Omega t) & 3/\delta_0 & -1/\delta_0 & -1/\delta_0 & -1/\delta_0 \\ \sin(\Omega t) & -\cos(\Omega t) & -1/\delta_0 & 3/\delta_0 & -1/\delta_0 & -1/\delta_0 \\ -\cos(\Omega t) & -\sin(\Omega t) & -1/\delta_0 & -1/\delta_0 & 3/\delta_0 & -1/\delta_0 \\ -\sin(\Omega t) & \cos(\Omega t) & -1/\delta_0 & -1/\delta_0 & -1/\delta_0 & 3/\delta_0 \end{pmatrix} \begin{pmatrix} \phi_p(t) \\ \phi_q(t) \\ \phi_1(t) \\ \phi_2(t) \\ \phi_3(t) \\ \phi_4(t) \end{pmatrix} = \begin{pmatrix} I_p(t) \\ I_q(t) \\ I_1(t) \\ I_2(t) \\ I_3(t) \\ I_4(t) \end{pmatrix}. \quad (4.11)$$

Analysis is simplified by changing to a left-right, even-odd basis for ports 1-4, and a rotating, circular basis for ports p and q :

$$\begin{pmatrix} I_{1,e}(t) \\ I_{r,e}(t) \\ I_{1,o}(t) \\ I_{r,o}(t) \end{pmatrix} = \frac{1}{\sqrt{2}} \begin{pmatrix} 1 & 0 & 1 & 0 \\ 0 & 1 & 0 & 1 \\ 1 & 0 & -1 & 0 \\ 0 & 1 & 0 & -1 \end{pmatrix} \begin{pmatrix} I_1(t) \\ I_2(t) \\ I_3(t) \\ I_4(t) \end{pmatrix}, \quad (4.12)$$

$$\begin{pmatrix} I_+(t) \\ I_-(t) \end{pmatrix} = \frac{1}{\sqrt{2}} \begin{pmatrix} e^{i\Omega t} & -ie^{i\Omega t} \\ e^{-i\Omega t} & ie^{-i\Omega t} \end{pmatrix} \begin{pmatrix} I_q(t) \\ I_p(t) \end{pmatrix}, \quad (4.13)$$

and similarly for the branch fluxes. In these new bases, Eq. (4.11) separates into two uncoupled systems of equations:

$$\frac{2}{l} \begin{pmatrix} 1 & -1 \\ -1 & 1 \end{pmatrix} \begin{pmatrix} \phi_{l,e}(t) \\ \phi_{r,e}(t) \end{pmatrix} = \begin{pmatrix} I_{l,e}(t) \\ I_{r,e}(t) \end{pmatrix}, \quad (4.14)$$

$$\frac{1}{l} \begin{pmatrix} 2 & 0 & \delta_0 & i\delta_0 \\ 0 & 2 & \delta_0 & -i\delta_0 \\ \delta_0 & \delta_0 & 4 & 0 \\ -i\delta_0 & i\delta_0 & 0 & 4 \end{pmatrix} \begin{pmatrix} \phi_+(t) \\ \phi_-(t) \\ \phi_{l,o}(t) \\ \phi_{r,o}(t) \end{pmatrix} = \begin{pmatrix} I_+(t) \\ I_-(t) \\ I_{l,o}(t) \\ I_{r,o}(t) \end{pmatrix}. \quad (4.15)$$

To complete the circulator, we shunt ports p and q with capacitances c . This fixes the relation between the currents and the branch fluxes at these ports:

$$-c \frac{d^2}{dt^2} \phi_{q,p} = I_{q,p}, \quad (4.16)$$

or equivalently in the circular, rotating basis,

$$-c \left(\frac{d}{dt} \mp i\Omega \right)^2 \phi_{\pm} = I_{\pm}. \quad (4.17)$$

With this constraint, Eq. (4.15) has a simple representation in the frequency domain, which we indicate with square brackets $[\cdot]$:

$$\frac{1}{l} \begin{pmatrix} 2 - lc(\omega - \Omega)^2 & 0 & \delta_0 & i\delta_0 \\ 0 & 2 - lc(\omega + \Omega)^2 & \delta_0 & -i\delta_0 \\ \delta_0 & \delta_0 & 4 & 0 \\ -i\delta_0 & i\delta_0 & 0 & 4 \end{pmatrix} \begin{pmatrix} \phi_+[\omega] \\ \phi_-[\omega] \\ \phi_{l,o}[\omega] \\ \phi_{r,o}[\omega] \end{pmatrix} = \begin{pmatrix} 0 \\ 0 \\ I_{l,o}[\omega] \\ I_{r,o}[\omega] \end{pmatrix}. \quad (4.18)$$

At this point we pause and comment on the constitutive relations for the even and odd excitations of the left and right ports of the circuit, given in Eq. (4.14) and Eq. (4.18), respectively. Even excitations of the left and right ports are uncoupled from nodes p and q , and are therefore non-resonant. Contrastingly, odd excitations of the left and right ports depend on the branch fluxes across nodes p and q , and on the value of the capacitors c . These dynamics are resonant. To show that they are also non-reciprocal, we write Eq. (4.18) as a 2×2 system of block matrices

$$\frac{1}{l} \begin{pmatrix} \mathbf{A} & \mathbf{B} \\ \mathbf{C} & \mathbf{D} \end{pmatrix} \begin{pmatrix} \phi_{\pm} \\ \phi_{l,r} \end{pmatrix} = \begin{pmatrix} \mathbf{0} \\ \mathbf{I}_{l,r} \end{pmatrix}, \quad (4.19)$$

where each matrix element in the reluctance matrix is itself a 2×2 matrix (bold variables denote matrices), and the internal degrees of freedom (ϕ_+ and ϕ_-) and the external degrees of freedom ($\phi_{l,o}$ and $\phi_{r,o}$) are contained in the 2×1 vectors $\boldsymbol{\phi}_\pm$ and $\boldsymbol{\phi}_{l,r}$.

Written in this way, it is clear that the internal degrees of freedom $\boldsymbol{\phi}_\pm$ can be eliminated, yielding a 2×2 matrix equation

$$(\mathbf{D} - \mathbf{C}\mathbf{A}^{-1}\mathbf{B}) \boldsymbol{\phi}_{l,r} = \mathbf{I}_{l,r}. \quad (4.20)$$

Expanding this to first order in Ω/ω , and evaluating the output on resonance when ω equals

$$\omega_0 \equiv \sqrt{\frac{4 - \delta_0^2}{2lc}}, \quad (4.21)$$

we obtain the reluctance relation

$$i\omega_0 \frac{16c\Omega}{\delta_0^2} \begin{pmatrix} 0 & 1 \\ -1 & 0 \end{pmatrix} \begin{pmatrix} \phi_{l,o}[\omega] \\ \phi_{r,o}[\omega] \end{pmatrix} = \begin{pmatrix} I_{l,o}[\omega] \\ I_{r,o}[\omega] \end{pmatrix}. \quad (4.22)$$

This is the reluctance relation of a gyrator, with gyration conductance $16c\Omega/\delta_0^2$ [129]. For harmonic fields, the reluctance matrix is $i\omega\mathbf{Y}$, where \mathbf{Y} is the system's admittance matrix.

If ports 1 through 4 are now connected to transmission lines of characteristic impedance Z_0 , the network's scattering matrix \mathbf{S} can be calculated:

$$\mathbf{S} = (1 + Z_0\mathbf{Y})^{-1} (1 - Z_0\mathbf{Y}). \quad (4.23)$$

Here, 1 is the 2×2 identity matrix. Using this expression, the scattering matrix S_o (here the subscript indicates the odd or differential two-port network) for the reluctance relation in Eq. (4.22) is

$$\mathbf{S}_o = \begin{pmatrix} 0 & -1 \\ 1 & 0 \end{pmatrix} \quad (4.24)$$

provided that the gyration conductance is set to Z_0^{-1} . Repeating this process for the even dynamics in Eq. (4.14), the even scattering matrix is

$$\mathbf{S}_e = \begin{pmatrix} \frac{\omega l}{\omega l - 4iZ_0} & \frac{4Z_0}{4Z_0 + i\omega l} \\ \frac{4Z_0}{4Z_0 + i\omega l} & \frac{\omega l}{\omega l - 4iZ_0} \end{pmatrix}, \quad (4.25)$$

which to zeroth order in $\omega l/Z_0$ is the scattering matrix of a direct (matched) connection between the left and right ports:

$$\mathbf{S}_e = \begin{pmatrix} 0 & 1 \\ 1 & 0 \end{pmatrix} + \mathcal{O}\left(\frac{\omega l}{Z_0}\right). \quad (4.26)$$

Finally, the full 4×4 scattering matrix in the numbered port basis can be recovered by reversing the change-of-basis procedure:

$$\mathbf{S} = \mathbf{U}^{-1} \mathbf{S}_{e,o} \mathbf{U}, \quad (4.27)$$

where \mathbf{U} is the unitary matrix in Eq. (4.12) that transforms between the even-odd and numbered port bases, and $\mathbf{S}_{e,o}$ is a 4×4 block-diagonal scattering matrix formed from the 2×2 scattering matrices of the even and odd dynamics:

$$\mathbf{S}_{e,o} = \begin{pmatrix} \mathbf{S}_e & \mathbf{0} \\ \mathbf{0} & \mathbf{S}_o \end{pmatrix}. \quad (4.28)$$

When \mathbf{S}_e and \mathbf{S}_o are given by Eq. (4.26) and Eq. (4.24), Eq. (4.27) reduces to the scattering matrix for an ideal four port counterclockwise circulator, the transpose of the expression in Eq. (4.9). The same result can be obtained via a time-domain analysis in an input-output formalism [115], but we do not reproduce that treatment here.

Chapter 5

Circulator Layout

In this chapter we discuss the layout of the superconducting microwave circulator described in Ch. 4. Many of the design considerations are common to a variety of other monolithic microwave integrated circuits. Others are rooted in the device's use of superconducting materials, and superconducting tunnel junctions. Before we enumerate these considerations, and the design measures undertaken to address them, we give a brief summary of the overarching design philosophy adopted in this project, and the trilayer process used to fabricate the devices. We then describe the design's evolution over the course of four design and measurement cycles.

5.1 Design philosophy

The construction of a superconducting circulator is part of a broader effort within our group to improve the measurement of superconducting qubits with a hierarchical, network-based approach. In the past three years, this has led to proposals for superconducting [115] and broadband [116] circulator designs; and an autonomous feedback scheme for qubit state preparation and preservation [137]; as well as superconducting demonstrations of single-pull, single-throw switches for in-fridge signal processing [131]; cross-over switches for code-domain multiplexing of qubit readout [131]; single-sideband modulators for frequency-domain multiplexing of qubit readout [132]; and cryogenic circulators [138].

These experimental efforts are greatly enhanced by a collaboration with the Quantum Devices group at the National Institute of Standards (NIST) in Boulder. The superconducting circuits

for the above demonstrations were fabricated at NIST in a standard niobium trilayer process (see Sec. 5.2). The design rules for this process (listed in App. B) impose some constraints on our layouts, but the process is wafer-scale, high-yield, and allows for multiple wiring layers and thousands of Josephson junctions on a single chip [139].

The complexity that the process affords is therefore quite powerful. But undisciplined application of that complexity makes it difficult to maintain microwave hygiene and retain physical intuition about a circuit. To leverage the advantages of the trilayer process while avoiding these pitfalls, we construct integrated circuits from repeated instances of the same basic circuits, with hierarchy utilized whenever possible. For example, the bridge-circuit multiplying element discussed in Sec. 4.2.1 functions as a single microwave switch [131], but two instances of the bridge circuit can be embedded between a pair of microwave hybrids to create a single-sideband modulator [132], and four instances can be used to create a tunable [115, 138] or broadband [116] circulator. Other primitives developed in the lab, such as the nonlinear resonator formed from an array of Josephson junctions in series with a capacitance (dubbed a tunable Kerr circuit), have similarly been instanced in the construction of parametric amplifiers [140, 24], tunable couplers for mechanical oscillators [141], and autonomous feedback controllers [137]. The bridge circuits and tunable Kerr circuits are themselves composed of repeated instances of SQUIDs, made up two Josephson junctions in parallel.

5.2 The Nb/AIO_x/Nb trilayer process

The circuits and structures discussed in this thesis were designed with open source layout software (KLayout), and fabricated by Leila Vale at the NIST Boulder cleanroom using optical lithography and a standard Nb/AIO_x/Nb trilayer process [142, 143]. Circuit boards for the chips were also designed in KLayout, and printed by Sierra Circuits on a Rogers 3010 substrate.¹

Tab. 5.1 overviews the design layers available within the trilayer process.

¹ KLayout produces gds2 files which can be converted to the gerber format preferred by boardhouses with standard software PCB software, such as LinkCad.

Table 5.1: Names, abbreviations, materials, and functions of the layers used in the NIST niobium trilayer process. Layers are in process-order. a-Si stands for amorphous silicon.

layer name	abbrev.	material	function
counter electrode	CE	Nb	The counter (upper) electrode for Josephson junctions.
counter electrode overflash	CEO	Nb	Overflash mask for the counter electrode.
aluminum	AL	Al	Aluminum layer that supports a surface oxide, which forms the insulating barrier for the Josephson junctions.
aluminum overflash	ALO	Al	Overflash mask for aluminum.
base electrode	BE	Nb	The base (bottom) electrode for Josephson junctions. Also serves as the primary wiring layer.
normal metal	R1	Au, Cu, or AuPd	Normal metal layer helpful for breaking supercurrent loops or engineering dissipation.
insulator 1	I1	SiO ₂ , Si ₃ N ₄ , or a-Si	Etch of first PECVD dielectric layer for creation of vias between BE and W1.
wiring 1	W1	Nb	Secondary niobium wiring layer.
insulator 1 excess	I1X	SiO ₂ , Si ₃ N ₄ , or a-Si	Additional etch to remove excess dielectric in the first PECVD layer.
insulator 2	I2	SiO ₂ , Si ₃ N ₄ , or a-Si	Dielectric etch for creation of vias between W1 and W2.
wiring 2	W2	Nb	Tertiary niobium wiring layer.
insulator 2 excess	I2X	SiO ₂ , Si ₃ N ₄ , or a-Si	Additional etch to remove excess dielectric in the second PECVD layer.

5.2.1 Josephson junctions in the trilayer process

As the name suggests, the process allows for the creation of superconducting circuits with superconducting-insulating-superconducting Josephson tunnel junctions [58], formed by sandwiching niobium layers around an insulating aluminum oxide. Fig. 5.1 shows the layer stack-up for this process, which begins with thermal growth of an oxide layer on a circular silicon chip (diameter 3", relative electric permittivity $\epsilon_r = 11.45$).² The trilayers are then deposited in a load-locked vacuum system, with an oxidation step after the aluminum deposition to create the aluminum oxide layer. The result is a “vertically” oriented Josephson junction which spans the entire wafer, oriented such that at sufficiently cold temperatures, cooper pairs may tunnel back and forth between the stacked layers of niobium. The lower niobium layer, known as the base electrode, also serves as the primary wiring layer for the circuit. The upper niobium layer is called the counter electrode.

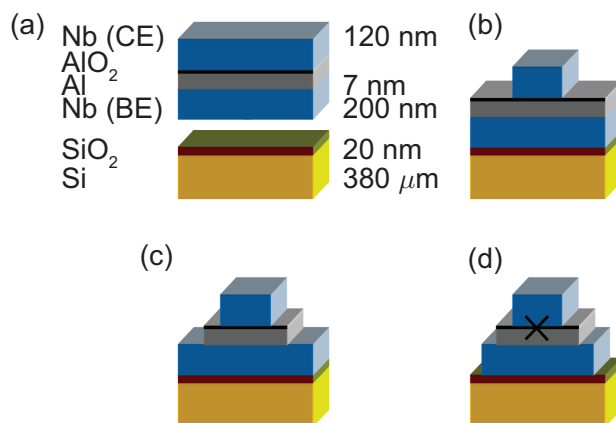


Figure 5.1: Josephson junctions in the Niobium trilayer process. (a) Layer stack-up of the trilayer. (b) The counter-electrode etch. (c) The aluminum/aluminum oxide etch. (d) The base electrode etch. The junction, indicated by the black ‘x’, is formed at the aluminum oxide interface. Graphics courtesy of Maxime Malnou.

The circuit is then defined via a subtractive process. First, a stepper flashes the counter electrode mask. To reduce the amount of counter electrode which unintentionally survives the subsequent etch, a second mask (the counter electrode overflash) is also flashed. This step is less

² This oxide growth is sometimes performed at NIST, and sometimes done by an external vendor—recently, Rogue Valley Microdevices.

about overcoming inconsistencies in the photoresist’s reaction with light, and more about making the process robust to imperfections in the masks. It helps ensure that no “extra” unwanted junctions remain on the wafer.

The same process is then repeated with the aluminum layer, including an additional mask for an aluminum overflash. Finally, the base electrode mask is also flashed, and the niobium is etched, leaving the desired pattern of Josephson junctions, as well as any circuit wiring done on the base electrode layer. If the circuit includes any normal metal (the R1 layer), this is now deposited, masked, and etched, leaving only the pattern defined by the R1 mask.

5.2.2 SQUID arrays in the trilayer process

To form SQUIDs from these Josephson junctions, four junctions are arranged at the corners of a rectangle, as illustrated in Fig. 5.2a. A dielectric is then deposited via an electron cyclotron resonance plasma enhanced chemical vapor deposition (PECVD) process (Fig. 5.2b). Vias to the junction counter electrodes are etched through this layer (defined with the I1 mask), and a secondary niobium layer, called W1, is deposited on top of the dielectric and etched according to the W1 mask (Fig. 5.2c). This niobium layer galvanically connects the four counter electrodes. Finally, an additional etch removes the excess dielectric in portions of the circuit that contain neither SQUIDs nor the W1 layer, reducing dielectric loss.

The result of this process is a series-array of two SQUIDs, each formed from a pair of Josephson junctions (Fig. 5.2e). Current in the first SQUID flows from the base electrode up to the first wiring layer, and then flows back to the base electrode through the second SQUID. Longer arrays of SQUIDs may be created with multiple instances of this pattern. Secondary wiring can also be accomplished on the W1 layer. Fig. 5.3 shows a layout view for a cell containing a series-array of two SQUIDs, as depicted schematically in Fig. 5.2.

This cell was used to create the SQUID arrays in the fourth-generation circulator. The Josephson junctions are 2 by 2 microns with nominal critical current density $0.48 \mu\text{A}/\mu\text{m}^2$, yielding $1.92 \mu\text{A}$ junctions and SQUIDs with maximum critical current of $3.84 \mu\text{A}$.

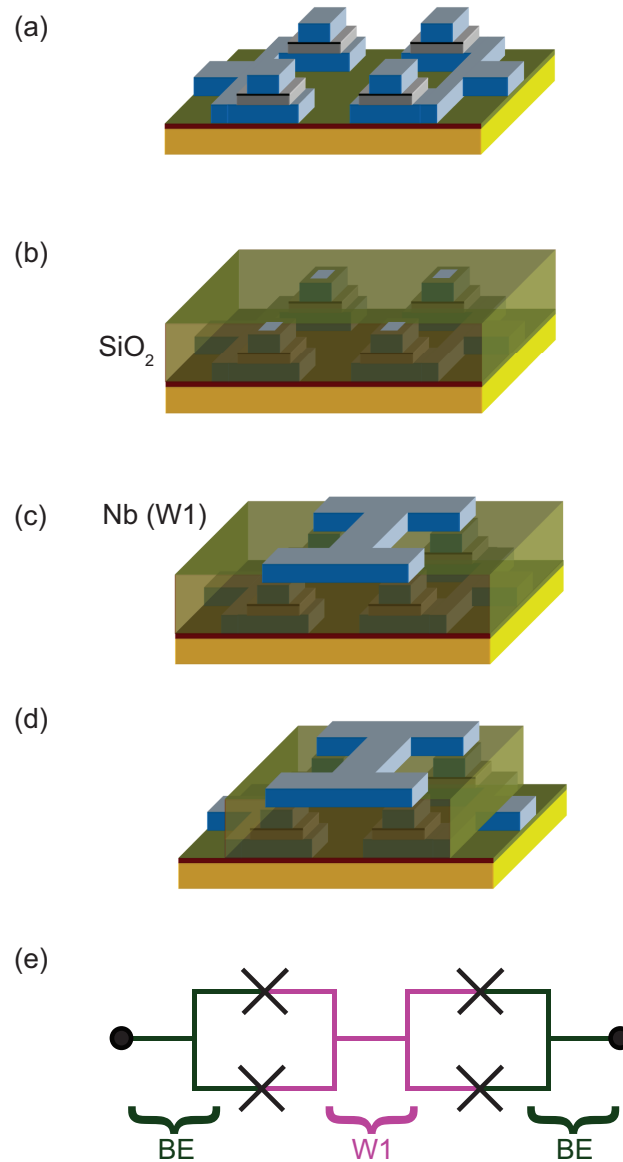


Figure 5.2: SQUIDs in the Niobium trilayer process are fabricated in pairs. (a) Four Josephson junctions are arranged on the corners of a rectangle. (b) A 300 nm-thick layer of dielectric (silicon oxide, in this case) is deposited on the wafer. This is the layer of insulation etched by I1 and I1X. (c) Vias (defined by I1) are etched through the dielectric layer to the junction counter electrodes. These vias are obscured in the figure by the W1 layer, and are not visible. A third layer of niobium—the W1 layer—is then deposited on top of the silicon oxide, and etched with the mask defined by W1. (d) A second etch on the silicon dioxide (defined by I1X) removes excess dielectric. (e) The result of this process is a series-array of two SQUIDs. Current in the first SQUID flows from the base electrode up to the first wiring layer, and then flows back to the base electrode through the second SQUID. Trilayer graphics courtesy of Maxime Malnou.

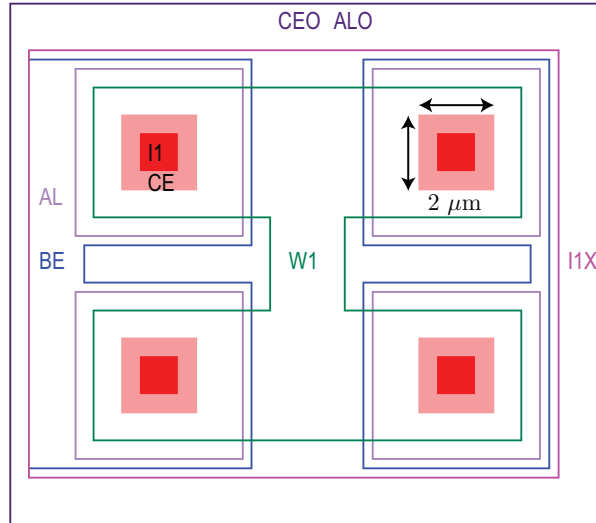


Figure 5.3: Layout of the SQUID cell used in the fourth-generation circulator, depicted schematically in Fig. 5.2. The CEO and ALO layers are directly on top of one-another, and demarcated by the largest rectangle.

Typical variation in junction critical currents with the NIST trilayer process is below 5% for junctions less than 1 mm apart. Furthermore, the frequency of high critical current outliers is also low: less than 1% of junctions have critical currents that exceed the target value by more than 30%. As the tunable inductors needed to realize the bridge circuit multipliers are formed by arrays of SQUIDs, the variation in array inductance is further reduced by averaging: if variations in the junction critical current are assumed to be uncorrelated across the array, an array of N SQUIDs will have a fractional uncertainty in its total inductance which is $1/\sqrt{2N}$ times the fractional uncertainty of the inductance of a single junction.

5.2.3 Additional wiring layers

If a tertiary wiring layer is desired, a second PECVD dielectric layer is then deposited. Vias (defined by the I2 mask) are etched through this layer, and a fourth niobium layer, W2, is then deposited and etched, leaving only the wiring pattern defined by the W2 mask. A final dielectric etch (defined by I2X) removes the excess dielectric everywhere except below W2.

5.2.4 Best practices for trilayer process layout

We conclude discussion of the trilayer process with a list of “best-practices” for trilayer layout. Many of these are specific to the equipment and practices at NIST Boulder, but some are more broadly applicable to general layout of superconducting circuits.

- Although BE, W1, and W2 are all composed of niobium, they are deposited on different substrates, and this gives the BE layer qualitatively different material properties from W1 and W2. (BE is deposited on thermally grown silicon oxide, whereas W1 and W2 reside on dielectrics deposited with a plasma-enhanced, chemical vapor deposition technique.) In particular, BE has lower dielectric losses than W1 and W2. For this reason,
 - * Circuit connectivity should be done whenever possible on BE.
 - * If a crossover is needed between the bias lines and microwave lines, make sure that it is the bias lines that make the cross over, since loss is typically more tolerable in that channel.
 - * Crossovers should be as short as possible. A good rule of thumb is to place vias $2\ \mu\text{m}$ away from the line which is being crossed.
- When making resistors with normal metal, one must consider the superconducting-normal metal-superconducting junction physics caused by the induced superconductivity of the proximity effect. A detailed discussion of this is deferred to Sec. 5.3.2. But the induced quasiparticle transport in the superconductors must also be considered. When possible, widen niobium traces that have normal metal overlap to mitigate this effect.
- Different layers should not share edges.
- The wafer dicing saw has a width of $40\ \mu\text{m}$. When designing chips, move the edge of the design $20\ \mu\text{m}$ in from the die edge. This facilitates dicing and prevents problems such as ground plane peeling, and can be accomplished by including alignment marks of width $20\ \mu\text{m}$ on the corners of the chip design.

- In general, geometric splits (e.g. variations in number of SQUIDs or capacitor dimensions) are easy to fabricate, whereas splits with different materials, oxidation time, or numbers of layers are more time consuming. When possible, design splits with geometric variations. For example, to design a spread of resonance frequencies in a wafer of our circulators, vary the capacitor dimension, not the critical current density of the Josephson junctions. Limit geometric splits to 6 or less, when possible. Splits should be labelled with names that are explanatory, but also easily distinguishable for collaborators not familiar with the work. For example, in a wafer with four splits, the labels
A_Cap95Res10, B_Cap95Res15, C_Cap115Res10, and D_Cap115Res15
are preferable to the labels
Cap95Res10, Cap95Res15, Cap115Res10, and Cap115Res15.
- To avoid lift-off problems, do not layout W1 or W2 layers above the R1 layer. This can be done by removing the normal metal directly beneath the wiring layer.
- Normal metal should be more than 4 μm away from vias.
- Vias from W2 to BE should be done in two steps, and not a single tall via.
- Avoid designs with different chip sizes on a single wafer.
- Utilize hierarchy; design with cells.
- Consider the effect of trapped flux upon cooling through the superconductor's critical temperature T_c . This can be done rapidly by comparing the equipartition energy $k_B T_c/2$ to the energy stored in the magnetic degree of freedom for one loop in the circuit, $\Phi_0^2/2L$, with L the inductance of the loop. If $k_B T_c/2 > \Phi_0^2/2L$ the available thermal energy will excite higher energy flux states as the circuit cools through T_c , and each time the device cools down it will be initialized in a different state.
- Consider the effect of vortex formation as superconducting films are cooled through their transition temperature T_c . Ref. [144] provides a rule of thumb for this process in designs

with niobium: in a magnetic field B_0 , vortex formation is suppressed in a niobium microstrip of width w when $B_0 w^2 < \Phi_0 = h/(2e)$.

5.3 Design considerations

Broadly speaking, the three major challenges in the layout of a superconducting circulator based on the approach discussed in Ch. 4 are

- (1) retaining circuit symmetry,
- (2) maintaining the stability of the flux environment, and
- (3) suppressing the coupling between the microwave signal lines and the radio-frequency bias lines.

In this section, we detail the design measures undertaken to overcome these difficulties.

5.3.1 Capacitor design

To realize capacitors of capacitance c for the circulator’s lumped element representation (Fig. 4.3c), we layout parallel-plate capacitors in a metal-insulator-metal geometry with niobium plates sandwiched around the dielectric SiO_2 (Fig. 5.4a). In the frequency range of 4 to 8 GHz, roughly pF capacitances are required to create capacitor-impedances near 50 Ohms. Making a pF capacitor with SiO_2 in the Nb trilayer process requires capacitor plates that are roughly 100 μm on a side—large enough to trap magnetic flux vortices when cooled through niobium’s superconducting transition temperature T_c in earth’s magnetic field [144].

To avoid trapping flux vortices, we pattern slots in the capacitor electrodes, such that the Nb strips that form the electrodes never exceed a width $w \ll 100 \mu\text{m}$. This ability to suppress vortices in non-zero magnetic fields is important for our layout, as the circulator is actuated with flux controls which can be spoiled by a static and unremovable flux gradient. Choosing $w = 5 \mu\text{m}$ ensures that the capacitor electrodes trap no magnetic flux vortices when the capacitor is cooled through T_c in our experiment’s modestly shielded magnetic environment.

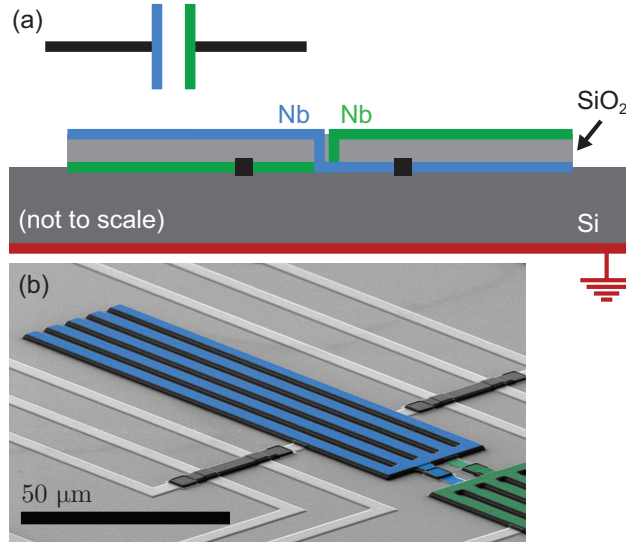


Figure 5.4: Capacitor design. (a) Schematic illustrating the symmetrization of the parallel plate capacitors used in the device. To create a capacitor c , two capacitors with half the desired capacitance are connected in parallel, such that the upper (lower) plate of the first capacitor is galvanically connected to the lower (upper) plate of the second. This procedure gives each side of the capacitor the same parasitic capacitance to the ground plane. (b) False-color scanning electron microscope image showing one of the $c/2$ capacitors used in the fourth-generation device (blue), and the joint connecting it to another $c/2$ capacitor (green), as described in (a). The plates in both capacitors are formed from narrow niobium strips of width $w = 5 \mu\text{m}$ to prevent trapping flux vortices [144].

To further symmetrize the circuit, each parallel-plate capacitor is then divided into two capacitors of capacitance $c/2$, and connected in parallel, such that the upper plate of the first (second) capacitor is galvanically linked to the lower plate of the second (first) capacitor (Fig. 5.4b). This procedure gives each side of the composite capacitor the same parasitic capacitance to ground, and is essential for preserving the symmetry on which the concept of the device relies.

A scanning electron microscope image of a capacitor is shown in Fig. 5.4b, which shows the Nb strips that form the top plate of one of the $c/2$ parallel plate capacitors. In the right side of the image, the capacitor is connected to a second parallel plate capacitor (mostly out of view) in the manner described above.

5.3.2 Use of normal metal

Superconducting loops in the circulator can trap magnetic flux and lead to an unstable flux environment, interfering with the flux biasing used to control the device. To avoid trapping unwanted flux, we layout the circulator using small amounts of a normal metal—in earlier version of the circulator, gold-palladium, and in later versions, gold. Fig. 5.5 illustrates the effect of using normal metal in this way: it shows measurements of the phase of forward transmission as a function of a static gradiometric flux Φ_g , in two circulators which are identical except for the absence (Fig. 5.5a) or presence (Fig. 5.5b) of normal metal. The phase wrap of the resonant delay is visible in both devices, but in Fig. 5.5a, the circuit’s resonant frequency shifts from scan to scan, resulting in jagged edges visible in the transmission’s phase. In contrast, the phase in Fig. 5.5b is stable from scan to scan, which we interpret as evidence of a a stable flux-environment.

The thickness (height) of the gold layer is $d = 225$ nm, giving it a sheet resistance of 60 mOhms/square. To reduce resistive losses in this layer, 11 Au squares are placed in parallel, yielding a total film resistance of about 10 mOhms. Four of these resistors are placed in each Wheatstone bridge (resistor symbols in Fig. 5.6b) to break supercurrent loops and maintain the symmetry required by the circuit. Estimates with time-domain numerical simulations (Simulink) indicate that the addition of these resistors causes the dissipation in the circuit to increase by 0.1 dB, limiting the internal Q of the circuit to be less than 2000.

To design the normal metal resistors in a way that prevents proximitization by the nearby niobium, the resistor lengths l —defined as its dimension parallel to the flow of current—is constrained to be $l \gg \xi_d$. Here ξ_d is the coherence length of Au calculated in a dirty limit, where the metal film’s mean free path l_n is less than the clean-limit coherence length [145]

$$\xi_c = \frac{\hbar v_F}{2\pi k_B T}. \quad (5.1)$$

In the above, v_F is the Fermi-velocity of the metal, k_B is Boltzmann’s constant, and T is the metal’s temperature. We justify this treatment with the observation that the Au film’s mean free path $l_n \approx 600$ nm $\ll 6$ μ m $\approx \xi_c$. This estimate for ξ_c is made with the assumption that $v_F = 1.4 \times 10^6$

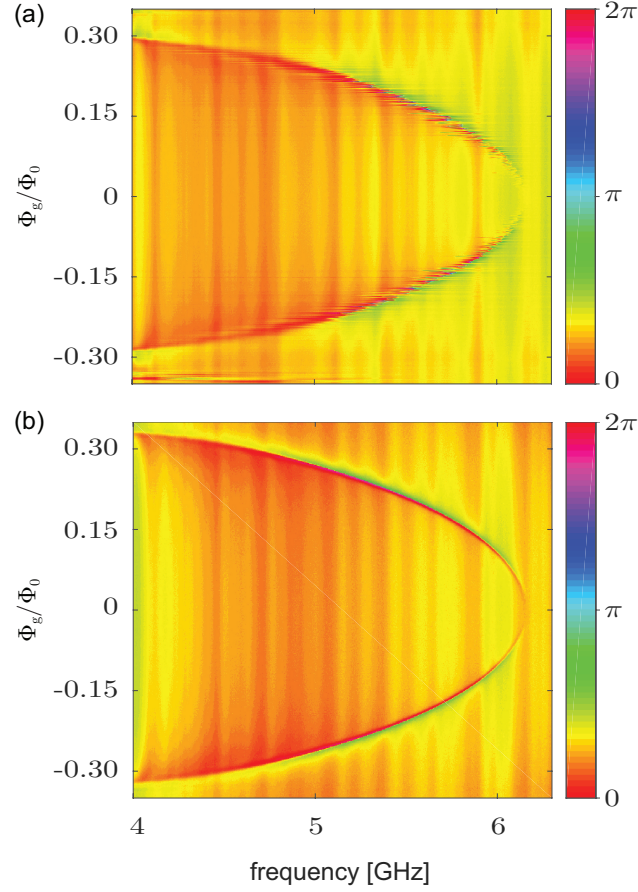


Figure 5.5: The effect of normal metal on the stability of a circulator’s resonant modes. (a) The phase of forward transmission $\angle S_{21}$ as a function of probe frequency and a static gradiometric flux Φ_g , with Φ_u fixed at $0.2\Phi_0$. The device under test is a fourth-generation circulator design, identical to that discussed in Ch. 6, with the exception that it contains no normal metal. (b) The same measurement as (a) on a fourth-generation circulator with normal metal inserted into the bridge circuits, as described in the text.

m/s in Au [146], and the temperature T set to 300 mK. The mean free path is calculated with the Drude model [146] and the film’s resistivity.

In the dirty-limit, the coherence length ξ_d is essentially a geometric mean of the clean-limit coherence length and the metal’s mean free path [145]:

$$\xi_d = \sqrt{\frac{l_n \xi_c}{3}}, \quad (5.2)$$

which comes out to $\xi_d \approx 1 \mu\text{m}$ for the above values of ξ_c and l_n . This value is comparable with

measurements of the dirty-limit coherence length in thin films of a similar elemental metal, copper, when one corrects for sample thickness [147, 148].

The condition $l \gg \xi_d$ can be made quantitative with consideration of the superconducting-normal-superconducting (SNS) junction physics which govern the Nb-Au-Nb interface. Unlike a superconducting-insulator-superconducting junction, which is governed by an energy scale set by the superconducting gap, the natural energy scale for the proximity effect in an SNS junction is the Thouless energy [148]. For junctions of reasonable size ($l > \xi_d$), the critical current of the SNS junction is

$$I_n = \frac{2\pi k_b T}{R_n q} \left(\frac{\xi_d}{l} \right)^2 e^{-l/\xi_d} e^{-l/l_\phi}. \quad (5.3)$$

Here q is the electron charge, R_n is the room temperature resistance of the junction, $l_\phi \approx 2 \mu\text{m}$ is the inelastic scattering length of gold at 300 mK [149], and the Thouless energy is expressed in terms of the coherence length ξ_d and the junction length l . The critical current I_n sets the Josephson energy $E_J = \varphi_0 I_n$ of the SNS junction, and the resistance R of the junction scales in relation to the Josephson energy and the energy in the thermal environment:

$$R = R_n e^{-E_J/k_B T}. \quad (5.4)$$

Along with the Josephson inductance of a SQUID array (Eq. (4.4)), the resistance in Eq. (5.4) sets an L/R time which characterizes the time required for trapped-flux to dissipate out of the circuit. Choosing $l > 5.5\xi_d$ ensures that L/R time is less than 1 second. In preliminary designs, we therefore set $l = 10 \mu\text{m}$. In later designs we found experimentally that $l = 5 \mu\text{m}$ also prevents flux-trapping, likely due to a dirty-limit coherence length which is less than our $1 \mu\text{m}$ estimate. The device presented in the following chapter has $l = 5 \mu\text{m}$.

5.3.3 Bias line design

The circulator's active components are actuated with flux controls created by a pair of on-chip bias lines. Design of these bias lines involves two important layout considerations: namely, isolating

the microwave fields from the bias lines, and preventing the RF bias signals from interfering with the operation of the microwave circuit.

Isolating the circulator’s microwave fields from the bias lines is important because from the perspective of the microwave circuit, coupling to the bias lines acts as an additional loss channel. To reduce losses of this kind low-pass filters (20 nH spiral inductors) are inserted into the bias lines as they enter and exit the chip (pink inductor symbols in Fig. 5.6a). These simple filters present an impedance of approximately 15 Ohms to the bias signals at $\Omega = 2\pi \times 120$ MHz, whereas at microwave frequencies in the 4 to 8 GHz band their impedance exceeds 500 Ohms. Simulations using commercial planar method-of-moments solvers (AWR Microwave Office) indicate that these filters limit microwave transmission out the bias lines to less than -20 dB.

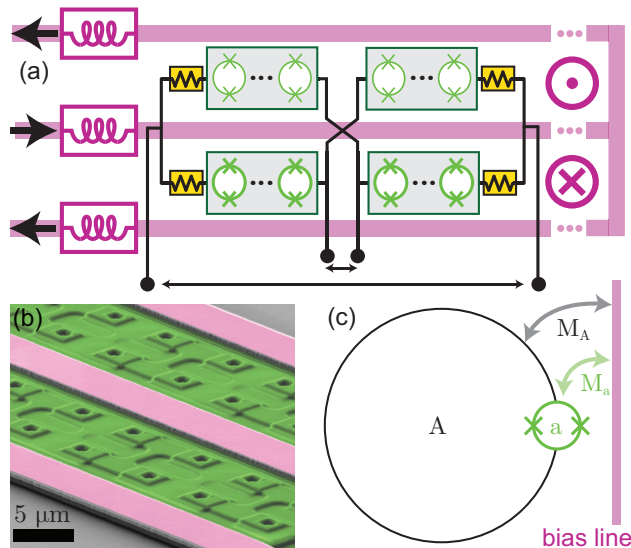


Figure 5.6: (a) Schematic showing the position of normal metal resistors in the inductive bridges, and the routing of a quadrupole-source bias line which couples strongly to the SQUIDs it encloses and weakly to surrounding loops of the circuit. (b) False color scanning electron microscope image showing two adjacent SQUID arrays (green) and the microstrip lines (pink) that flux-bias them. (c) Schematic illustrating the challenge of coupling a bias line strongly to a small SQUID loop while coupling it weakly to a larger circuit loop.

The challenge of the second consideration—preventing bias signals from interfering with the circuit’s microwave operation—is illustrated in Fig. 5.6c. The lumped-element representation of the

circulator (Fig. 4.3c) contains tunable inductors, realized with flux-modulated SQUIDs, as well as larger circuit loops which are (partly) comprised of SQUIDs. For simplicity, we consider the effect of a bias line on one such loop of area A which includes a SQUID with area a inside it (Fig. 5.6c).

To operate the circulator, the bias line must dynamically thread a flux through the SQUID, on the order of a tenth of a flux quantum $\Phi_g \approx \Phi_0/10$, at a rate Ω . If the mutual inductance between the bias line and the SQUID loop is denoted as M_a , this requires an AC bias current with amplitude $I_g \approx \Phi_0/(10M_a)$.

The time-dependent gradiometric flux, however, also threads through the larger circuit loop of area A . Faraday's law describes the electromotive force induced around this loop, which for a cosinusoidal bias current is $\mathcal{E} = \Omega M_A I_g \sin(\Omega t)$. We assume the impedance of the loop Z_A is entirely inductive in origin. The loop inductance L_A is the sum of its geometric L_g and Josephson inductance L_J , which we write in terms of the participation ratio $p \equiv L_A/L_J$ as $L_A = pL_J$, yielding $Z_A = i\Omega p L_J$. Ohm's law then allows a calculation of the AC current induced around the loop of area A , which with the appropriate substitutions has an amplitude of

$$I_{\text{ind}} \approx \frac{2\pi}{10p} \frac{M_A}{M_a} I_s, \quad (5.5)$$

with I_s the critical current of the SQUID.

When the induced currents approach the SQUID critical currents in magnitude, the higher order corrections in Eq. (4.4) become significant, and when it exceeds the critical currents, the SQUIDs become dissipative elements. From Eq. (5.5) one can see that the bias signals will couple to the microwave circuit and interfere with the circulator's operation unless the prefactor on the equation's right-hand side is much less than one. The circulator's performance (in particular, the ability to impedance match the device) requires that the participation ratio p not be much greater than one. The only way to satisfy the requirement, then, is to engineer the mutual inductances such that $\frac{M_A}{M_a} \ll 1$. This is challenging, as the size of the parallel plate capacitors and the SQUID arrays mandates that $A/a \approx 10^3$.

To overcome the disparity in loop areas and satisfy the coupling condition $M_A/M_a \ll 1$, we

layout the bias lines in a symmetric way, such that their currents create magnetic quadrupoles. The layout of the shielded bias lines is shown schematically in Fig. 5.6a, and is also visible in the SEM image in Fig. 5.6b. The central bias line, bisecting the bridge, carries the full bias current I_g across the chip, and then splits into two parallel arms, each carrying a current $I_g/2$ on the outside edges of the bridge. As the currents in these lines flow in opposite directions, the magnetic field B_g from this shielded configuration scales as

$$B_g = \frac{\mu_0 I_g}{2\pi r} \left(\frac{\epsilon}{r}\right)^2 + \mathcal{O}\left(\frac{\epsilon}{r}\right)^4, \quad (5.6)$$

where ϵ is the separation between the inner and outer bias lines, and μ_0 is the vacuum permeability. We make ϵ as small as possible in our layouts, given the requirement that the SQUID arrays must reside between the inner and outer bias lines. These constraints result in the choice $\epsilon = 17.5 \mu\text{m}$.

5.4 Design iterations

In the following sections we catalogue the previous design iterations. The intent is to provide some record of the design process chronology, and the insights which led to the design considerations discussed in the preceding section. In the interest of brevity, extensive details about measurements of past devices are not provided. Likewise, details about the experimental set-up are deferred to Ch. 6.

5.4.1 Generation I.

Fig. 5.7 shows a false-color optical micrograph of the first-generation circulator. The micrograph is taken after a protective photoresist is removed from the chip, via a standard sequence of solvent rinses (30 seconds in acetone, 30 seconds in acetone, 30 seconds in isopropanol, dry with nitrogen gas). The main design features and observed performance are summarized in Tab. 5.2.

When the resonant delay was tuned with a static gradiometric flux, its frequency dependence agreed qualitatively with a circuit model. These measurements, however, exhibited a clear hysteresis with respect to the sweep-direction of the bias current, as illustrated in Fig. 5.8.

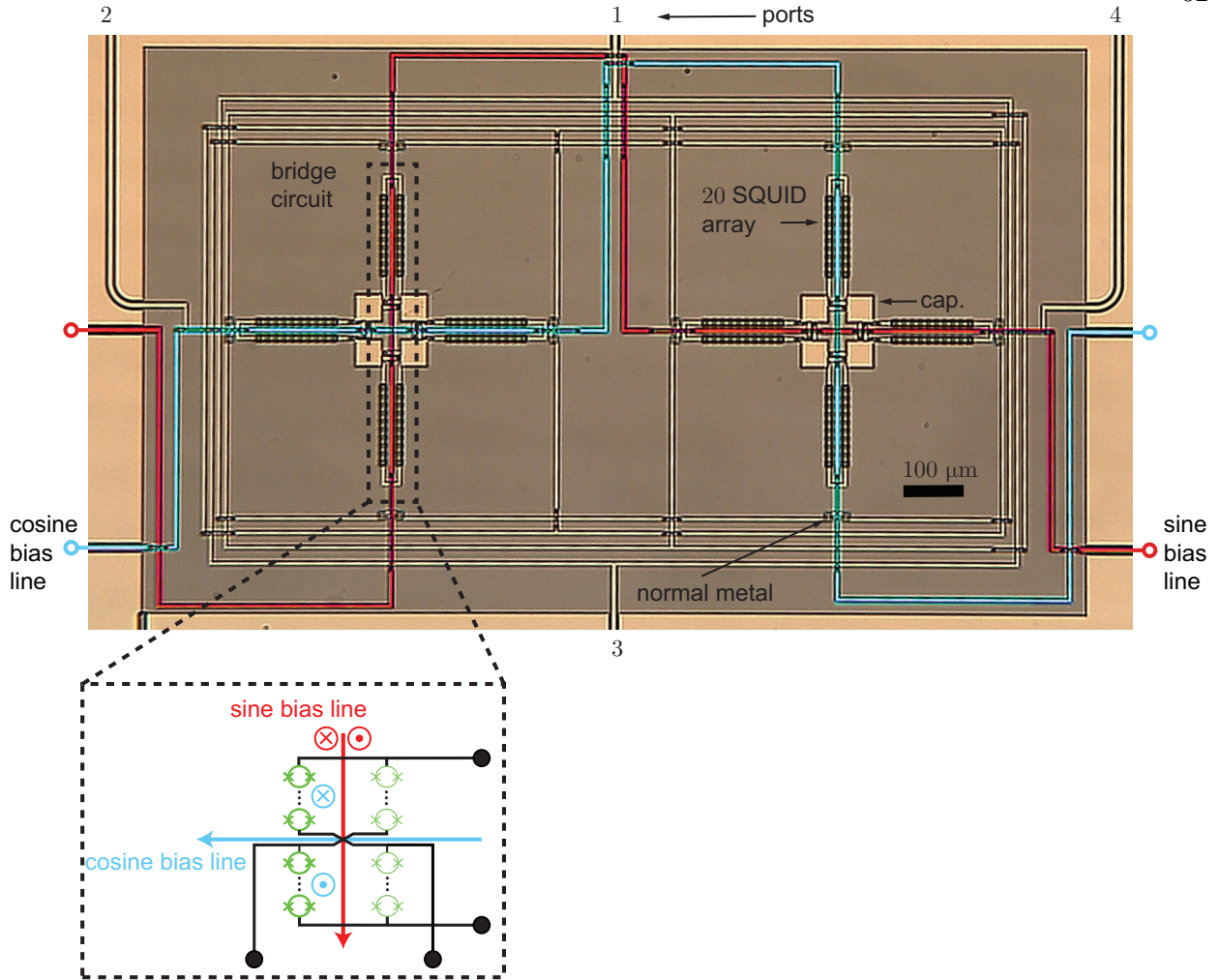


Figure 5.7: False-color optical micrograph of the first-generation circulator layout. The pop-out displays how the cosine bias line couples to a sinusoidally modulated bridge circuit in an undesirable way.

When the device was configured as a gyrator and biased near the operation point expected from theoretical considerations (e.g. with $\phi = \pi/2$, $\Omega\tau = \pi/2$, as described in Ch. 4), the resonant delays were visible. Fig. 5.9a shows the phase of transmission (color), as a function of frequency and the magnitude of the AC gradiometric flux Φ_g . At gradiometric fluxes above $0.08 \Phi_0$, two resonant modes separated by $2\Omega/(2\pi)$ are visible in the plot. At lower gradiometric fluxes, though, the flux environment of the resonator appears to be unstable. The largest non-reciprocity is observed in this unstable region, as shown in Fig. 5.9b, which plots $|S_{21} - S_{12}|$ [dB] over the same region of

Table 5.2: Design features and performance of the first-generation circulator.

Design features	Observed performance
<ul style="list-style-type: none"> • Capacitors symmetrized to balance parasitic capacitance to ground, as described in Sec. 5.3.1 	<ul style="list-style-type: none"> • Resonant modes tune with static flux, in qualitative agreement with circuit model, but exhibit hysteresis
<ul style="list-style-type: none"> • Normal metal (AuPd) inserted to break all supercurrent loops except those inside the bridge circuits, which are suppressed by gradiometry of figure-eight layout (see Sec. 4.2.1) 	<ul style="list-style-type: none"> • Transmission strongly attenuated by dynamical flux modulation

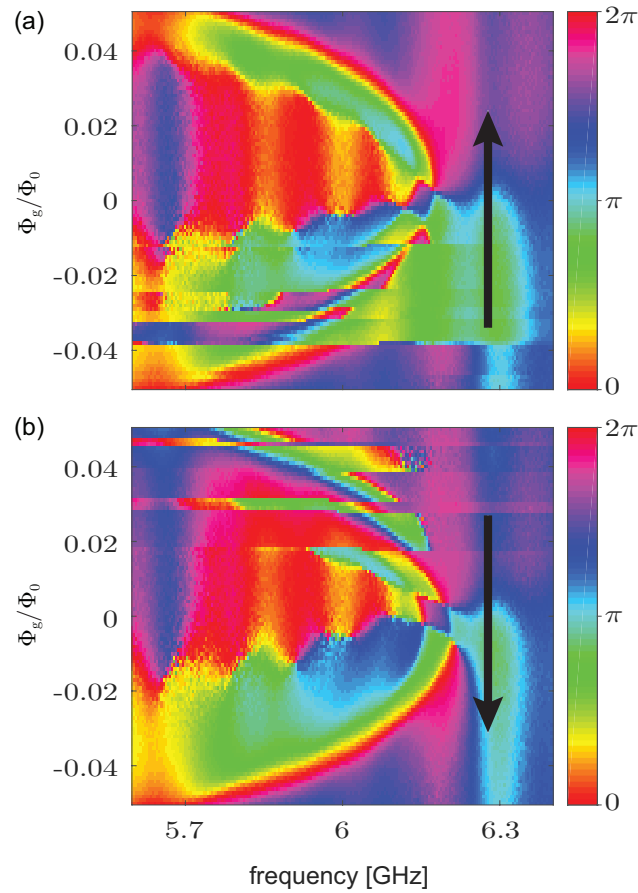


Figure 5.8: Hysteresis in the first-generation circulator with respect to sweep-direction of bias currents. (a) Phase of transmission (color) through the device, as a function of frequency and an *upwardly* swept static gradiometric flux Φ_g . (b) The same measurement, for a *downwardly* swept static gradiometric flux Φ_g .

parameter space. Even there, though, its magnitude is still far from the maximum theoretical value of 3 dB. This is not due to an equality in the phases of forward and reverse transmission, as can be seen in Fig. 5.9c, where $\angle S_{21} - \angle S_{12}$ is displayed for the same measurement.

Hysteresis in the DC flux sweeps and instability and weak transmission in the AC flux sweeps likely resulted from a flux-stability issue. Inspecting the layout in Fig. 5.7, one can see that the cosine (sine) bias line couples strongly to the sinusoidally (cosinusoidally) modulated bridges. This is illustrated in the pop-out below the micrograph. There, the sinusoidal bias line modulates the flux through the SQUIDs in the desired fashion, but does not thread flux through the figure-eight because of the circuit’s gradiometric design (the twist at the center of the figure-eight). The cosinusoidal bias line, however, threads a large flux through the bridge-circuit’s figure eight. As these bridges have no internal normal metal to break super-current loops, and as that coupling threads many flux-quantum through those loops,³ the result is an unstable (and dynamically evolving) flux-environment.

5.4.2 Generation II.

To address this issue, the second generation device was a large-scale redesign. The figure eight-geometry of the bridge circuits was retained, as was the symmetrization of the capacitors, but otherwise the circuit layout was completely rearranged. Fig. 5.10 shows a false-color optical micrograph of the second-generation circulator. The main design features and observed performance are summarized in Tab. 5.3.

In this device, again configured as a gyrator, the observed performance improved dramatically. Transmission was still strongly attenuated (-26 dB of insertion loss), but the resonant delays were visible during AC modulation of the bias currents, and the device exhibited the desired π difference between forward and backward transmission, characteristic of gyrators. Despite these improvements, we still observed instabilities in the flux environment, evident in sub-linewidth-scale

³ To see this, recall that the bias lines are designed to thread a sizable fraction of a flux-quantum through the SQUIDs that they address, and these SQUIDs are orders of magnitude smaller in area than the bridge circuit.

Table 5.3: Design features and performance of the second-generation circulator.

(New) design features	Observed performance
<ul style="list-style-type: none"> • Smaller footprint (tens of nH of geometric inductance eliminated) • New layout allows bias lines to run in straight, parallel lines and drastically reduces mutual inductance between cosine (sine) bias line and sinusoidally (cosinusoidally) modulated bridges • Straight bias lines enabled by inversion of one pair of bridge circuit electrodes, which introduces an effective π phase shift into the modulation (realizing the $-\sin(\Omega t)$ modulation with a sinusoidal bias current) • Slotted parallel-plate capacitors, to suppress the creation of flux vortices, as described in Sec. 5.3.1 	<ul style="list-style-type: none"> • Resonant modes tune with static flux, in quantitative agreement with circuit model • Resonant modes tune with dynamic flux modulation, but shift in frequency from scan to scan by fractions of a linewidth. • Gyration (π phase shift between forward and backward transmission) with -26 dB insertion loss

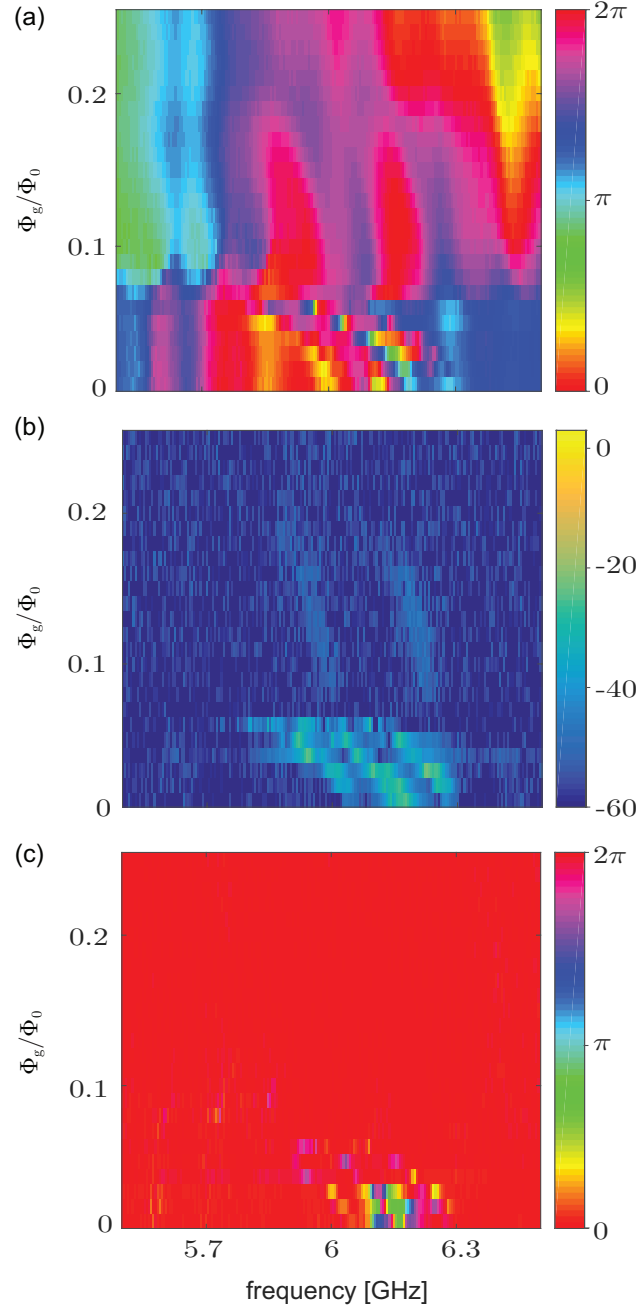


Figure 5.9: AC modulation of the first-generation circulator. (a) Phase of transmission (color) through the device, as a function of frequency and AC gradiometric flux of amplitude Φ_g . (b) Non-reciprocity $|S_{21} - S_{12}|$ [dB] as a function of frequency and AC gradiometric flux of amplitude Φ_g . (c) Angular non-reciprocity $\angle S_{21} - \angle S_{12}$ over the same parameter space.

shifts in the resonant frequency of the circuit between scans.

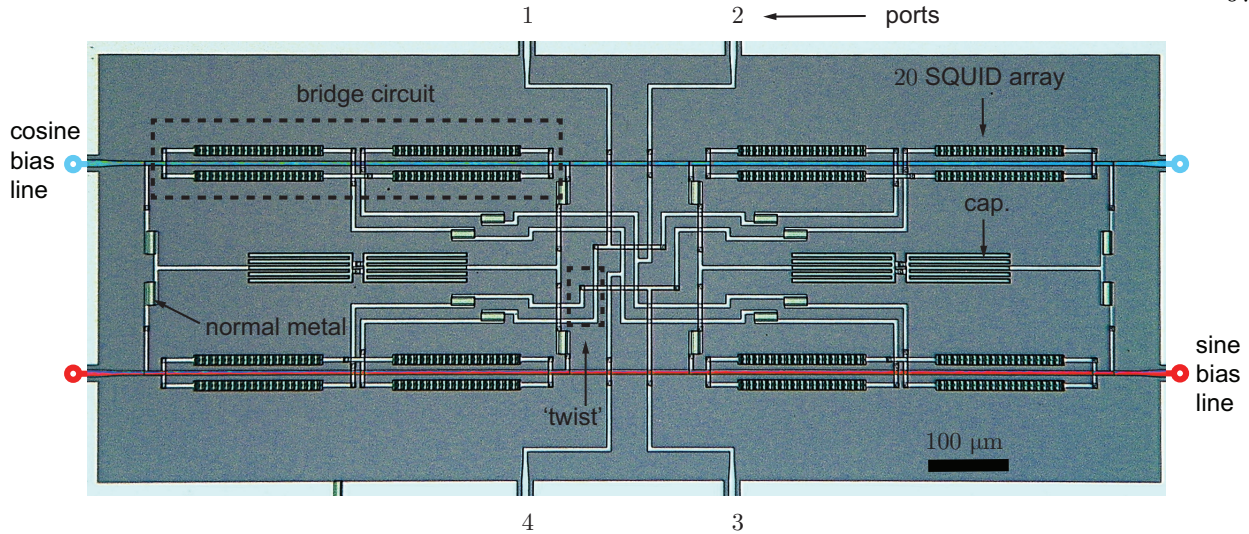


Figure 5.10: False-color optical micrograph of the second-generation circulator layout.

In the first and second generation designs, normal metal had been inserted to break all of the superconducting loops in the circuit, except those within the bridges themselves. The idea behind this had been that as these structures were folded into a symmetrical figure-eight, their gradiometry would prevent the flow of screening currents.

Motivated by the observed flux-instabilities, we reconsidered this conclusion. As the uniform background magnetic field must be strong enough to thread a sizable fraction of a flux quantum through each SQUID, and as the SQUIDs are more than three orders of magnitude smaller in area than the bridge circuits, a gradiometric approach requires gradiometry better than one part in 10^3 . For bridge circuits which are hundreds of microns long and tens of microns wide, that entails fabrication with sub-micron resolution, unachievable with the optical lithography used in the trilayer process. We therefore resolved to move the normal metal into the bridge circuits, and break all of the device's supercurrent loops in the subsequent design cycle.

When considering what limited the insertion loss of the device, we observed that the measured operation point was far from the operation point expected from the theoretical model: namely, $\Omega\tau \ll \pi/2$. Attempts to increase bias frequency Ω or the duration of the resonant delay τ (which

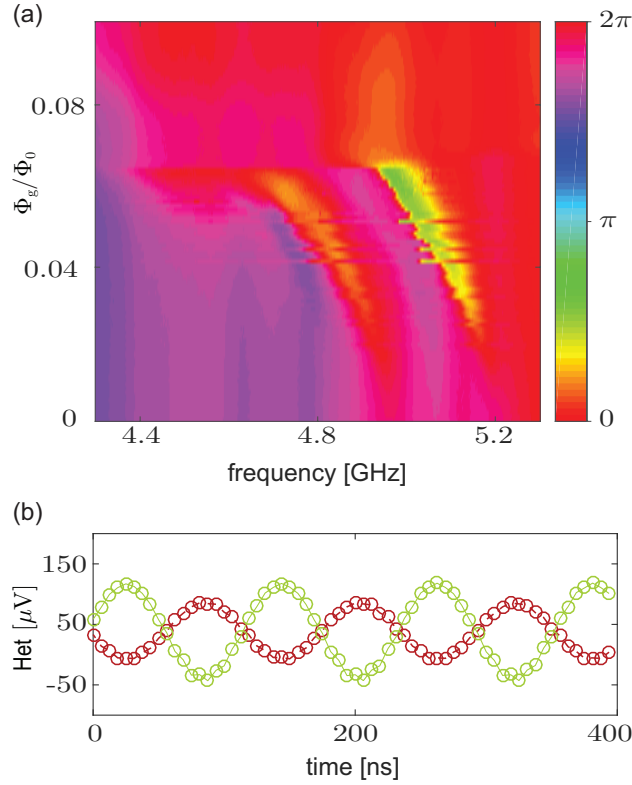


Figure 5.11: Performance of the second-generation circulator (configured as a gyrator). (a) Measurements of $\angle S_{21}$ (color) as a function of frequency and the magnitude of AC gradiometric flux Φ_g . The phase wrap from the two resonant delays is visible around 4.8 and 5.2 GHz, respectively. An “edge” feature is also visible in the data when the gradiometric flux is around $\Phi_g^{\text{edge}} = 0.065\Phi_0$. (b) Heterodyne measurement of forward (red circles, dashed red line) and backward (yellow circles, solid yellow line) transmission through the device. The two signals are π out of phase, as desired for a gyrator. The maxima on the y-axis, however, indicate the received power has been attenuated by 26 dB relative to the input.

may be tuned by increasing the degree to which the bridges are imbalanced), led to a breakdown in the device, visible in the sudden disappearance of the resonant delay and any kind of non-reciprocal transmission (e.g. the “edge” feature in Fig. 5.11a). In dedicated studies of this breakdown, we observe that the location of the edge (in parameter space) depended on Ω and τ , but also on the phase ϕ between the gradiometric flux drives.

Fig. 5.12 illustrates how such an angular dependence could arise, if the edge resulted from the total bias flux (i.e. the interference between the two gradiometric flux lines) through a large

loop in the circuit exceeding some critical value—for example, a value set by the SQUID critical currents, in the manner discussed in Sec. 5.3.3. To see this, note that the flux Φ_{bias} through the large loop in Fig. 5.12a can be expressed with a sum-to-product identity as

$$\begin{aligned}\Phi_{\text{bias}} &= M_A I_g [\cos(\Omega t) - \cos(\Omega t + \phi)] \\ &= -2M_A I_g \sin(\phi/2) \sin(\Omega t + \phi/2).\end{aligned}\tag{5.7}$$

Eq. (5.7) predicts a half-angle scaling of the magnitude of the total bias flux with ϕ . To test that prediction, we perform sweeps like that shown in Fig. 5.11a, with a variety of different phases ϕ and bias frequencies Ω . For each sweep, we record the gradiometric flux Φ_g^{edge} at which the “edge” feature appears.

If, as discussed in Sec. 5.3.3, the edge results from a changing flux through one of these large loops inducing a current that exceeds some threshold value, then a plot of the inverse of Φ_g^{edge} as a function of ϕ should exhibit the same half-angle dependence predicted in Eq. (5.7). Fig. 5.12b shows that this is indeed the case. Each circle is a separate measurement of Φ_g^{edge} , and the different traces correspond to bias frequencies between $2\pi \times 20$ MHz and $2\pi \times 120$ MHz. The solid lines without circles are guides to the eye. They show the expected half-angle dependence $\sin(\phi/2)$ for three different magnitudes, and are included to facilitate comparison with the measured data. This observation supports the conjecture that the edge was caused by induced currents in the microwave circuit which exceeded the critical current of the SQUIDs.

5.4.3 Generation III.

To combat this failure-mode, in the third design cycle we implemented the quadrupole-shielded bias lines discussed in Sec. 5.3.3. We also moved the normal metal inside the bridge circuits, and switched from AuPd to Au, to decrease resistance of the normal metal inserts from 400 mOhm to 10 mOhm. Other than these changes, and the addition of low-pass filters in the bias lines, the overall architecture was largely unchanged from generation two. Fig. 5.13 shows a false-color optical micrograph of the third-generation circulator. Its principal design features and

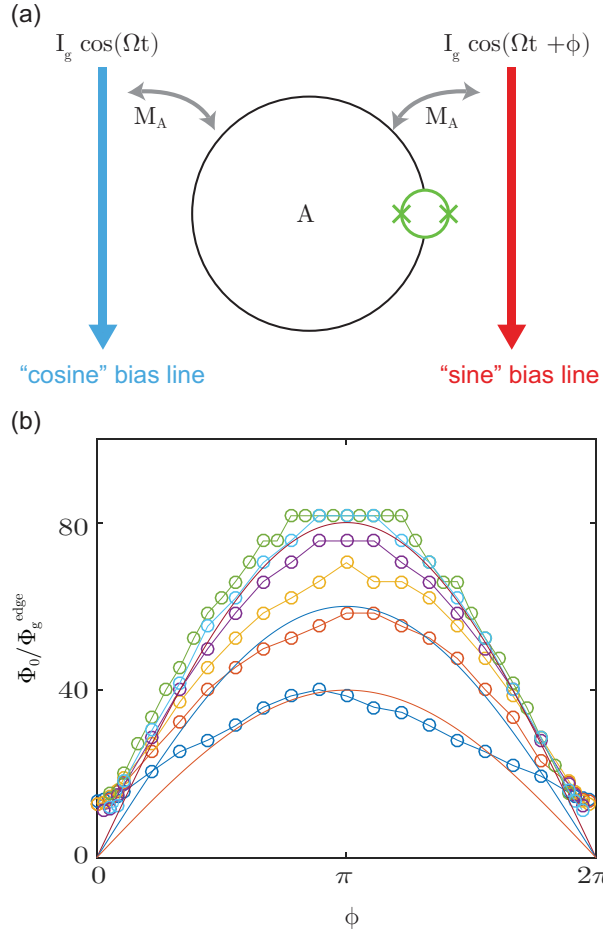


Figure 5.12: Angular dependence of the “edge” feature in the second-generation circulator. (a) Schematic illustrating how flux driven through a large circuit loop (containing a SQUID) by the two bias lines can interfere, to produce a total flux that scales as $\sin(\phi/2)$. (b) Measurements of the “edge” feature (like the one shown in Fig. 5.11), as a function ϕ . Circles are individual measurements of Φ_g^{edge} , and solid lines are theory curves that scale as $\sin(\phi/2)$. The different traces correspond to repeated measurements with different bias frequencies Ω .

observed performance are summarized in Tab. 5.4.

Generation three also improved substantially on its predecessor. When configured as a gyrator, the circuit’s resonant frequencies were visible and stable under active modulation of the gradiometric flux Φ_g (Fig. 5.14a), and the device exhibited the expected non-reciprocal transmission with -4 dB of insertion loss. Heartened by this performance, we also tested the device as a

Table 5.4: Design features and performance of the third-generation circulator.

(New) design features	Observed performance
<ul style="list-style-type: none"> • Used Au instead of AuPd to break supercurrent loops • Moved normal metal inside the bridge circuit, to break all off the circuit's superconducting loops • Implemented the shielded bias lines discussed in Sec. 5.3.3 by running bias currents on the secondary wiring layer (W1) • Inserted simple low-pass filters (20 nH spiral inductors) on the bias lines to reduce the approximately 3 dB of estimated microwave loss through this channel 	<ul style="list-style-type: none"> • Resonant modes tune with static flux, in quantitative agreement with circuit model • Resonant modes tune with dynamic flux modulation; resonant frequencies are stable • Gyration (π phase shift between forward and backward transmission) with -4 dB insertion loss • 13 dB of isolation, 3 dB insertion loss, when operated as an isolator • Linear in microwave power for signals up to -86 dBm

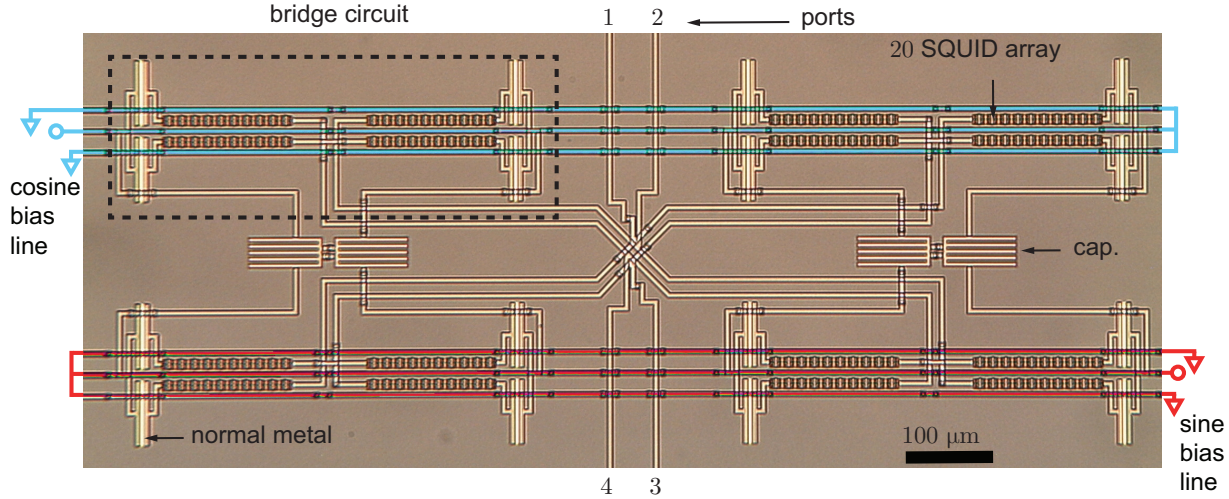


Figure 5.13: False-color optical micrograph of the third-generation circulator layout.

circulator. Fig. 5.14b shows transmission through the device from port 1 to 2 (dashed line) and port 2 to 1 (solid line), as a function of the bias phase ϕ . The approximately 10 dB of contrast between the two traces reveals a violation of Lorentz reciprocity. The device’s dynamical reconfigurability is also evident—operation points for both clockwise and counter-clockwise circulation are visible in the sweeps. At these points, isolation exceeds -13 dB and insertion loss is less than 3 dB.

Nevertheless, the operation point where optimal performance was observed deviated from the expected parameters for ideal operation—though the degree of deviation was far less than in the second generation device. Hypothesizing that the performance breakdown discussed previously was still a limiting factor, we attempted to further reduce the parasitic coupling between the bias lines and larger circuit loops, by reducing the separation between the primary and current returning microstrips of the bias lines from $\epsilon = 23 \mu\text{m}$ to $\epsilon = 17.5 \mu\text{m}$ (reducing the quadrupole moment of the bias line). We also reduced the number of SQUIDs in each array to $N = 12$, to reduce the area of the loops which couple to the bias lines. To maintain the inductance of the arrays at 1 nH, we made a concomitant change in the junction critical current, reducing it from $3 \mu\text{A}$ to $1.92 \mu\text{A}$.

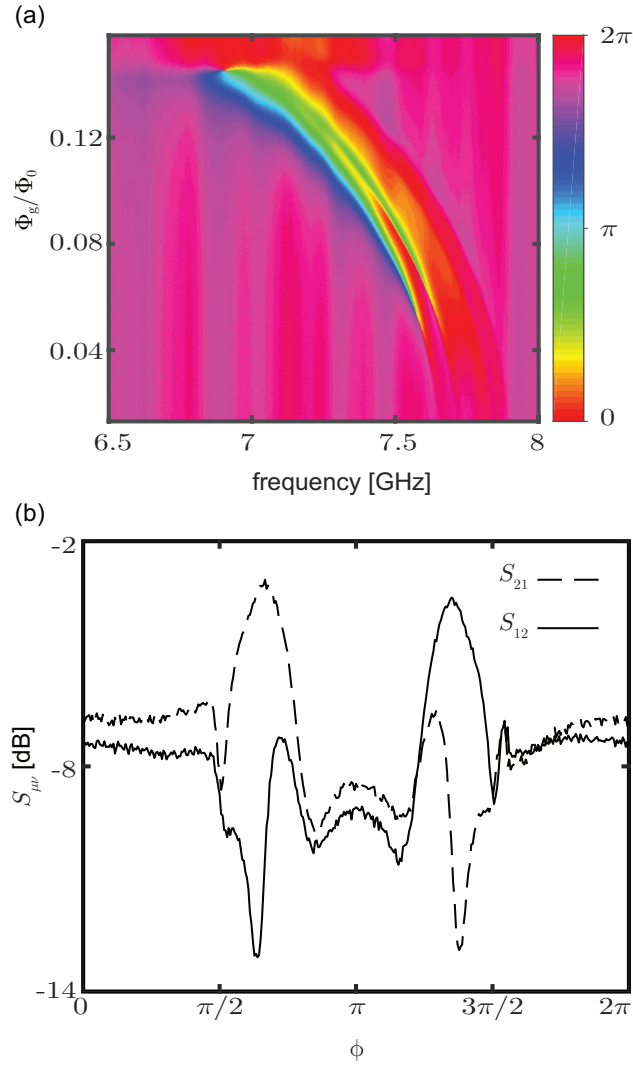


Figure 5.14: Performance of the third generation circulator. (a) The phase of transmission $\angle S_{21}$ as a function of frequency and the magnitude of the AC gradiometric flux Φ_g . Unlike previous generations, the resonant response is completely stable from scan to scan. (b) Transmission as a function of phase ϕ , from the first port to the second port (dashed line) and the second port to the first port (solid line). Two clear operation points are visible, where clockwise and counter-clockwise circulation is realized.

5.4.4 Generation IV.

These changes are reflected in the layout of the fourth-generation device, depicted in Fig. 5.15 alongside the circulator's lumped-element representation. They are also recorded in Tab. 5.5, with

the device's observed performance. As that performance is the subject of the following chapter, we momentarily defer its discussion.

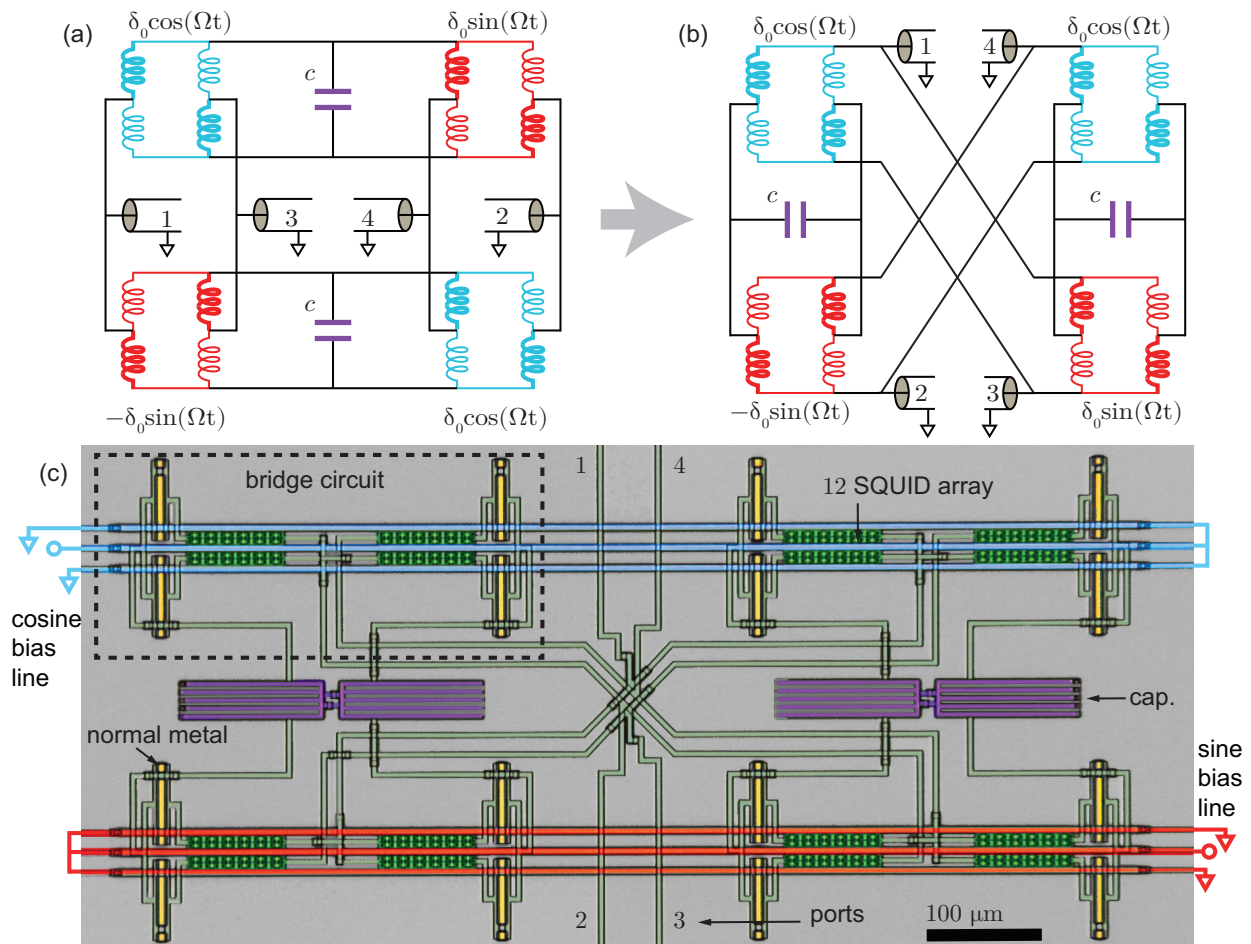


Figure 5.15: Layout of the fourth generation circulator. (a) Lumped-element representation of the circulator. (b) The lumped-element circulator representation in (a), rearranged to better match the device's layout. (c) False-color optical micrograph of the fourth-generation circulator layout.

An additional split was also designed for this wafer, which makes a more radical departure from the layout in generation three. We call this device version b of the fourth-generation circulator. An optical micrograph of a version b chip is shown in Fig. 5.16. Its design features and observed performance are summarized in Tab. 5.6, and are discussed in more detail in the following chapter.

Table 5.5: Design features and performance of the fourth-generation circulator.

(New) design features	Observed performance
<ul style="list-style-type: none"> • Reduced junction critical current from $3 \mu\text{A}$ to $1.92 \mu\text{A}$ and number of SQUIDs in each array from $N = 20$ to $N = 12$, to keep arrays at 1 nH of inductance while reducing circuit footprint • Moved bias lines to tertiary wiring layer (W2) to tighten the quadrupole layout (reduce ϵ, in the language of Sec. 5.3.3) 	<ul style="list-style-type: none"> • Resonant modes tune with static flux, in quantitative agreement with circuit model • Resonant modes tune with dynamic flux modulation; resonant frequencies are stable • $>40 \text{ dB}$ of isolation, less than 1 dB insertion loss, at select frequencies • Tunable operation frequency between 4 and 5.6 GHz • Linear in microwave power for signals up to -90 dBm

Table 5.6: Design features and performance of the fourth-generation circulator, version b.

(New) design features	Observed performance
<ul style="list-style-type: none"> • Interdigitated capacitors • Bias lines split off chip allow for 50% reduction in geometric inductance • Bias line “quadrupole” created without any current division 	<ul style="list-style-type: none"> • Optimal operation phases separated by π • Resonant modes tune with dynamic flux modulation; resonant frequencies are stable • $>40 \text{ dB}$ of isolation, less than 1 dB insertion loss, at select frequencies • Tunable operation frequency between 4 and 5.6 GHz • Linear in microwave power for signals up to -90 dBm

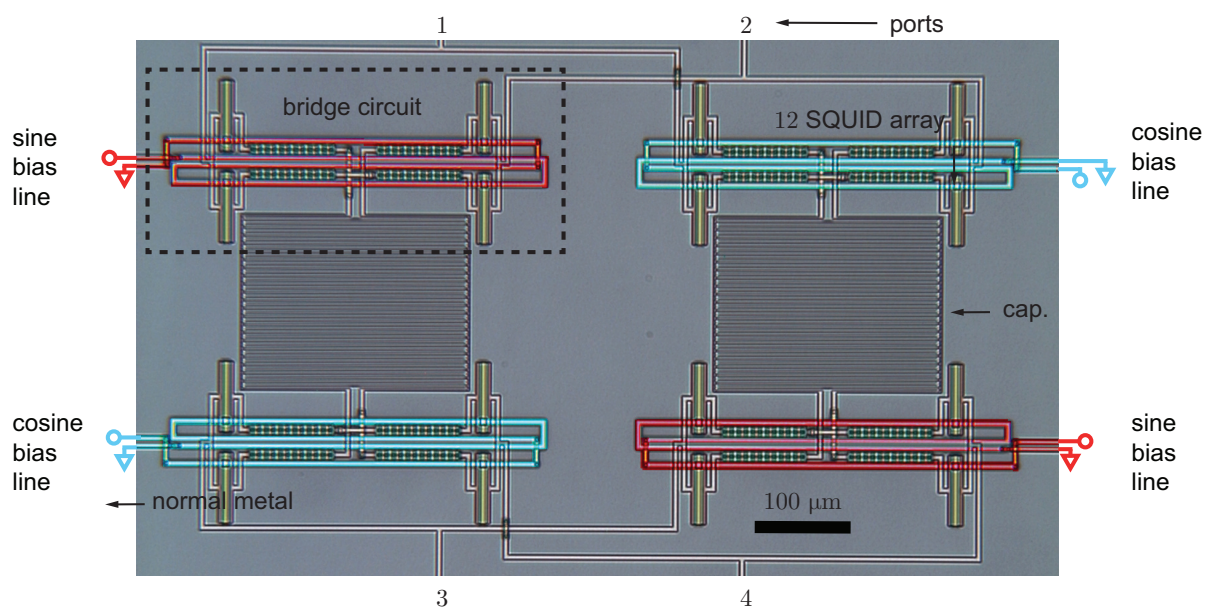


Figure 5.16: False-color optical micrograph of the fourth-generation circulator (version b) layout.

Chapter 6

Experimental results

In this chapter we describe the performance of the fourth-generation circulators. We begin by describing the basic experimental setup. Next the tune-up procedure (that is, the process by which the device's control parameters are set) is discussed. Experimental results follow this, including measurements of the circulator's scattering matrix elements and a characterization of its transmission spectrum and linearity. These measurements are performed over a range of different operation frequencies and with the circulator configured for clockwise and counterclockwise circulation, highlighting the device's tunability and the capability to dynamically reconfigure its sense of circulation *in-situ*. We conclude with a discussion of the measurements, including the device's current limitations, and scaling considerations.

6.1 Experimental setup

To measure the circulator, two of its four ports are terminated in 50 Ohm loads and the circuit is mounted at the base of a ^3He cryostat. A simplified schematic of the experimental setup is shown in Fig. 6.1 (additional details are provided in App. C). Two switches and a directional coupler allow for measurement of the four accessible scattering parameters with a network analyzer.

6.2 Tune-up procedure

Three straightforward steps are required to prepare the circulator for operation. First, the frequency of the resonant delay ω_0 is tuned to the desired operation frequency. Second, the duration

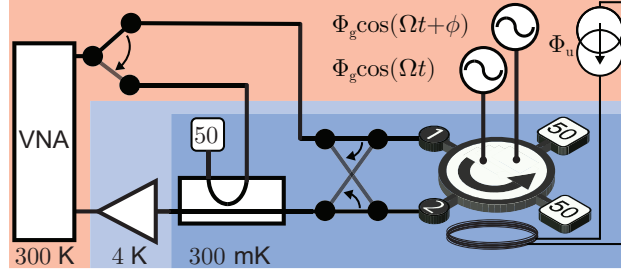


Figure 6.1: Simplified experimental schematic for circulator measurements in a ^3He cryostat (attenuation, filtering, and isolation omitted). Two switches and a directional coupler allow measurement of four of the circulator's scattering parameters.

of the resonant delay τ is set to $\pi/2\Omega$. Finally, the phase difference ϕ between the gradiometric flux control drives is set to $\pm\pi/2$.

We illustrate the first two of these steps in Fig. 6.2, which shows in color the group delay τ acquired during transmission through the device at different probe frequencies ω_p , and for different values of a static gradiometric flux Φ_g applied to all four of the inductive bridges. The measurement is shown for three different values of the uniform flux Φ_u .

Two features are immediately evident in the data. First, the resonant nature of the delay is clear: for fixed values of Φ_u and Φ_g , fields at most probe frequencies are off-resonance and their group delays are less than 5 ns, as visible in the black background of the color plot. Against this background, three arches are visible, which show the resonant delay tuning with Φ_g for the three measurements at distinct Φ_u . The shapes of these arches are qualitatively captured by the theoretical predictions in dashed gray lines, which are made with Eq. (4.7) and the relations that map Φ_g & Φ_u to δ_0 & l_0 in Eq. (4.5) and Eq. (4.6).

Second, when $|\Phi_g|$ approaches 0, the group delay vanishes. A gradiometric bias with magnitude much less than $\Phi_0 = 2\pi\varphi_0$ results in approximately balanced bridges ($\delta \ll 1$). As the external-coupling of the resonant mode depends on δ^2 (Eq. (4.8)), balanced bridges result in under-coupled resonant modes, which strongly attenuates transmission through the resonant differential

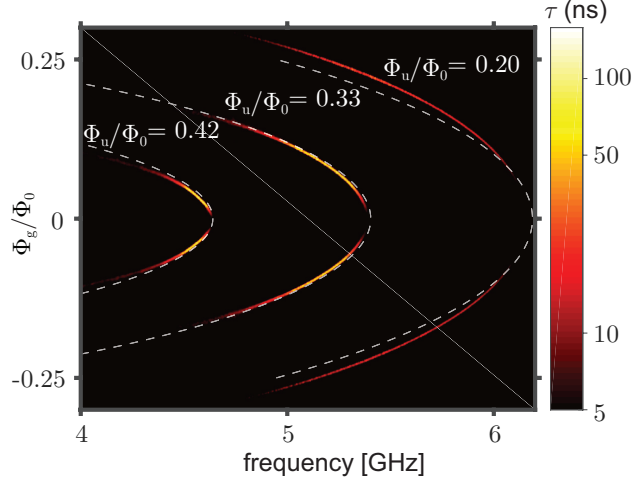


Figure 6.2: Measurements of the circulator’s group delay τ (color, log scale) as a function of the probe frequency and a static gradiometric flux Φ_u applied to all four of the bridge circuits. The duration and center frequency of the resonant delay depend on the uniform and gradiometric flux, allowing the circulator’s operation frequency to be tuned between 4 and 6 GHz. Dashed gray lines are predictions of Eq. (4.7) which use the mapping in Eq. (4.5) and Eq. (4.6). To account for geometric inductance in the circuit (which is not present in the model), the dashed lines are calculated with effective uniform fluxes $\tilde{\Phi}_u/\Phi_0 = 0.38, 0.33,$ and 0.28 , chosen to match the frequency of the measured and predicted delays when $\Phi_g = 0$.

modes. (The internal quality factor of the circuit is estimated to be 400 when the resonant delay is tuned to 5 GHz.) Power is still transmitted through the non-resonant common mode, but without acquiring resonant delay.

As circulation bandwidth scales with the linewidth of the resonant delay, for the measurements in this paper we operate the device with a relatively brief delay on the order of several nanoseconds, with $\Omega = 2\pi \times 120$ MHz. This choice has the additional benefit of reducing the influence of internal losses by keeping the circuit strongly over-coupled.

The final step of the tune-up procedure involves selection of the relative phase ϕ between the gradiometric flux controls. Fig. 6.3 shows a sweep of ϕ when the resonant delay ω_0 is set near $2\pi \times 4$ GHz and the duration of the delay τ is fixed at several ns with $\Omega = 2\pi \times 120$ MHz. The color scale in Fig. 6.3a shows the magnitude of S_{21} as a function of this phase and the probe frequency: S_{12} is shown in Fig. 6.3b. (Calibration of network parameter measurements is discussed in Appendix D.)

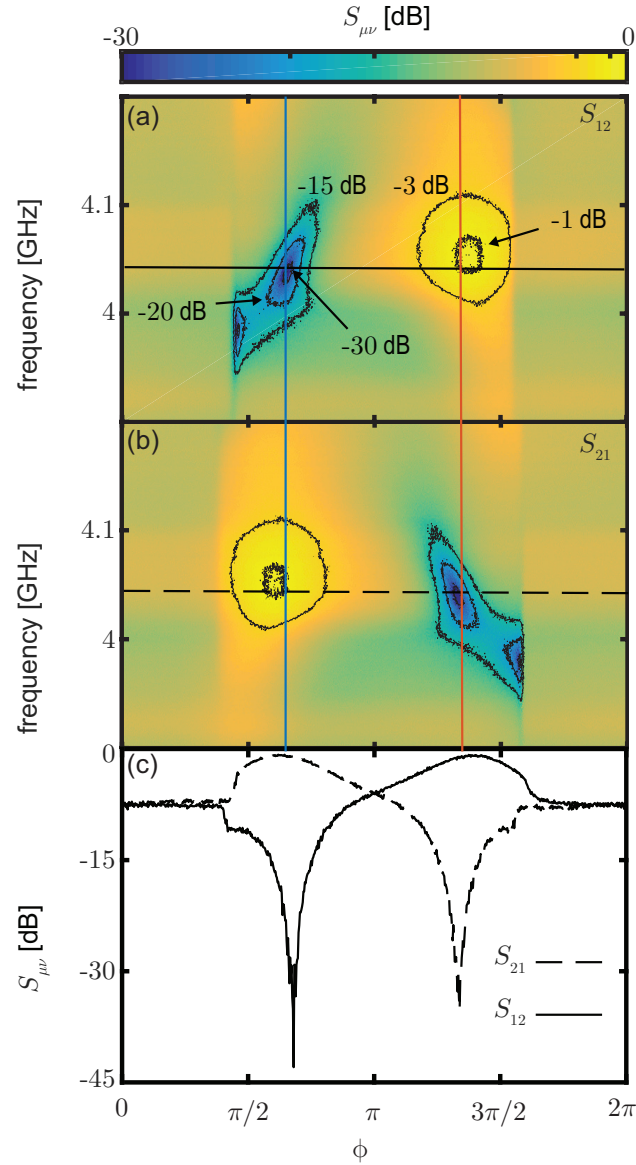


Figure 6.3: Measurements of a dynamically reconfigurable circulator. The phase ϕ between the gradiometric flux lines determines the direction of circulation. (a)-(b) S_{12} and S_{21} a function of the probe frequency and the phase ϕ . Horizontal and vertical lines indicate the location of linecuts plotted in (c) and Fig. 6.4(a). (c) Linecuts of S_{21} (dashed) and S_{12} (solid) at probe frequency $\omega_p = 2\pi \times 4.044$ GHz.

The color plots in Fig. 6.3 reveal two regions of parameter space in which operating points can be chosen. At these phases, the insertion loss is less than 1 dB and the isolation exceeds 30

dB. They can therefore be interpreted as the phases which realize a clockwise or counterclockwise circulator. To illustrate this, Fig. 6.3c shows frequency linecuts at 4.044 GHz from both transmission measurements. Importantly, the linecuts show that high transmission in the counterclockwise (clockwise) direction is accompanied by strong isolation in the clockwise (counterclockwise) direction. They also illustrate how toggling the phase ϕ allows dynamical reconfiguration of the device’s sense of circulation. Interestingly, one can see that the strongest non-reciprocity is observed at phases near but distinct from the expected operating points at $\pi/2$ and $3\pi/2$. Sec. 6.4 describes how geometric inductance in the circuit causes this discrepancy.

6.3 Performance

The frequency-dependence of the non-reciprocity is visible in linecuts of Fig. 6.3a, b, taken at the two optimal operating phases. These linecuts are shown alongside reflection measurements in Fig. 6.4a, and characterize four of the device’s sixteen scattering parameters. Different ports were probed in a separate cooldown, with similar results (presented momentarily).

In the transmission measurements (top right and bottom left plots), high transmission (> -1 dB) and robust isolation (> 20 dB) are observed in a 50 MHz window around 4.044 GHz. These features are approximately coincident with -11 dB dips in the reflection measurements (top left and bottom right plots). Together, power collected in the transmission and reflection measurements account for 90% of the injected signal power.

To determine if the remaining power is dissipated or scattered to other frequencies, a spectrum analyzer is used to measure the transmission of the circulator at frequencies $\omega_p \pm m\Omega$ which are detuned from the input frequency by integer multiples of the modulation rate Ω . Fig. 6.4b shows the power of these spectral components, relative to the transmitted spectral component at ω_p . The device suppresses spurious sidebands by more than 20 dB. The spectral purity of the output—in particular, the suppression of spectral components at $\omega_p \pm 2\Omega$ —is a testament to the high-degree of symmetry in the circuit. From this measurement, we conclude that the remaining 10% of input power is dissipated into heat or other radiation modes.

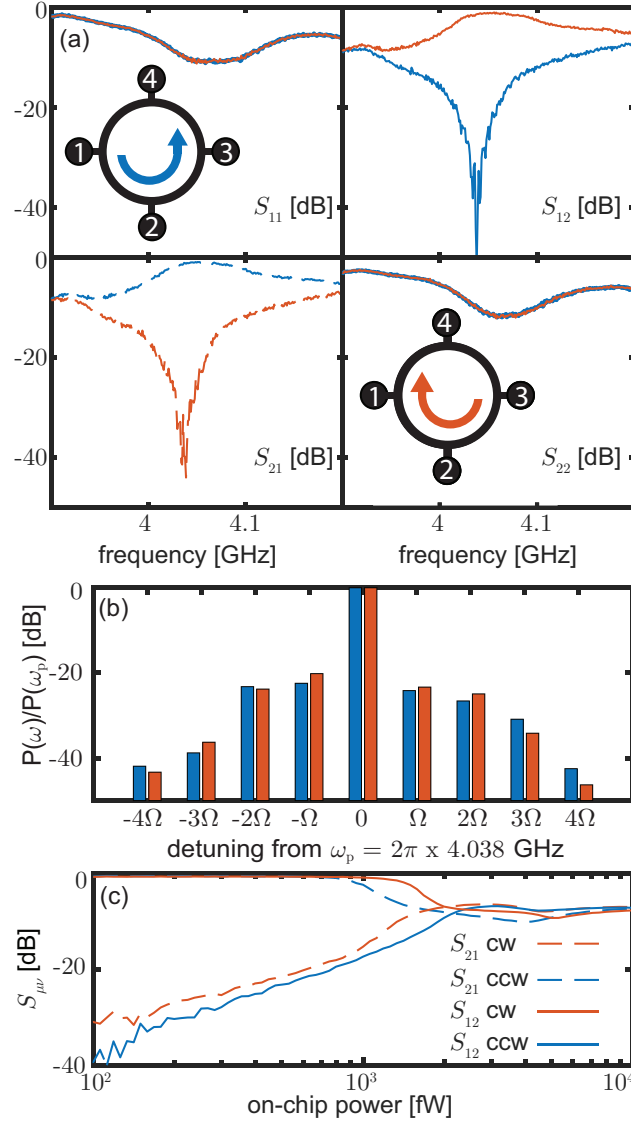


Figure 6.4: Performance of an on-chip superconducting circulator tuned to operate near 4 GHz. (a) Frequency dependence of four of the circulator’s 16 scattering parameters, when configured as a counterclockwise circulator (blue traces) and a clockwise circulator (orange traces). (b) Transmission spectrum of the circulator at $\omega_p = 2\pi \times 4.044$ GHz, measured at frequencies $\omega_p \pm m\Omega$ with m a positive integer. Spectral components are normalized by the power transmitted at ω_p . Spurious sidebands are suppressed by approximately 20 dB. (c) Transmission as a function of probe power, with probe frequency fixed at $\omega_p = 2\pi \times 4.044$ GHz. 1 dB compression occurs around 1 pW.

Finally, Fig. 6.4c displays the dependence of clockwise and counterclockwise transmission on the power of the probe signal. Fixing the probe frequency at $\omega_p = 2\pi \times 4.044$ GHz, the measurement

is repeated for both clockwise and counterclockwise operation. In both cases, 1 dB compression of the transmitted signal occurs at input powers around 1 pW. As the input power approaches this value, we also observe a degradation in the circulator’s isolation, which drops below 20 dB at a power again roughly equal to 1 pW. In analogy with the 1 dB compression point, we refer to this power as the 20 dB expansion point of the circulator. Expressed in terms of photon number, this linearity allows the circulator to process over 10^3 photons per inverse of its bandwidth.

For reference, the typical power in a microwave tone used for dispersive readout [59] of a superconducting qubit is between 100 and 1000 aW (few photon level) [150]. The three orders of magnitude that separate this power scale from the 1 dB compression and 20 dB expansion points of the device are critical for one attractive application of a monolithic superconducting circulator: on-chip integration with a quantum-limited reflection amplifier, such as a Josephson parametric amplifier. The high power handling of the circulator allows it to route qubit readout tones even after they reflect off a Josephson parametric amplifier and are amplified by 20 dB.

To demonstrate the circulator’s tunability, we operate the device at a variety of frequencies between 4 and 6 GHz and repeat the measurements shown in Fig. 6.4. Fig. 6.5 summarizes the performance of the device across this band. Insertion loss is shown in Fig. 6.5a. Transmission is greatest at the lowest frequency, and decreases with frequency until it approaches -3 dB. We attribute this trend to the geometric inductance present in the circuit, which limits the degree to which the bridges can be imbalanced. This inhibits impedance matching and reduces the degree to which the resonant differential modes are over-coupled. At lower operation frequencies, the Josephson inductance comprises a greater fraction of the bridge’s total inductance, mitigating this effect.

This interpretation is supported by the power dissipation that we estimate at each operation frequency (Fig. 6.5b), computed as the sum of the reflection R and transmission T coefficients $-10 \log_{10} (R^2 + T^2)$. (Power transmitted to sidebands of the modulation frequency is suppressed by over 20 dB, and is therefore neglected in this accounting). Reflections, visible in the discrepancy between insertion loss and transmission, are larger at higher frequencies, where the role of geometric

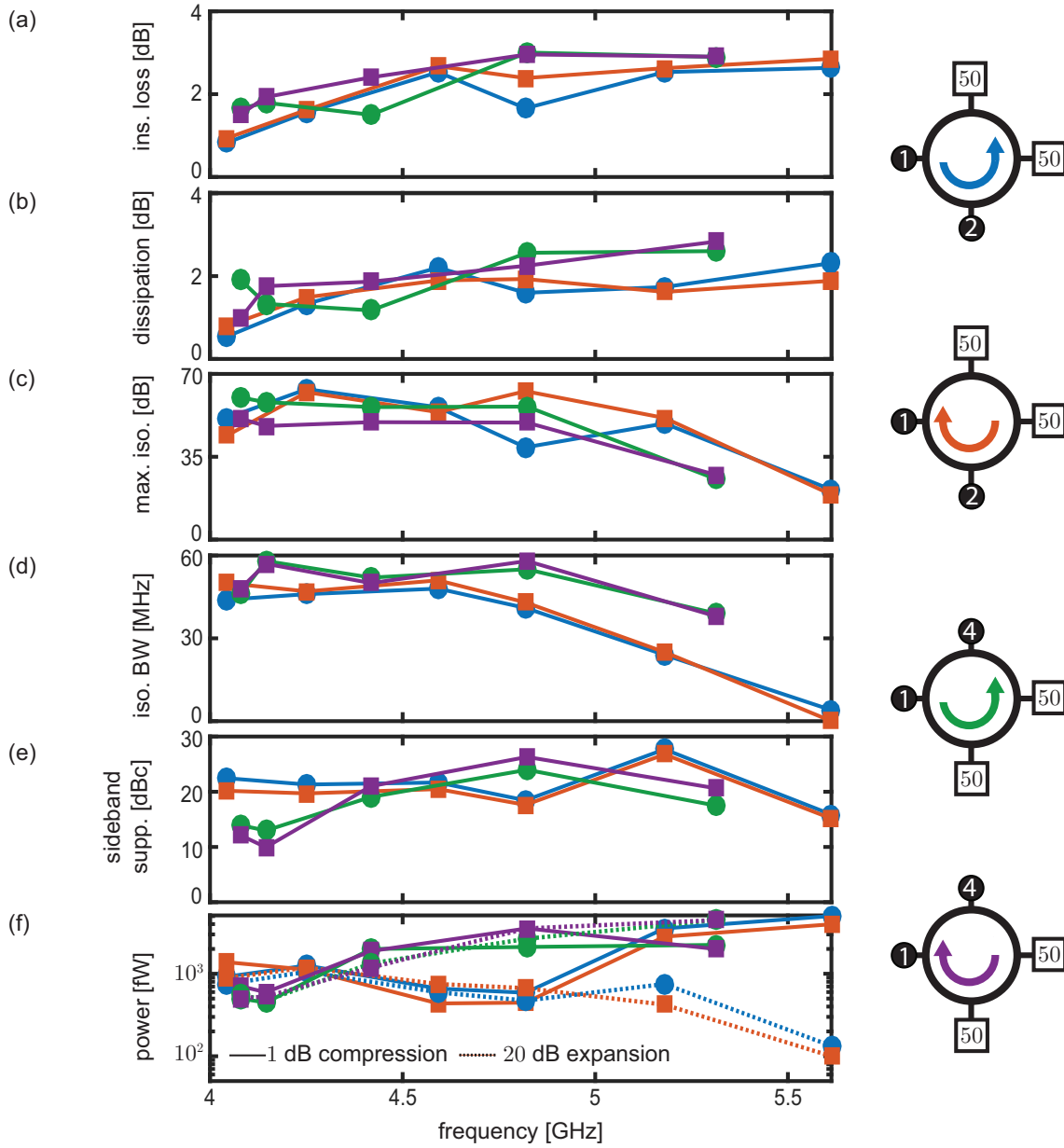


Figure 6.5: Performance of a widely tunable on-chip circulator. The minimum insertion loss (a), dissipation (b), maximum isolation (c), isolation bandwidth (d), sideband suppression (e), and power handling (f) are plotted at frequencies between 4 and 6 GHz, for clockwise (orange and purple rectangles) and counterclockwise (blue and green circles) operation. Isolation bandwidth refers to the bandwidth over which isolation exceeds 20 dB. Sideband suppression refers to the contrast between transmitted spectral components at the input frequency ω_p and the largest spurious sideband of the form $\omega_p \pm n\Omega$. In (e), dotted (solid) lines indicate the device's 1 dB compression (20 dB expansion) point.

inductance is more pronounced. Dissipation is also greater at higher operation frequencies, where the external coupling of the resonant mode is lower. We believe the dominant source of dissipation in the circuit is the dielectric loss of SiO_2 .

The circulator’s maximum isolation is plotted in Fig. 6.5c. Below 5.5 GHz, isolation exceeds 35 dB for both device configurations. Critically, isolation is achieved over a bandwidth of several tens of MHz, much greater than the bandwidths typical for strongly-coupled cavity ports in dispersive qubit readout, which range up to several MHz [46, 47, 151]. Fig. 6.5d shows the frequency interval over which the isolation exceeds 20 dB.

It should be noted this isolation is achieved concurrent with the performance shown in the rest of Fig. 6.5: all specifications are measured at two fixed operation phases, which realize clockwise and counterclockwise circulation. To select these operation phases in a quantitative manner, we write a cost function to simultaneously balance the benefits of low insertion loss, high isolation, and broad bandwidth, for both clockwise and counterclockwise operation. Ultimately, different applications will prioritize the relative importance of these specifications in different ways, allowing trade-offs in performance specifications, for example, between insertion loss and isolation. Similarly, if the device’s reconfigurability is not needed, performance will generally exceed that shown in Fig. 6.5.

Fig. 6.5e characterizes the spectral purity of transmitted fields at each operation frequency. It shows the size of the largest spurious sideband, (relative to the power transmitted at the probe frequency), which we call the sideband suppression. Harmonics of the modulation frequency Ω are strongly suppressed across the operation band, typically by about 20 dB.

Lastly, Fig. 6.5f shows how the power-handling of the circulator depends on the operation frequency. Frequencies between 4 and 5 GHz have 1 dB compression points and 20 dB expansion points around 1 pW, roughly three orders of magnitude above the power level used for dispersive readout of a superconducting qubit.

6.4 Discussion

Applications and perspectives for an on-chip superconducting circulator are discussed in the final chapter of this thesis. Here we comment on issues currently limiting device performance, and on the attenuation and filtering considerations relevant to scalability.

6.4.1 Device limitations and deviation from theoretical models

In this section we discuss non-idealities observed in the circulator, in which the network parameter measurements depart from the theoretical predictions of the scattering matrix, obtained with the analytical model in Ref. [115]. The reference predicts the dependence of \mathbf{S} on the parameters l_0 , δ , and Ω . Using the relations in Eq. (4.5) and Eq. (4.6), l_0 and δ can be mapped to the flux controls Φ_u and Φ_g . To facilitate this comparison, Fig. 6.6 shows measured and predicted transmission parameters, as a function of the probe frequency and the gradiometric flux Φ_g .

Qualitatively, the experiment and model agree fairly well: all four plots show a pair of resonant modes split by twice the modulation rate $\Omega/2\pi$, in analogy with a Sagnac interferometer [128]. As Φ_g increases, these modes shift down in frequency and broaden. Furthermore, the device's non-reciprocity is evident in both the model and in experiments: at the lower frequency mode, S_{21} is large in magnitude at the same frequency and gradiometric flux that S_{12} is small.

One can also see aspects of the experimental data which are not captured in the model. For example, as Φ_g approaches 0 the resonant modes become increasingly difficult to perceive in the experimental data. In the model, though, the modes become narrower as Φ_g decreases, but remain well distinguished from the off-resonant transmission. This discrepancy is a result of the fact that internal losses are not included in the theoretical model. In the measurement, the presence of loss means that for small enough Φ_g , the modes become under-coupled and are difficult to detect.

Another discrepancy is the slight splitting ($2g \approx 2 \times 2\pi \times 17$ MHz) of each resonant mode, visible in the experimental plots (Fig. 6.6a and b). We attribute this splitting to a hybridization of the circuit's two degenerate resonant modes, which is not included in the model.

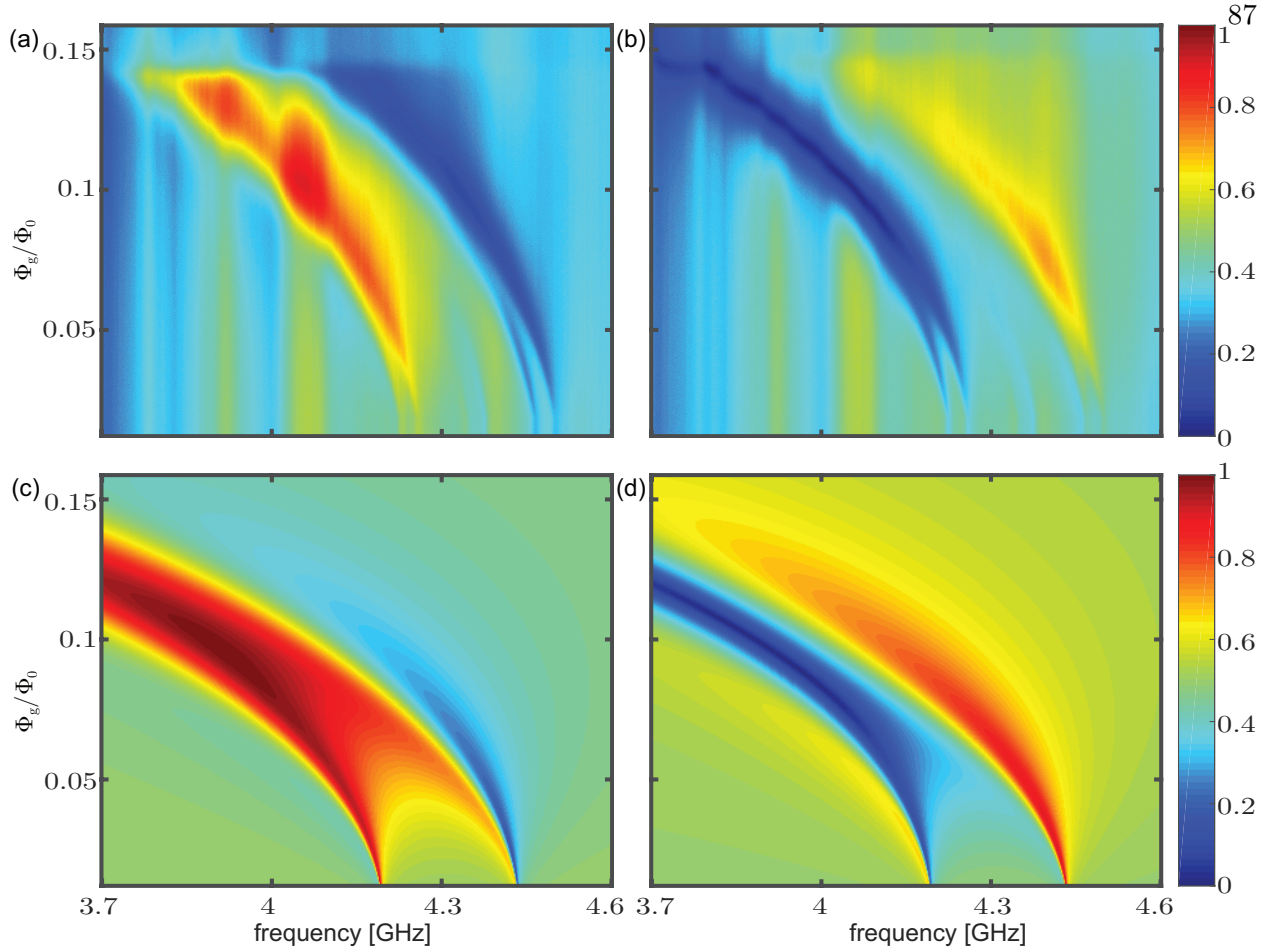


Figure 6.6: Measurements (a,b) and theoretical predictions (c,d) of $|S_{21}|$ and $|S_{12}|$, as a function of probe frequency and amplitude of the oscillatory gradiometric flux, when the device is configured as a counterclockwise circulator. Theoretical predictions are made with the expressions in Ref. [115] and the mapping in Eq. (4.5) and Eq. (4.6). Circuit parameters are fixed at their design targets ($l_0 = 1$ nH, $c = 1$ pF) and the flux controls are set to match the measurements in (a) and (b): $\Omega = 2\pi \times 120$ MHz, $\Phi_u = 0.38\Phi_0$.

The sharp “edge” visible at large $\Phi_g/\Phi_0 \approx 0.15$ in the measurements is an additional difference between the model and experiments. As discussed in Ch. 5, this edge feature is likely caused by induced currents in the microwave circuit which exceed the critical current of the SQUIDS. Refinements in the layout can reduce these induced currents, though device operation would still be limited in the amplitude of the applied gradiometric flux; the application of a total external flux $\Phi_u \pm \Phi_g$ with magnitude greater than $\Phi_0/2$ causes a deviation from the simple flux tuning described

in Fig. 4.2. When the total flux exceeds this threshold, further increase in Φ_g serves to **balance** the inductive bridges, rather than imbalance them, and a departure from the model is expected in this regime.

A final difference between the model and experiments is visible in the scaling of the resonant modes with the gradiometric flux. The modes in the theory plots are more sensitive to Φ_g , bending down to lower frequencies than the measured modes. They also broaden and merge, to a degree which is not apparent in the measurements. We attribute this discrepancy to geometric inductance in the circuit which reduces the tunability of the resonant delay and restricts the modal linewidth.

This interpretation is supported by our observation of optimal circulator performance at drive phases ϕ distinct from the theoretically expected values at $\pi/2$ and $3\pi/2$. When geometric inductance restricts the linewidths of the circulator's resonant modes, it prevents the creation of the brief (2 ns) resonant delay needed to satisfy the convert-delay operation condition: $\Omega\tau = \pi/2$. The condition can be met with reduction of Ω , but this is undesirable for two reasons: first, the circulator's bandwidth is proportional to Ω ; second, device performance requires that the modulation rate Ω exceed the internal splitting g of the hybridized resonant modes: $\Omega \gg g$.

A simple extension of the theory discussed in Sec. 4.1 shows how the circulator's transmission depends on ϕ and $\Omega\tau$ in the general case when $\Omega\tau$ takes values other than $\pi/2$:

$$\begin{aligned} S_{21} &\propto \frac{1}{2}(1 - \cos(\Omega\tau + \phi)) \\ S_{12} &\propto \frac{1}{2}(1 - \cos(\Omega\tau - \phi)). \end{aligned} \tag{6.1}$$

From these expressions, it is clear that if $\Omega\tau$ is forced to take values greater than $\pi/2$, improved counterclockwise (clockwise) circulation can be obtained with phases greater (less) than $\pi/2$ ($3\pi/2$). Our observation of optimal control phases at $\approx 2\pi/3$ and $4\pi/3$ corresponds to a minimum achievable delay of about 3 ns.

6.4.2 Comparison with the fourth-generation, version b device

The performance of the fourth generation version b chip is also consistent with this argument. In that device, geometric inductance was reduced by approximately 50% (see Fig. 5.16 for an optical micrograph) by dividing the sine and cosine bias lines off-chip, allowing the bridge circuits to be imbalanced to a greater degree.

Fig. 6.7 shows its scattering matrix when the device was configured as an isolator. Over 40 dB of contrast may be observed between the forward transmission and reverse isolation at the center of the device's bandwidth. Importantly, the difference between the optimal clockwise and counterclockwise operation phases for this device is $0.9972\pi \approx \pi$. In sum, we expect shorter delays to be possible with this device, and observe no deviation in the operation phases from theoretical expectations.

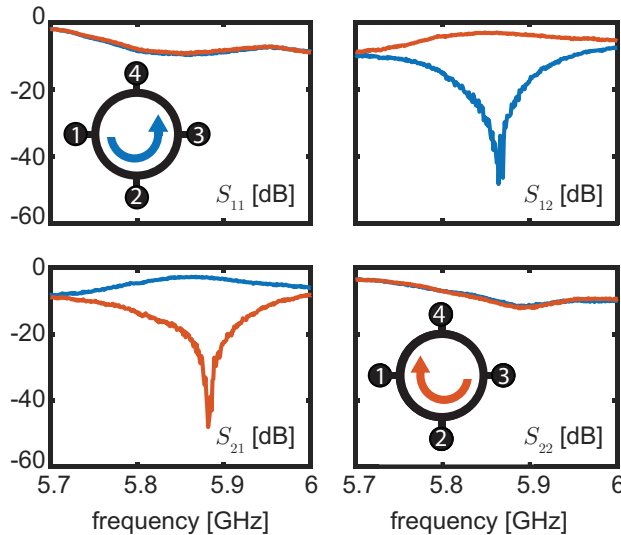


Figure 6.7: Scattering parameters of the fourth-generation circulator, version b, tuned to operate near 5.9 GHz. Frequency dependence of four of the circulator's 16 scattering parameters, when configured as a counterclockwise circulator (blue traces) and a clockwise circulator (orange traces).

Fig. 6.8 shows the performance of this circulator over a wide operation band, between 4 and 7 GHz. Insertion loss and dissipation are plotted in Fig. 6.8a, the maximum isolation is plotted in Fig. 6.8b, and the bandwidth over which isolation exceeds 20 dB is plotted in Fig. 6.8c.

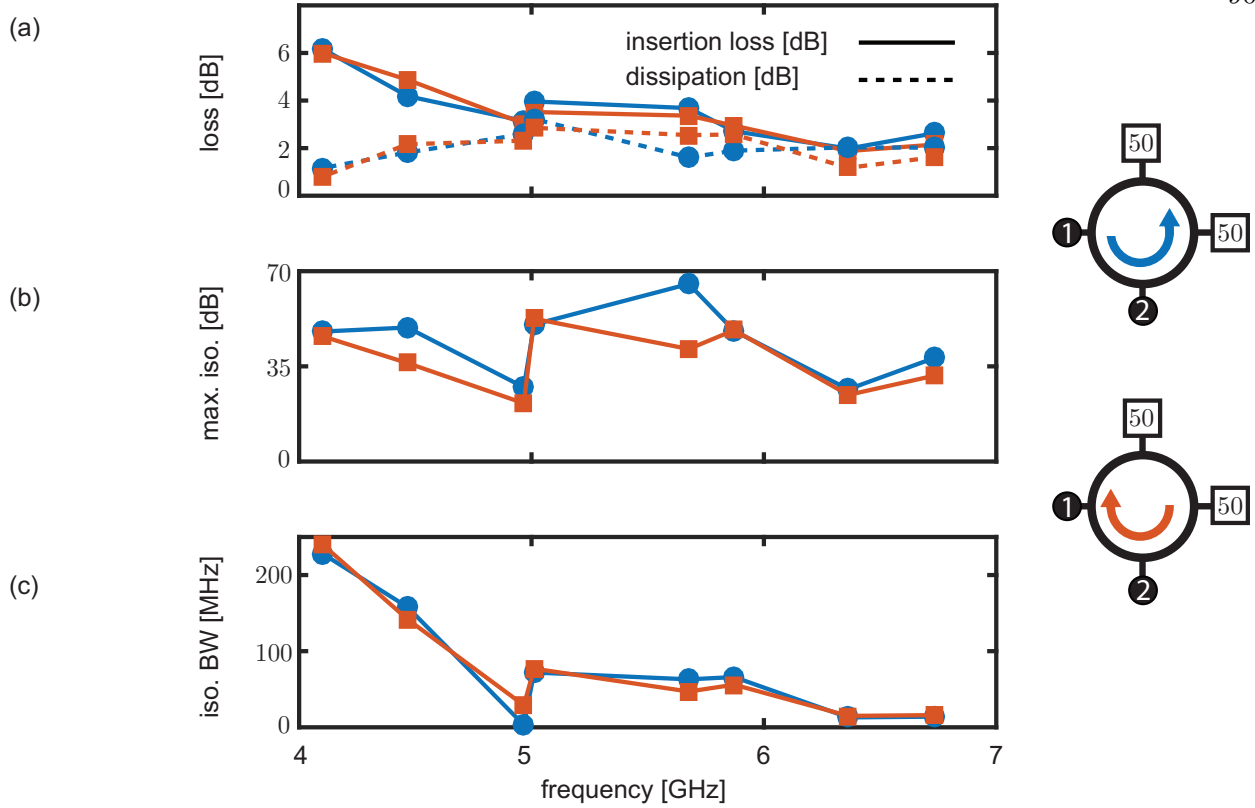


Figure 6.8: Performance of the fourth-generation circulator, version b. Insertion loss (a, solid lines) and dissipation (a, dashed lines), maximum isolation (b), and isolation bandwidth (c), as a function of operation frequency. Isolation bandwidth is defined as the frequency interval over which the isolation exceeds 20 dB.

In many ways, its performance is comparable to the other generation-four design (discussed in Sec. 6.3). The predominant difference is a slight increase in the reflection coefficient of the version b device, which results in greater insertion loss. (Version b exhibits insertion losses between 2 and 6 dB, compared to 0.8 to 3 dB insertion losses in the other device).

The discrepancy is especially apparent at low operation frequencies. One explanation for this observation is the difference in capacitance values for the two designs (0.96 pF in the first device and 0.6 pF in the version b design). The smaller capacitance in the version b device allows it to operate up to 7 GHz, and necessitates the application of a large uniform flux to shift the circuit's resonant frequency down to 4 GHz. At this frequency, the SQUID arrays have a reactance of about 100 Ohms, which leads to a total breakdown of the expansion in Ch. 4 in the parameter $\omega l/Z_0$.

In other words, as the two devices have different maximum operation frequencies, a comparison at 4 GHz may not be a direct comparison: the device with the greater operation frequency must be tuned to a greater degree to reach 4 GHz, which can cause a breakdown of a needed high- Q approximation. Nevertheless, even near its maximum operation frequency the version b device is not as well matched to 50 Ohms.

One surprising similarity in the performance of the two devices is that their measured dissipation is quite similar. Measurements with test resonators (SQUID array bridge circuits shunted by parallel-plate capacitors) indicate an internal Q between 300 and 400, which was assumed to be limited by dielectric loss in the silicon oxide. Given the external coupling rate of the circulator's resonant modes, this would lead to approximately 0.5 dB of insertion loss. Unexpectedly, the version b device (which uses interdigitated capacitors) shows no reduction in dissipation. A detailed explanation for the insertion loss in the two devices remains an open question.

6.4.3 Filtering, attenuation, and power-consumption considerations, in the context of scaling

One of the costs associated with replacing passive ferrite circulators with active on-chip circulators is the power consumption of the control tones, and the heat loads this creates in a dilution refrigerator. Estimating that power consumption requires a discussion of the attenuation and filtering of the control lines.

To determine the attenuation required to keep the added noise below half a photon, the added noise is estimated as a function of the temperature T to which the control lines are thermalized. Scaling and filtering considerations are then discussed, in light of this result.

For simplicity, consider the noise added by the circulator during transmission from its first port to its second port. Fluctuations of the bias current amplitude and relative phase between the two bias signals will modulate a transmitted tone, thus creating noisy modulation sidebands of the tone. The sideband noise powers caused by amplitude fluctuations S_I^{AN} and phase fluctuations S_I^{PN}

are (at most)

$$\begin{aligned} S_I^{\text{AN}} &= \left(\frac{\partial S_{21}}{\partial I_g} I_{1\text{dB}} \right)^2 S_I, \\ S_I^{\text{PN}} &= \left(\frac{\partial S_{21}}{\partial \phi} \frac{I_{1\text{dB}}}{I_g} \right)^2 S_I. \end{aligned} \quad (6.2)$$

Here, $I_{1\text{dB}}$ is the signal current in the device at its 1 dB compression point and $S_I = 4k_B T/Z_0$ is the current spectral density of the Johnson noise (in the bias lines) at a temperature T [152, 14]. We say the sideband noise powers are bounded above by the relations in Eq. (6.2) because these noise powers are multiplicative, and it is reasonable to assume the microwave signal power incident on the device (during normal operation) is at most $I_{1\text{dB}}$.

Because we operate near a maximum in $|S_{21}|$, the dominant effect of noise in both the amplitude and phase of the bias currents is the phase modulation of the transmitted tone; i.e., both S_I^{AN} and S_I^{PN} are predominantly phase noise in the transmitted tone.

The partial derivatives in Eq. (6.2) can be calculated directly from measurements of the scattering parameters, made as a function of the bias current amplitude I_g and the phase between the bias lines ϕ (shown, for example, in Fig. 6.6 and Fig. 6.3). After these numerical derivatives are calculated, the sideband noise powers may be divided by $2\hbar\omega_p/Z_0$ to convert them to photon numbers. In our measurements, where the bias lines are thermalized to $T \approx 300$ K, this results in $n = 14$ photons of added noise, with S_I^{AN} accounting for 95% of the noise.

Positioning 40 dB of attenuation at room temperature and 20 dB at the four Kelvin stage of a dilution refrigerator would result in a noise temperature of $T \approx 7$ K, or in units of photons, $n = 0.3$. This level of attenuation is reasonable for modern dilution refrigerators, as the circulator operates with gradiometric currents I_g on the scale of 100 μA : the heat load caused by a 20 dB attenuator at the four-K stage is 50 μW , which is much less than the Watt-scale cooling power available at that stage.

With superconducting twisted-pairs to carry the bias currents from the four-K stage to the mixing chamber plate, and a contact resistance of 10 mOhm at the chip interface, the heat load on the mixing chamber plate is 100 pW. This load is also much less than the roughly 50 μW of

available cooling power on a 50 mK mixing chamber plate. These considerations are summarized in Tab. (6.1), which presents a power budget for an active circulator with control lines thermalized as described above.

Table 6.1: Power budget for an active circulator with control lines thermalized to $T \approx 7$ K as described in the text. In this configuration, the circulator adds 0.3 photons of noise. A contact resistance of 10 mOhm is assumed at the chip interface. Cited cooling powers are for an Oxford cryogen-free dilution refrigerator, and are approximate.

T [K]	I_g [A]	heat load [W]	cooling power [W]
300	10^{-1}	5×10^{-1}	n/a
4	10^{-3}	5×10^{-5}	7.5×10^{-1}
0.05	10^{-4}	10^{-10}	5×10^{-5}

This analysis indicates the feasibility of operating 10^3 on-chip circulators in a single dilution refrigerator, each with less than half a photon of added noise. We emphasize that this is one of many possible design choices and it is possible to reduce the added noise and dissipated power in several different ways. For example, the bias lines could be filtered to reject the noise below 50 MHz, which adds noise in the circulator's band, while still passing 100 MHz bias tones.

Chapter 7

Conclusion and Outlook

In this thesis we realize the on-chip superconducting circulator proposed in Ref. [115]. Lorentz reciprocity is broken in the circuit with sequential translations in frequency and time, which we show with a standard circuit analysis and with a simple model system composed of just two components: multiplying elements and delays. We describe how both of these elements can be created in a cryogenic microwave environment, and then characterize the performance of a circulator built from these components. We observe low insertion loss and over 20 dB of isolation over a bandwidth of approximately 50 MHz. The device is linear with respect to input power for fields up to 1 pW in power, and its transmission spectrum is spectrally pure, in the sense that spurious harmonics created by the device's RF control tones are suppressed by more than 20 dB. Finally, we demonstrate that all of these performance specifications can be achieved over a frequency range in excess of 1 GHz, and in clockwise or counterclockwise configurations. This ability to dynamically reconfigure the sense of circulation is a feature unavailable in commercial ferrite circulators which are typically constructed with permanent magnets, and enables new possibilities for the connectivity of advanced networks.

As the device requires no microwave frequency control tones, and as it is orders of magnitude more compact than commercial ferrite circulators, this superconducting circulator is a scalable alternative to signal routing with ferrite junction circulators. We estimate that with superconducting twisted pairs carrying the low-frequency control tones, 10^3 of these circulators could be operated in a single dilution refrigerator.

From a technological perspective, the superconducting circulator constructed for this thesis represents a new level of complexity for analog integrated circuits in the niobium trilayer process. It also provides a demonstration of a general-purpose prescription for circulation [115], which need not be implemented with superconducting materials. For example, in room temperature applications where tunable capacitors are a widely available component, the dual of this circuit can be used to realize a scalable, on-chip circulator. Transmission and reception of signals in the antennas of cellular phones and cellular base stations is currently multiplexed in frequency, due to the need for high channel isolation and the dearth of compact, integrated, non-reciprocal components at microwave frequencies. Duplexing with a circulator would obviate the need for this multiplexing, doubling the effective bandwidth of the antenna. Such an adaptation of the circulator technology could be lucrative, as 5G telecommunication technologies are likely to gain mass-market coverage by 2020, with a projected \$250 billion USD market size [153].

Looking forward, the work suggests several immediate extensions. In a future design, layout changes could improve device performance: dielectric loss can be reduced with the use of low-loss dielectrics like amorphous silicon [100], or with interdigitated capacitors. Similarly, dividing the power in the gradiometric flux lines off-chip and delivering the control tones with four dedicated on-chip bias lines removes layout constraints, and enables the design of a circuit with approximately half the geometric inductance.

Even with the device's existing performance, another obvious extension is on-chip integration of the circulator with a quantum-limited amplifier. This further miniaturizes the amplification chain, and removes unwanted sources of loss from normal-metal connections between the superconducting reflection amplifier and circulator.

Finally, the essential concept of frequency conversion and delay can be adapted to a lossless and broadband design, using non-resonant delays, as suggested in Ref. [116]. Fig. 7.1a illustrates one possible design for such a broadband, lossless circuit. The device uses the same bridge-circuit multipliers as the circulator discussed in the previous chapter, but requires only two of the bridges. The element Z_m is an impedance included to impedance match the bridge circuits, needed because

of the finite-tunability of the SQUID-array inductors. As the Bode-Fano criterion [154, 155] is relatively lenient for low quality-factor circuits, we estimate that appropriate choice of Z_m would allow reflections to be limited to less than -20 dB over a bandwidth of 8 GHz (see supplementary information in Ref. [132]).

The delays, rather than realized with a resonant mode, are transmission lines connecting the two bridges. A final difference is that the bias signals are square wave, rather than sinusoidal. Biased in this way, the impedance-matched bridge circuits function as cross-over switches.

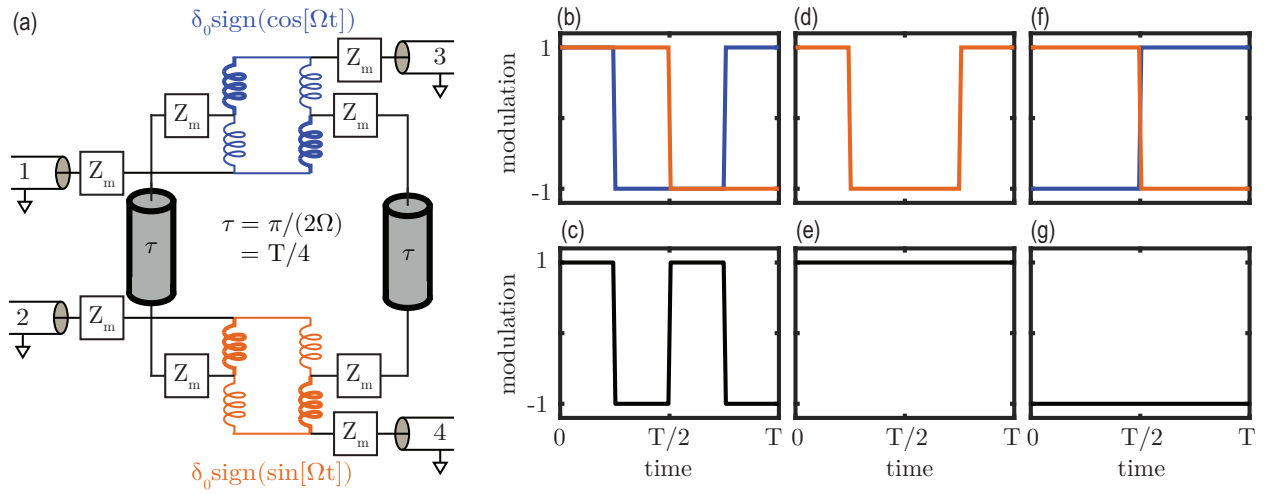


Figure 7.1: Lossless, broadband circulation. (a) Schematic for a lossless, broadband, and superconducting circulator, inspired by ideas in Refs. [116, 156, 120]. Circulation arises from interference between the reciprocal even-mode and the gyrating odd-mode of the circuit. (b)-(g) Describe how non-reciprocity arises in the odd-mode. (b) Modulation profiles of the two square-wave biased bridge circuits when the delay separating the bridges is $\tau = 0$. (c) Product of the modulation profiles in (b). Transmission is reciprocal, and power is scattered into modulation sidebands. (d) Modulation profile for a signal exciting the differential mode of the upper port (odd excitation of ports 1 & 3) when the delay separating the bridges is a quarter of the modulation period, $\tau = T/4$. (Graphically, this shifts the orange trace back by a quarter-period.) (e) The product of the modulation profiles in (d). As the product is 1 for the entire modulation period, the signal is effectively unmodulated. (f) Modulation profile for a signal exciting the differential mode of the lower port (odd excitation of ports 2 & 4) when the delay separating the bridges is a quarter of the modulation period, $\tau = T/4$. (Graphically, this shifts the blue trace back by a quarter-period.) (e) The product of the modulation profiles in (d). The product is constant in time, as in (e), but the minus sign imparts a π phase shift on the incident signal. The odd-mode of the circuit therefore realizes a gyrator.

As in the analysis of Ch. 4, the circuit’s operation is greatly simplified by transforming to a basis of even and odd excitations of the top (ports 1 & 3) and bottom (ports 2 & 4) ports. Viewed in that light, circulation again arises from a “virtual” Hogan construction, e.g. the interference of a reciprocal common mode and a gyrating differential mode. To show how non-reciprocity arises in the differential mode, the square-wave modulation of transmission realized by the two bridge circuits is plotted in Fig. 7.1b. If no delay is included between them, a differential signal on the upper (odd excitation of ports 1 & 3) or lower (odd excitation of ports 2 & 4) is modulated in time according to Fig. 7.1c, and the network is reciprocal (and scatters the incident signal into sidebands spaced by odd multiples of the modulation rate Ω). If, however, a delay τ of one-quarter the modulation period $T/4 = \pi/(2\Omega)$ is inserted between the two bridge circuits, reciprocity is broken, and the incident signal’s frequency is unchanged. A signal incident on the upper port is modulated by (Fig. 7.1d and Fig. 7.1e)

$$\text{sign}(\cos[\Omega t]) \times \text{sign}(\sin[\Omega t + \pi/4]) = 1, \quad (7.1)$$

whereas a signal incident on the lower port is modulated by (Fig. 7.1f and Fig. 7.1g)

$$\text{sign}(\sin[\Omega t]) \times \text{sign}(\cos[\Omega t + \pi/4]) = -1. \quad (7.2)$$

The circuit’s odd-mode therefore realizes a gyrator.

Prospects for such a device are extremely attractive given the high power-handling of these SQUID-array based devices, as their integration with a broadband low-noise amplifier [157] could enable scalable frequency-domain multiplexing of many-qubit systems with near-unit measurement efficiency. Given the current state of quantum error-correction and architectures for quantum information processing with superconducting circuits, such signal-processing innovations will almost certainly be necessary for construction of any superconducting quantum computer intended to be more than a proof-of-principle.

Bibliography

- [1] R. P. Feynman, “Simulating physics with computers,” International Journal of Theoretical Physics, vol. 21, no. 6, pp. 467–488, Jun 1982. [Online]. Available: <https://doi.org/10.1007/BF02650179>
- [2] —, “Quantum mechanical computers,” Foundations of Physics, vol. 16, no. 6, pp. 507–531, Jun 1986. [Online]. Available: <https://doi.org/10.1007/BF01886518>
- [3] D. Deutsch, “Quantum theory, the church-turing principle and the universal quantum computer,” Proceedings of the Royal Society of London A: Mathematical, Physical and Engineering Sciences, vol. 400, no. 1818, pp. 97–117, 1985.
- [4] —, “Quantum computational networks,” Proceedings of the Royal Society of London A: Mathematical, Physical and Engineering Sciences, vol. 425, no. 1868, pp. 73–90, 1989. [Online]. Available: <http://rspa.royalsocietypublishing.org/content/425/1868/73>
- [5] P. Shor, “Lecture notes in computer science,” in Algorithmic Number Theory: First International Symposium, L. M. Adleman and M.-D. A. Huang, Eds. New York: Springer, 1994, p. 289.
- [6] R. L. Rivest, A. Shamir, and L. Adleman, “A method for obtaining digital signatures and public-key cryptosystems,” Commun. ACM, vol. 21, no. 2, pp. 120–126, Feb. 1978. [Online]. Available: <http://doi.acm.org/10.1145/359340.359342>
- [7] L. K. Grover, “Quantum mechanics helps in searching for a needle in a haystack,” Phys. Rev. Lett., vol. 79, pp. 325–328, Jul 1997. [Online]. Available: <https://link.aps.org/doi/10.1103/PhysRevLett.79.325>
- [8] M. H. Yung, , J. D. Whitfield, S. Boixo, D. G. Tempel, and A. Aspuru-Guzik, Advances in Chemical Physics, Volume 154: Quantum Information and Computation for Chemistry, K. B. Whaley, A. R. Dinner, and S. A. Rice, Eds. John Wiley & Sons, 2014.
- [9] M. B. Hastings, D. Wecker, B. Bauer, and M. Troyer, “Improving quantum algorithms for quantum chemistry,” Quantum information and computation, vol. 1, no. 1-2, p. 00010021, 2015.
- [10] D. Poulin, M. B. Hastings, D. Wecker, N. Wiebe, A. C. Doherty, and M. Troyer, “The trotter step size required for accurate quantum simulation of quantum chemistry,” Quantum information and computation, vol. 15, no. 5-6, p. 03610384, 2015.

- [11] A. K. Ekert, “Quantum cryptography based on bell’s theorem,” *Phys. Rev. Lett.*, vol. 67, pp. 661–663, Aug 1991. [Online]. Available: <https://link.aps.org/doi/10.1103/PhysRevLett.67.661>
- [12] W. Heisenberg, *The physical principles of the quantum theory*. Courier Corporation, 1949.
- [13] C. Gardiner and P. Zoller, *Quantum noise: a handbook of Markovian and non-Markovian quantum stochastic methods with applications to quantum optics*. Springer Science & Business Media, 2004, vol. 56.
- [14] H. Nyquist, “Thermal agitation of electric charge in conductors,” *Phys. Rev.*, vol. 32, pp. 110–113, Jul 1928. [Online]. Available: <https://link.aps.org/doi/10.1103/PhysRev.32.110>
- [15] H. B. Callen and T. A. Welton, “Irreversibility and generalized noise,” *Phys. Rev.*, vol. 83, pp. 34–40, Jul 1951. [Online]. Available: <https://link.aps.org/doi/10.1103/PhysRev.83.34>
- [16] Braginskii, “Quantum-mechanical limitations in macroscopic experiments and modern experimental technique.”
- [17] V. B. Braginsky, Y. I. Vorontsov, and K. S. Thorne, “Quantum nondemolition measurements,” *Science*, vol. 209, no. 4456, pp. 547–557, 1980. [Online]. Available: <http://science.sciencemag.org/content/209/4456/547>
- [18] G. Nogues, A. Rauschenbeutel, S. Osnaghi, M. Brune, J. M. Raimond, and S. Haroche, “Seeing a single photon without destroying it,” *Nature*, vol. 400, no. 6741, p. 239, 1999.
- [19] H. A. Lorentz, “The theorem of poynting concerning the energy in the electromagnetic field and two general propositions concerning the propagation of light,” *Amsterdammer Akademie der Wetenschappen*, vol. 4, p. 176, 1896.
- [20] J. Kerckhoff, L. Bouten, A. Silberfarb, and H. Mabuchi, “Physical model of continuous two-qubit parity measurement in a cavity-qed network,” *Phys. Rev. A*, vol. 79, p. 024305, Feb 2009. [Online]. Available: <https://link.aps.org/doi/10.1103/PhysRevA.79.024305>
- [21] N. Roch, M. E. Schwartz, F. Motzoi, C. Macklin, R. Vijay, A. W. Eddins, A. N. Korotkov, K. B. Whaley, M. Sarovar, and I. Siddiqi, “Observation of measurement-induced entanglement and quantum trajectories of remote superconducting qubits,” *Physical review letters*, vol. 112, no. 17, p. 170501, 2014.
- [22] A. Narla, S. Shankar, M. Hatridge, Z. Leghtas, K. M. Sliwa, E. Zalys-Geller, S. O. Mundhada, W. Pfaff, L. Frunzio, R. J. Schoelkopf, and M. H. Devoret, “Robust concurrent remote entanglement between two superconducting qubits,” *Physical Review X*, vol. 6, no. 3, p. 031036, 2016.
- [23] H. Pichler, T. Ramos, A. J. Daley, and P. Zoller, “Quantum optics of chiral spin networks,” *Phys. Rev. A*, vol. 91, p. 042116, Apr 2015. [Online]. Available: <https://link.aps.org/doi/10.1103/PhysRevA.91.042116>
- [24] M. A. Castellanos-Beltran, K. D. Irwin, G. C. Hilton, L. R. Vale, and K. W. Lehnert, “Amplification and squeezing of quantum noise with a tunable josephson metamaterial,” *Nature Physics*, vol. 4, no. 12, pp. 929–931, 2008.

- [25] N. Bergeal, R. Vijay, V. E. Manucharyan, I. Siddiqi, R. J. Schoelkopf, S. M. Girvin, and M. H. Devoret, “Analog information processing at the quantum limit with a josephson ring modulator,” *Nature Physics*, vol. 6, no. 4, pp. 296–302, 2010.
- [26] A. G. Fowler, M. Mariantoni, J. M. Martinis, and A. N. Cleland, “Surface codes: Towards practical large-scale quantum computation,” *Phys. Rev. A*, vol. 86, p. 032324, Sep 2012. [Online]. Available: <https://link.aps.org/doi/10.1103/PhysRevA.86.032324>
- [27] K. K. Likharev and V. K. Semenov, “Rsfq logic/memory family: a new josephson-junction technology for sub-terahertz-clock-frequency digital systems,” *IEEE Transactions on Applied Superconductivity*, vol. 1, no. 1, pp. 3–28, March 1991.
- [28] J. Zmuidzinas, “Superconducting microresonators: Physics and applications,” *Annu. Rev. Condens. Matter Phys.*, vol. 3, no. 1, pp. 169–214, 2012.
- [29] W. Holland, D. Bintley, E. Chapin, A. Chrysostomou, G. Davis, J. Dempsey, W. Duncan, M. Fich, P. Friberg, M. Halpern et al., “Scuba-2: the 10 000 pixel bolometer camera on the james clerk maxwell telescope,” *Monthly Notices of the Royal Astronomical Society*, vol. 430, no. 4, pp. 2513–2533, 2013.
- [30] B. M. Brubaker, L. Zhong, Y. V. Gurevich, S. B. Cahn, S. K. Lamoreaux, M. Simanovskaia, J. R. Root, S. M. Lewis, S. Al Kenany, K. M. Backes, I. Urdinaran, N. M. Rapidis, T. M. Shokair, K. A. van Bibber, D. A. Palken, M. Malnou, W. F. Kindel, M. A. Anil, K. W. Lehnert, and G. Carosi, “First results from a microwave cavity axion search at 24 μeV ,” *Phys. Rev. Lett.*, vol. 118, p. 061302, Feb 2017. [Online]. Available: <https://link.aps.org/doi/10.1103/PhysRevLett.118.061302>
- [31] P. Wolf, S. Bize, A. Clairon, A. N. Luiten, G. Santarelli, and M. E. Tobar, “Tests of lorentz invariance using a microwave resonator,” *Phys. Rev. Lett.*, vol. 90, p. 060402, Feb 2003. [Online]. Available: <https://link.aps.org/doi/10.1103/PhysRevLett.90.060402>
- [32] R. Hughes, “A quantum information science and technology roadmap,” Los Alamos National Laboratory, Tech. Rep., 2004.
- [33] P. Zoller, T. Beth, D. Binosi, R. Blatt, H. Briegel, D. Bruss, T. Calarco, J. I. Cirac, D. Deutsch, J. Eisert, A. Ekert, C. Fabre, N. Gisin, P. Grangiere, M. Grassl, S. Haroche, A. Imamoglu, A. Karlson, J. Kempe, L. Kouwenhoven, S. Kröll, G. Leuchs, M. Lewenstein, D. Loss, N. Lütkenhaus, S. Massar, J. E. Mooij, M. B. Plenio, E. Polzik, S. Popescu, G. Rempe, A. Sergienko, D. Suter, J. Twamley, G. Wendin, R. Werner, A. Winter, J. Wrachtrup, and A. Zeilinger, “Quantum information processing and communication,” *The European Physical Journal D - Atomic, Molecular, Optical and Plasma Physics*, vol. 36, no. 2, pp. 203–228, Nov 2005. [Online]. Available: <https://doi.org/10.1140/epjd/e2005-00251-1>
- [34] Z. Leghtas, G. Kirchmair, B. Vlastakis, R. J. Schoelkopf, M. H. Devoret, and M. Mirrahimi, “Hardware-efficient autonomous quantum memory protection,” *Phys. Rev. Lett.*, vol. 111, p. 120501, Sep 2013. [Online]. Available: <https://link.aps.org/doi/10.1103/PhysRevLett.111.120501>
- [35] S. Haroche and J.-M. Raimond, *Exploring the quantum: atoms, cavities, and photons*. Oxford university press, 2006.

- [36] V. V. Albert, K. Noh, K. Duivenvoorden, R. T. Brierley, P. Reinhold, C. Vuillot, L. Li, C. Shen, S. M. Girvin, B. M. Terhal, and L. Jiang, “Performance and structure of bosonic codes,” *ArXiv e-prints*, Aug. 2017.
- [37] A. Kitaev, “Fault-tolerant quantum computation by anyons,” *Annals of Physics*, vol. 303, no. 1, pp. 2 – 30, 2003. [Online]. Available: <http://www.sciencedirect.com/science/article/pii/S0003491602000180>
- [38] M. H. Devoret and R. J. Schoelkopf, “Superconducting circuits for quantum information: an outlook,” *Science*, vol. 339, no. 6124, pp. 1169–1174, 2013.
- [39] D. P. DiVincenzo *et al.*, “The physical implementation of quantum computation,” *arXiv preprint quant-ph/0002077*, 2000.
- [40] D. Nigg, M. Müller, E. A. Martinez, P. Schindler, M. Hennrich, T. Monz, M. A. Martin-Delgado, and R. Blatt, “Quantum computations on a topologically encoded qubit,” *Science*, vol. 345, no. 6194, pp. 302–305, 2014. [Online]. Available: <http://science.sciencemag.org/content/345/6194/302>
- [41] C. Sayrin, I. Dotsenko, X. Zhou, B. Peaudecerf, T. Rybarczyk, S. Gleyzes, P. Rouchon, M. Mirrahimi, H. Amini, M. Brune *et al.*, “Real-time quantum feedback prepares and stabilizes photon number states,” *Nature*, vol. 477, no. 7362, pp. 73–77, 2011.
- [42] G. Waldherr, Y. Wang, S. Zaiser, M. Jamali, T. Schulte-Herbrüggen, H. Abe, T. Ohshima, J. Isoya, J. Du, P. Neumann *et al.*, “Quantum error correction in a solid-state hybrid spin register,” *Nature*, vol. 506, no. 7487, pp. 204–207, 2014.
- [43] M. D. Reed, L. DiCarlo, S. E. Nigg, L. Sun, L. Frunzio, S. M. Girvin, and R. J. Schoelkopf, “Realization of three-qubit quantum error correction with superconducting circuits,” *Nature*, vol. 482, p. 382, 2012.
- [44] D. Ristè, C. C. Bultink, K. W. Lehnert, and L. DiCarlo, “Feedback control of a solid-state qubit using high-fidelity projective measurement,” *Phys. Rev. Lett.*, vol. 109, p. 240502, Dec 2012. [Online]. Available: <https://link.aps.org/doi/10.1103/PhysRevLett.109.240502>
- [45] P. Campagne-Ibarcq, E. Flurin, N. Roch, D. Darson, P. Morfin, M. Mirrahimi, M. H. Devoret, F. Mallet, and B. Huard, “Persistent control of a superconducting qubit by stroboscopic measurement feedback,” *Phys. Rev. X*, vol. 3, p. 021008, May 2013. [Online]. Available: <https://link.aps.org/doi/10.1103/PhysRevX.3.021008>
- [46] J. Kelly, R. Barends, A. G. Fowler, A. Megrant, E. Jeffrey, T. C. White, D. Sank, J. Y. Mutus, B. Campbell, Y. Chen *et al.*, “State preservation by repetitive error detection in a superconducting quantum circuit,” *Nature*, vol. 519, no. 7541, pp. 66–69, 2015.
- [47] N. Ofek, A. Petrenko, R. Heeres, P. Reinhold, Z. Leghtas, B. Vlastakis, Y. Liu, L. Frunzio, S. Girvin, L. Jiang *et al.*, “Extending the lifetime of a quantum bit with error correction in superconducting circuits,” *Nature*, 2016.
- [48] R. W. Heeres, P. Reinhold, N. Ofek, L. Frunzio, L. Jiang, M. H. Devoret, and R. J. Schoelkopf, “Implementing a universal gate set on a logical qubit encoded in an oscillator,” *Nature Communications*, vol. 8, 2017.

- [49] S. Touzard, A. Grimm, Z. Leghtas, S. Mundhada, P. Reinhold, R. Heeres, C. Axline, M. Reagor, K. Chou, J. Blumoff et al., “Coherent oscillations in a quantum manifold stabilized by dissipation,” arXiv preprint arXiv:1705.02401, 2017.
- [50] P. W. Shor, “Scheme for reducing decoherence in quantum computer memory,” Phys. Rev. A, vol. 52, pp. R2493–R2496, Oct 1995. [Online]. Available: <https://link.aps.org/doi/10.1103/PhysRevA.52.R2493>
- [51] A. Steane, “Multiple-particle interference and quantum error correction,” Proceedings of the Royal Society of London A: Mathematical, Physical and Engineering Sciences, vol. 452, no. 1954, pp. 2551–2577, 1996.
- [52] E. Knill and R. Laflamme, “Theory of quantum error-correcting codes,” Phys. Rev. A, vol. 55, pp. 900–911, Feb 1997. [Online]. Available: <https://link.aps.org/doi/10.1103/PhysRevA.55.900>
- [53] M. H. Freedman and D. A. Meyer, “Projective plane and planar quantum codes,” Foundations of Computational Mathematics, vol. 1, no. 3, pp. 325–332, Jul 2001. [Online]. Available: <https://doi.org/10.1007/s102080010013>
- [54] M. Takita, A. D. Córcoles, E. Magesan, B. Abdo, M. Brink, A. Cross, J. M. Chow, and J. M. Gambetta, “Demonstration of weight-four parity measurements in the surface code architecture,” Physical review letters, vol. 117, no. 21, p. 210505, 2016.
- [55] J. M. Gambetta, J. M. Chow, and M. Steffen, “Building logical qubits in a superconducting quantum computing system,” NPJ Quantum Information, vol. 3, no. 2, 2017.
- [56] U. Vool and M. Devoret, “Introduction to quantum electromagnetic circuits,” International Journal of Circuit Theory and Applications, vol. 45, no. 7, pp. 897–934, 2017, cta.2359. [Online]. Available: <http://dx.doi.org/10.1002/cta.2359>
- [57] X. Gu, A. F. Kockum, A. Miranowicz, Y.-x. Liu, and F. Nori, “Microwave photonics with superconducting quantum circuits,” arXiv preprint arXiv:1707.02046, 2017.
- [58] K. K. Likharev, Dynamics of Josephson junctions and circuits. Gordon and Breach science publishers, 1986.
- [59] A. Blais, R.-S. Huang, A. Wallraff, S. M. Girvin, and R. J. Schoelkopf, “Cavity quantum electrodynamics for superconducting electrical circuits: An architecture for quantum computation,” Physical Review A, vol. 69, no. 6, p. 062320, 2004.
- [60] R. Vijay, D. H. Slichter, and I. Siddiqi, “Observation of quantum jumps in a superconducting artificial atom,” Phys. Rev. Lett., vol. 106, p. 110502, Mar 2011. [Online]. Available: <http://link.aps.org/doi/10.1103/PhysRevLett.106.110502>
- [61] D. Ristè, J. G. van Leeuwen, H.-S. Ku, K. W. Lehnert, and L. DiCarlo, “Initialization by measurement of a superconducting quantum bit circuit,” Phys. Rev. Lett., vol. 109, p. 050507, Aug 2012. [Online]. Available: <https://link.aps.org/doi/10.1103/PhysRevLett.109.050507>
- [62] J. Koch, T. M. Yu, J. Gambetta, A. A. Houck, D. I. Schuster, J. Majer, A. Blais, M. H. Devoret, S. M. Girvin, and R. J. Schoelkopf, “Charge-insensitive qubit design derived from the cooper pair box,” Phys. Rev. A, vol. 76, p. 042319, Oct 2007. [Online]. Available: <https://link.aps.org/doi/10.1103/PhysRevA.76.042319>

- [63] A. P. Sears, A. Petrenko, G. Catelani, L. Sun, H. Paik, G. Kirchmair, L. Frunzio, L. I. Glazman, S. M. Girvin, and R. J. Schoelkopf, “Photon shot noise dephasing in the strong-dispersive limit of circuit qed,” *Phys. Rev. B*, vol. 86, p. 180504, Nov 2012. [Online]. Available: <https://link.aps.org/doi/10.1103/PhysRevB.86.180504>
- [64] C. Wang, Y. Y. Gao, P. Reinhold, R. Heeres, N. Ofek, K. Chou, C. Axline, M. Reagor, J. Blumoff, K. Sliwa et al., “A schrödinger cat living in two boxes,” *Science*, vol. 352, no. 6289, pp. 1087–1091, 2016.
- [65] M. Reagor, W. Pfaff, C. Axline, R. W. Heeres, N. Ofek, K. Sliwa, E. Holland, C. Wang, J. Blumoff, K. Chou, M. J. Hatridge, L. Frunzio, M. H. Devoret, L. Jiang, and R. J. Schoelkopf, “Quantum memory with millisecond coherence in circuit qed,” *Phys. Rev. B*, vol. 94, p. 014506, Jul 2016. [Online]. Available: <https://link.aps.org/doi/10.1103/PhysRevB.94.014506>
- [66] C. M. Caves, “Quantum limits on noise in linear amplifiers,” *Phys. Rev. D*, vol. 26, pp. 1817–1839, Oct 1982. [Online]. Available: <https://link.aps.org/doi/10.1103/PhysRevD.26.1817>
- [67] G. G. Stokes, “On the perfect blackness of the central spot in newton’s rings, and on the verification of fresnel’s formulae for the intensities of reflected and refracted rays,” *Cambridge and Dublin Mathematical Journal*, vol. 4, pp. 1–14, 1849.
- [68] H. Von Helmholtz, *Handbuch der physiologischen Optik*. Voss, 1867, vol. 9.
- [69] H. B. G. Casimir, “On onsager’s principle of microscopic reversibility,” *Rev. Mod. Phys.*, vol. 17, pp. 343–350, Apr 1945. [Online]. Available: <https://link.aps.org/doi/10.1103/RevModPhys.17.343>
- [70] R. Fleury, D. Sounas, C. F. Sieck, M. R. Haberman, and A. Alù, “Sound isolation and giant linear nonreciprocity in a compact acoustic circulator,” *Science*, vol. 343, no. 6170, 2013.
- [71] C. Coullais, D. Sounas, and A. Alù, “Static non-reciprocity in mechanical metamaterials,” *Nature*, vol. 542, no. 461, 2017.
- [72] Z. Yang, F. Gao, X. Shi, X. Lin, Z. Gao, Y. Chong, and B. Zhang, “Topological acoustics,” *Phys. Rev. Lett.*, vol. 114, p. 114301, Mar 2015. [Online]. Available: <https://link.aps.org/doi/10.1103/PhysRevLett.114.114301>
- [73] P. Wang, L. Lu, and K. Bertoldi, “Topological phononic crystals with one-way elastic edge waves,” *Phys. Rev. Lett.*, vol. 115, p. 104302, Sep 2015. [Online]. Available: <https://link.aps.org/doi/10.1103/PhysRevLett.115.104302>
- [74] S. A. Cummer, J. Christensen, and A. Alù, “Controlling sound with acoustic metamaterials,” *Nature Reviews Materials*, vol. 1, p. 16001, 2016.
- [75] G. Viola and D. P. DiVincenzo, “Hall effect gyrators and circulators,” *Physical Review X*, vol. 4, no. 2, p. 021019, 2014.
- [76] A. C. Mahoney, J. I. Colless, S. J. Pauka, J. M. Hornibrook, J. D. Watson, G. C. Gardner, M. J. Manfra, A. C. Doherty, and D. J. Reilly, “On-chip microwave quantum hall circulator,” *Phys. Rev. X*, vol. 7, p. 011007, Jan 2017.

- [77] A. C. Mahoney, J. I. Colless, L. Peeters, S. J. Pauka, E. J. Fox, X. Kou, L. Pan, D. G.-G. K. L. Wang, and D. J. Reilly, “Zero-field edge magnetoplasmons in a magnetic topological insulator,” arXiv preprint arXiv:1703.03122, 2017.
- [78] D. M. Pozar, “Microwave engineering. 4th,” 2011.
- [79] D. Jalas, A. Petrov, M. Eich, W. Freude, S. Fan, Z. Yu, R. Baets, M. Popović, A. Melloni, J. D. Joannopoulos, M. Vanwolleghem, C. R. Doerr, and H. Renner, “What is and what is not an optical isolator,” Nature Photonics, vol. 7, p. 579582, 2013.
- [80] C. Vassallo, Optical Waveguide Concepts, ser. 5. Sara Burgerhartstraat 25 P.O. Box 211, 1000 AE Amsterdam, The Netherlands: Elsevier, 1991, vol. 1, ch. 1, pp. 15–23.
- [81] F. L. Pedrotti, L. S. Pedrotti, and L. M. Pedrotti, Introduction to optics, 3rd ed. Prentice Hall, 2007.
- [82] A. Kamal, J. Clarke, and M. H. Devoret, “Noiseless non-reciprocity in a parametric active device,” Nature Physics, vol. 7, no. 4, pp. 311–315, 2011.
- [83] C. E. Fay and R. L. Comstock, “Operation of the ferrite junction circulator,” Microwave Theory and Techniques, IEEE Transactions on, vol. 13, no. 1, pp. 15–27, 1965.
- [84] J. Fujita, M. Levy, R. M. O. Jr., L. Wilkens, and H. Dtsch, “Waveguide optical isolator based on machzehnder interferometer,” Applied Physics Letters, vol. 76, no. 16, pp. 2158–2160, 2000. [Online]. Available: <http://dx.doi.org/10.1063/1.126284>
- [85] L. Bi, J. Hu, P. Jiang, D. H. Kim, G. F. Dionne, L. C. Kimerling, and C. Ross, “On-chip optical isolation in monolithically integrated non-reciprocal optical resonators,” Nature Photonics, vol. 5, no. 12, pp. 758–762, 2011.
- [86] Y. Shoji, T. Mizumoto, H. Yokoi, I.-W. Hsieh, and R. M. O. Jr., “Magneto-optical isolator with silicon waveguides fabricated by direct bonding,” Applied Physics Letters, vol. 92, no. 7, p. 071117, 2008. [Online]. Available: <http://dx.doi.org/10.1063/1.2884855>
- [87] W. Śmigaj, J. Romero-Vivas, B. Gralak, L. Magdenko, B. Dagens, and M. Vanwolleghem, “Magneto-optical circulator designed for operation in a uniform external magnetic field,” Opt. Lett., vol. 35, no. 4, pp. 568–570, Feb 2010. [Online]. Available: <http://ol.osa.org/abstract.cfm?URI=ol-35-4-568>
- [88] Z. Wang and S. Fan, “Optical circulators in two-dimensional magneto-optical photonic crystals,” Opt. Lett., vol. 30, no. 15, pp. 1989–1991, Aug 2005. [Online]. Available: <http://ol.osa.org/abstract.cfm?URI=ol-30-15-1989>
- [89] K. Fang, Z. Yu, V. Liu, and S. Fan, “Ultracompact nonreciprocal optical isolator based on guided resonance in a magneto-optical photonic crystal slab,” Opt. Lett., vol. 36, no. 21, pp. 4254–4256, Nov 2011. [Online]. Available: <http://ol.osa.org/abstract.cfm?URI=ol-36-21-4254>
- [90] A. M. Mahmoud, A. R. Davoyan, and N. Engheta, “All-passive nonreciprocal metastructure,” Nature Communications, vol. 6, no. 8359, 2015.

- [91] K. Gallo, G. Assanto, K. R. Parameswaran, and M. M. Fejer, “All-optical diode in a periodically poled lithium niobate waveguide,” *Applied Physics Letters*, vol. 79, no. 3, pp. 314–316, 2001. [Online]. Available: <http://dx.doi.org/10.1063/1.1386407>
- [92] L. Fan, J. Wang, L. T. Varghese, H. Shen, B. Niu, Y. Xuan, A. M. Weiner, and M. Qi, “An all-silicon passive optical diode,” *Science*, vol. 335, no. 6067, pp. 447–450, 2012. [Online]. Available: <http://science.sciencemag.org/content/335/6067/447>
- [93] Y. Zhang, D. Li, C. Zeng, Z. Huang, Y. Wang, Q. Huang, Y. Wu, J. Yu, and J. Xia, “Silicon optical diode based on cascaded photonic crystal cavities,” *Opt. Lett.*, vol. 39, no. 6, pp. 1370–1373, Mar 2014. [Online]. Available: <http://ol.osa.org/abstract.cfm?URI=ol-39-6-1370>
- [94] L. A. Zadeh and C. A. Deoser, *Linear system theory*. McGraw Hill, 1963.
- [95] B. D. O. Anderson and R. W. Newcomb, “On reciprocity and time-variable networks,” *Proceedings of the IEEE*, vol. 53, no. 10, pp. 1674–1674, 1965.
- [96] D. L. Sounas, C. Caloz, and A. Alù, “Giant non-reciprocity at the subwavelength scale using angular momentum-biased metamaterials,” *Nature communications*, vol. 4, p. 2407, 2013.
- [97] K. Fang, Z. Yu, and S. Fan, “Experimental demonstration of a photonic aharonov-bohm effect at radio frequencies,” *Phys. Rev. B*, vol. 87, p. 060301, Feb 2013.
- [98] B. Abdo, K. Sliwa, S. Shankar, M. Hatridge, L. Frunzio, R. J. Schoelkopf, and M. H. Devoret, “Josephson directional amplifier for quantum measurement of superconducting circuits,” *Physical review letters*, vol. 112, no. 16, p. 167701, 2014.
- [99] K. M. Sliwa, M. Hatridge, A. Narla, S. Shankar, L. Frunzio, R. J. Schoelkopf, and M. H. Devoret, “Reconfigurable josephson circulator/directional amplifier,” *Phys. Rev. X*, vol. 5, p. 041020, 2015.
- [100] F. Lecocq, L. Ranzani, G. A. Peterson, K. Cicak, R. W. Simmonds, J. D. Teufel, and J. Aumentado, “Nonreciprocal microwave signal processing with a field-programmable josephson amplifier,” *Phys. Rev. Applied*, vol. 7, p. 024028, Feb 2017. [Online]. Available: <https://link.aps.org/doi/10.1103/PhysRevApplied.7.024028>
- [101] B. Abdo, M. Brink, and J. M. Chow, “Gyrator operation using josephson mixers,” *Phys. Rev. Applied*, vol. 8, p. 034009, Sep 2017. [Online]. Available: <https://link.aps.org/doi/10.1103/PhysRevApplied.8.034009>
- [102] E. Li, B. J. Eggleton, K. Fang, and S. Fan, “Photonic aharonov-bohm effect in photon-phonon interactions,” *Nature communications*, vol. 5, 2014.
- [103] G. A. Peterson, F. Lecocq, K. Cicak, R. W. Simmonds, J. Aumentado, and J. D. Teufel, “Demonstration of efficient nonreciprocity in a microwave optomechanical circuit,” *Phys. Rev. X*, vol. 7, p. 031001, Jul 2017. [Online]. Available: <https://link.aps.org/doi/10.1103/PhysRevX.7.031001>
- [104] N. R. Bernier, L. D. Toth, A. Koottandavida, M. A. Ioannou, D. Malz, A. Nunnenkamp, A. Feofanov, and T. Kippenberg, “Nonreciprocal reconfigurable microwave optomechanical circuit,” *arXiv*, 2017.

- [105] S. Barzanjeh, M. Wulf, M. Peruzzo, M. Kalaei, P. B. Dieterle, O. Painter, and J. M. Fink, “Mechanical on-chip microwave circulator,” *arXiv preprint arXiv:1706.00376*, 2017.
- [106] F. Ruesink, M.-A. Miri, A. Al, and E. Verhagen, “Nonreciprocity and magnetic-free isolation based on optomechanical interactions,” *Nature communications*, vol. 7, p. 13662, 2016.
- [107] K. Fang, J. Luo, A. Metelmann, M. H. Matheny, F. Marquardt, A. A. Clerk, and O. Painter, “Generalized non-reciprocity in an optomechanical circuit via synthetic magnetism and reservoir engineering,” *Nature Physics*, vol. 13, no. 5, pp. 465–471, 2017.
- [108] L. Ranzani and J. Aumentado, “Graph-based analysis of nonreciprocity in coupled-mode systems,” *New Journal of Physics*, vol. 17, no. 2, p. 023024, 2015.
- [109] K. Fang, Z. Yu, and S. Fan, “Realizing effective magnetic field for photons by controlling the phase of dynamic modulation,” *Nature Physics*, vol. 6, no. 11, pp. 782–787, 2012.
- [110] —, “Photonic aharonov-bohm effect based on dynamic modulation,” *Phys. Rev. Lett.*, vol. 108, p. 153901, Apr 2012.
- [111] L. D. Tzauang, K. Fang, P. Nussenzeig, S. Fan, and M. Lipson, “Non-reciprocal phase shift induced by an effective magnetic flux for light,” *Nature photonics*, vol. 8, no. 9, 2014.
- [112] R. Peierls, “Zur theorie des diamagnetismus von leitungselektronen,” *Zeitschrift für Physik A Hadrons and Nuclei*, vol. 80, no. 11, pp. 763–791, 1933.
- [113] S. Khorasani, “Diamond configuration for non-reciprocal transmission,” *IEEE Journal of Quantum Electronics*, 2017.
- [114] B. Anderson and R. Newcomb, “The time-variable lattice and nonreciprocal rlc networks,” *Circuit Theory, IEEE Transactions on*, vol. 13, no. 2, pp. 233–235, 1966.
- [115] J. Kerckhoff, K. Lalumière, B. J. Chapman, A. Blais, and K. W. Lehnert, “On-chip superconducting microwave circulator from synthetic rotation,” *Phys. Rev. Applied*, vol. 4, p. 034002, Sep 2015. [Online]. Available: <http://link.aps.org/doi/10.1103/PhysRevApplied.4.034002>
- [116] E. I. Rosenthal, B. J. Chapman, A. P. Higginbotham, J. Kerckhoff, and K. W. Lehnert, “Breaking lorentz reciprocity with frequency conversion and delay,” *Phys. Rev. Lett.*, vol. 119, p. 147703, Oct 2017. [Online]. Available: <https://link.aps.org/doi/10.1103/PhysRevLett.119.147703>
- [117] S. K. Ibrahim, S. Bhandare, D. Sandel, H. Zhang, and R. Noe, “Non-magnetic 30 db integrated optical isolator in iii/v material,” *Electronics Letters*, vol. 40, no. 20, pp. 1293–1294, 2004.
- [118] S. Bhandare, S. K. Ibrahim, D. Sandel, H. Zhang, F. Wust, and R. Noé, “Novel nonmagnetic 30-db traveling-wave single-sideband optical isolator integrated in iii/v material,” *IEEE Journal of selected topics in quantum electronics*, vol. 11, no. 2, pp. 417–421, 2005.
- [119] C. R. Doerr, N. Dupuis, and L. Zhang, “Optical isolator using two tandem phase modulators,” *Opt. Lett.*, vol. 36, no. 21, pp. 4293–4295, Nov 2011. [Online]. Available: <http://ol.osa.org/abstract.cfm?URI=ol-36-21-4293>

- [120] Y. Yang, C. Galland, Y. Liu, K. Tan, R. Ding, Q. Li, K. Bergman, T. Baehr-Jones, and M. Hochberg, “Experimental demonstration of broadband lorentz non-reciprocity in an integrable photonic architecture based on mach-zehnder modulators,” *Optics express*, vol. 22, no. 14, pp. 17 409–17 422, 2014.
- [121] A. Metelmann and A. Clerk, “Nonreciprocal photon transmission and amplification via reservoir engineering,” *Physical Review X*, vol. 5, no. 2, p. 021025, 2015.
- [122] A. Metelmann and H. E. Türeci, “Nonreciprocal signal routing in an active quantum network,” *arXiv preprint arXiv:1703.04052*, 2017.
- [123] A. Metelmann and A. A. Clerk, “Nonreciprocal quantum interactions and devices via autonomous feedforward,” *Phys. Rev. A*, vol. 95, p. 013837, Jan 2017. [Online]. Available: <https://link.aps.org/doi/10.1103/PhysRevA.95.013837>
- [124] S. Manipatruni, J. T. Robinson, and M. Lipson, “Optical nonreciprocity in optomechanical structures,” *Phys. Rev. Lett.*, vol. 102, p. 213903, May 2009. [Online]. Available: <https://link.aps.org/doi/10.1103/PhysRevLett.102.213903>
- [125] Z. Yu and S. Fan, “Complete optical isolation created by indirect interband photonic transitions,” *Nature Photonics*, vol. 3, 2009.
- [126] ———, “Optical isolation based on nonreciprocal phase shift induced by interband photonic transitions,” *Applied Physics Letters*, vol. 94, no. 17, p. 171116, 2009.
- [127] H. Lira, Z. Yu, S. Fan, and M. Lipson, “Electrically driven nonreciprocity induced by interband photonic transition on a silicon chip,” *Phys. Rev. Lett.*, vol. 109, p. 033901, Jul 2012. [Online]. Available: <https://link.aps.org/doi/10.1103/PhysRevLett.109.033901>
- [128] M. O. Scully and M. S. Zubairy, *Quantum optics*. Cambridge University Press, 1997.
- [129] B. D. H. Tellegen, “The gyrator, a new electric network element,” *Philips Res. Rep*, vol. 3, no. 2, pp. 81–101, 1948.
- [130] C. L. Hogan, “The ferromagnetic faraday effect at micro-wave frequencies and its applications,” *Rev. Mod. Phys.*, vol. 25, 1953.
- [131] B. J. Chapman, B. A. Moores, E. I. Rosenthal, J. Kerckhoff, and K. W. Lehnert, “General purpose multiplexing device for cryogenic microwave systems,” *Applied Physics Letters*, vol. 108, no. 22, p. 222602, 2016.
- [132] B. J. Chapman, E. I. Rosenthal, J. Kerckhoff, L. R. Vale, G. C. Hilton, and K. W. Lehnert, “Single-sideband modulator for frequency domain multiplexing of superconducting qubit readout,” *Applied Physics Letters*, vol. 110, p. 162601, 2017.
- [133] K. Lalumière, “Électrodynamique quantique en guide d’onde,” Ph.D. dissertation, Université de Sherbrooke, 2015.
- [134] G. Burkard, R. H. Koch, and D. P. DiVincenzo, “Multilevel quantum description of decoherence in superconducting qubits,” *Phys. Rev. B*, vol. 69, p. 064503, Feb 2004. [Online]. Available: <https://link.aps.org/doi/10.1103/PhysRevB.69.064503>

- [135] G. Burkard, “Circuit theory for decoherence in superconducting charge qubits,” *Phys. Rev. B*, vol. 71, p. 144511, Apr 2005. [Online]. Available: <https://link.aps.org/doi/10.1103/PhysRevB.71.144511>
- [136] O. Heaviside, *Electrical Papers*. MacMillan and Co, 1894, vol. 2.
- [137] C. K. Andersen, J. Kerckhoff, K. W. Lehnert, B. J. Chapman, and K. Mølmer, “Closing a quantum feedback loop inside a cryostat: Autonomous state preparation and long-time memory of a superconducting qubit,” *Phys. Rev. A*, vol. 93, p. 012346, Jan 2016. [Online]. Available: <https://link.aps.org/doi/10.1103/PhysRevA.93.012346>
- [138] B. J. Chapman, E. I. Rosenthal, J. Kerckhoff, B. A. Moores, L. R. Vale, G. C. Hilton, K. Lalumière, A. Blais, and K. W. Lehnert, “Widely tunable on-chip microwave circulator for superconducting quantum circuits,” *arXiv preprint arXiv:1707.04565*, 2017.
- [139] W. Holland, M. MacIntosh, A. Fairley, D. Kelly, D. Montgomery, D. Gostick, E. Atad-Ettedgui, M. Ellis, I. Robson, M. Hollister, A. Woodcraft, P. Ade, I. Walker, K. Irwin, G. Hilton, W. Duncan, C. Reintsema, A. Walton, W. Parkes, C. Dunare, M. Fich, J. Kycia, M. Halpern, D. Scott, A. Gibb, J. Molnar, E. Chapin, D. Bintley, S. Craig, T. Chylek, T. Jenness, F. Economou, and G. Davis, “Scuba-2: a 10,000-pixel submillimeter camera for the james clerk maxwell telescope,” pp. 62 751E–62 751E–15, 2006. [Online]. Available: <http://dx.doi.org/10.1117/12.671186>
- [140] M. A. Castellanos-Beltran and K. W. Lehnert, “Widely tunable parametric amplifier based on a superconducting quantum interference device array resonator,” *Applied Physics Letters*, vol. 91, no. 8, p. 083509, 2007. [Online]. Available: <http://dx.doi.org/10.1063/1.2773988>
- [141] J. Kerckhoff, R. W. Andrews, H. S. Ku, W. F. Kindel, K. Cicak, R. W. Simmonds, and K. W. Lehnert, “Tunable coupling to a mechanical oscillator circuit using a coherent feedback network,” *Phys. Rev. X*, vol. 3, p. 021013, Jun 2013. [Online]. Available: <https://link.aps.org/doi/10.1103/PhysRevX.3.021013>
- [142] J. E. Sauvageau, C. J. Burroughs, P. A. A. Booij, M. W. Cromar, R. P. Benz, and J. A. Koch, “Superconducting integrated circuit fabrication with low temperature ecr-based pecvd sio/sub 2/dielectric films,” *Applied Superconductivity, IEEE Transactions on*, vol. 5, no. 2, pp. 2303–2309, 1995.
- [143] J. A. B. Mates, G. C. Hilton, K. D. Irwin, L. R. Vale, and K. W. Lehnert, “Demonstration of a multiplexer of dissipationless superconducting quantum interference devices,” *Applied Physics Letters*, vol. 92, no. 2, p. 023514, 2008.
- [144] G. Stan, S. B. Field, and J. M. Martinis, “Critical field for complete vortex expulsion from narrow superconducting strips,” *Phys. Rev. Lett.*, vol. 92, p. 097003, Mar 2004. [Online]. Available: <https://link.aps.org/doi/10.1103/PhysRevLett.92.097003>
- [145] T. Van Duzer and C. W. Turner, *Principles of superconductive devices and circuits*, 2nd ed. Prentice Hall, 1981.
- [146] N. W. Ashcroft and N. D. Mermin, *Solid state physics*. Holt, Rinehart and Winston, 1976.

- [147] H. Pothier, S. Guéron, D. Esteve, and M. H. Devoret, “Flux-modulated andreev current caused by electronic interference,” *Phys. Rev. Lett.*, vol. 73, pp. 2488–2491, Oct 1994. [Online]. Available: <https://link.aps.org/doi/10.1103/PhysRevLett.73.2488>
- [148] P. Dubos, H. Courtois, B. Pannetier, F. K. Wilhelm, A. D. Zaikin, and G. Schön, “Josephson critical current in a long mesoscopic s-n-s junction,” *Phys. Rev. B*, vol. 63, p. 064502, Jan 2001. [Online]. Available: <https://link.aps.org/doi/10.1103/PhysRevB.63.064502>
- [149] P. Mohanty and R. A. Webb, “High-field measurements of electron decoherence time in metallic nanowires: Switching off magnetic impurity spins,” *Phys. Rev. Lett.*, vol. 91, p. 066604, Aug 2003. [Online]. Available: <https://link.aps.org/doi/10.1103/PhysRevLett.91.066604>
- [150] D. Riste, M. Dukalski, C. A. Watson, G. de Lange, M. J. Tiggelman, Y. M. Blanter, K. W. Lehnert, R. N. Schouten, and L. DiCarlo, “Deterministic entanglement of superconducting qubits by parity measurement and feedback,” *Nature*, vol. 502, no. 7471, pp. 350–354, 2013.
- [151] S. Hacoen-Gourgy, L. S. Martin, E. Flurin, V. V. Ramasesh, K. B. Whaley, and I. Siddiqi, “Quantum dynamics of simultaneously measured non-commuting observables,” *Nature*, vol. 538, no. 7626, pp. 491–494, 2016.
- [152] J. B. Johnson, “Thermal agitation of electricity in conductors,” *Phys. Rev.*, vol. 32, pp. 97–109, Jul 1928. [Online]. Available: <https://link.aps.org/doi/10.1103/PhysRev.32.97>
- [153] Z. E. Research, “Strong growth potential for u.s. telecom industry,” September 2016. [Online]. Available: <https://www.zacks.com/commentary/89921/strong-growth-potential-for-us-telecom-industry>
- [154] H. W. Bode et al., *Network analysis and feedback amplifier design.* van Nostrand, 1945.
- [155] R. M. Fano, “Theoretical limitations on the broadband matching of arbitrary impedances,” *Journal of the Franklin Institute*, vol. 249, no. 1, pp. 57–83, 139–154, 1950.
- [156] T. Dinc, M. Tymchenko, A. Nagulu, D. Sounas, H. Krishnaswamy, and A. Alù, “Synchronized conductivity modulation to realize broadband lossless magnetic-free nonreciprocity,” *Nature Communications*, vol. 8, no. 275.
- [157] C. Macklin, K. O’Brien, D. Hover, M. E. Schwartz, V. Bolkhovskiy, X. Zhang, W. D. Oliver, and I. Siddiqi, “A near-quantum-limited josephson traveling-wave parametric amplifier,” *Science*, vol. 350, no. 6258, pp. 307–310, 2015.

Appendix A

Graph theory eigenfrequency analysis for a half-circulator

Consider the network in Fig. A.1a. Its resonant frequencies may be calculated with a graph-theoretical approach [134, 135], in which each element in the network is designated as a (tree) branch or a chord. Together, the branches form a tree—an object which encloses no circuit loops, but which creates a loop with the addition of any chord. Note that for networks of non-trivial size, there are multiple ways to define a tree.

We choose a tree with five branches (black circuit elements in Fig. A.1b) and four chords (gray circuit elements in Fig. A.1b). Each circuit element is labeled with an integer, to allow indexing of the voltage across (or current through) the element. Arrows indicate the defined direction of positive current flow.

Each chord completes a circuit loop, and Kirchoff's voltage law thus associates an equation with each of the chords. Take, for example, the chord associated with current I_6 . Addition of this chord to the tree creates a loop, with associated equation

$$V_3 + V_6 - V_1 - V_2 = 0. \quad (\text{A.1})$$

It is helpful to collect the equations for each chord in a matrix notation, writing

$$\mathbf{F}^T \mathbf{V}_b = \mathbf{V}_c, \quad (\text{A.2})$$

where the vectors \mathbf{V}_b and \mathbf{V}_c are the voltages of the branches and chords. For the network in

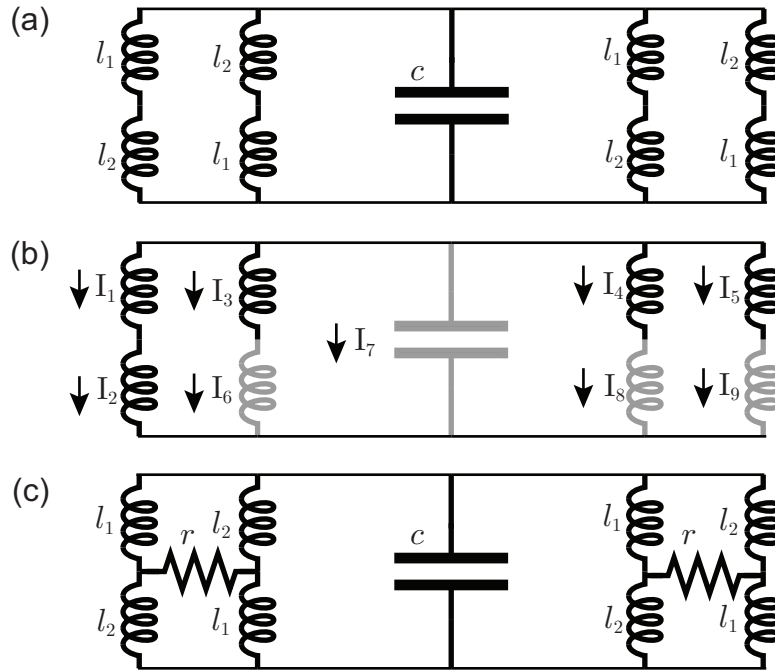


Figure A.1: (a) General form of the circuit depicted in Fig. 4.2b, isolated from any transmission lines (or equivalently, terminated in transmission lines of very large characteristic impedance). (b) The circuit in (a), with currents at each chord and branch labelled. Arrows indicate the (arbitrary) choice of direction for which current flow is positive. (c) The circuit in (a), connected to transmission lines of characteristic impedance r , as indicated by resistor symbols.

Fig. A.1b,

$$\mathbf{V}_b = \begin{bmatrix} V_1 \\ V_2 \\ V_3 \\ V_4 \\ V_5 \end{bmatrix}, \quad (\text{A.3})$$

$$\mathbf{V}_c = \begin{bmatrix} V_6 \\ V_7 \\ V_8 \\ V_9 \end{bmatrix}, \quad (\text{A.4})$$

and

$$\mathbf{F}^t = \begin{bmatrix} 1 & 1 & -1 & 0 & 0 \\ 1 & 1 & 0 & 0 & 0 \\ 1 & 1 & 0 & -1 & 0 \\ 1 & 1 & 0 & 0 & -1 \end{bmatrix}. \quad (\text{A.5})$$

This is convenient, as the deliberate manner in which the equations in Eq. (A.2) were collected ensures that the currents in the branches and chords satisfy a complementary equation,

$$\mathbf{F}\mathbf{I}_c = -\mathbf{I}_b. \quad (\text{A.6})$$

The next step is to relate the currents and voltages of the chords (branches) in the Laplace domain:

$$\mathbf{V}_b = \mathbf{Z}_b\mathbf{I}_b, \quad (\text{A.7})$$

$$\mathbf{V}_c = \mathbf{Z}_c\mathbf{I}_c.$$

In this example,

$$\mathbf{Z}_b = s \begin{bmatrix} l_1 & 0 & 0 & 0 & 0 \\ 0 & l_2 & 0 & 0 & 0 \\ 0 & 0 & l_2 & 0 & 0 \\ 0 & 0 & 0 & l_1 & 0 \\ 0 & 0 & 0 & 0 & l_2 \end{bmatrix}, \mathbf{Z}_c = \begin{bmatrix} sl_1 & 0 & 0 & 0 & 0 \\ 0 & 1/cs & 0 & 0 & 0 \\ 0 & 0 & sl_2 & 0 & 0 \\ 0 & 0 & 0 & sl_1 & 0 \end{bmatrix}. \quad (\text{A.8})$$

Eqs. A.2, A.6, and A.8 may now be combined into a single matrix equation:

$$\mathbf{F}\mathbf{I}_c = -\mathbf{I}_b, \quad (\text{A.9})$$

$$\mathbf{F}\mathbf{Z}_c^{-1}\mathbf{V}_c = -\mathbf{Z}_b^{-1}\mathbf{V}_b,$$

$$\mathbf{F}\mathbf{Z}_c^{-1}\mathbf{F}^T\mathbf{V}_b = -\mathbf{Z}_b^{-1}\mathbf{V}_b,$$

$$(\mathbf{F}\mathbf{Z}_c^{-1}\mathbf{F}^T\mathbf{V}_b + \mathbf{Z}_b^{-1})\mathbf{V}_b = 0,$$

$$(\mathbf{F}\mathbf{Z}_c^{-1}\mathbf{F}^T\mathbf{V}_b\mathbf{Z}_b + \mathbf{1})\mathbf{V}_b = 0.$$

Here, $\mathbf{1}$ is the identity matrix and the superscripts denote matrix inversion. By the invertible matrix theorem, the determinant of the matrix on the left-hand side must vanish for a non-trivial solution. The requirement that,

$$\text{Det}[\mathbf{F}\mathbf{Z}_c^{-1}\mathbf{F}^T\mathbf{V}_b\mathbf{Z}_b + \mathbf{1}] = 0. \quad (\text{A.10})$$

yields a characteristic equation in s , the roots of which are the eigenfrequencies of the network. In this example, those frequencies are

$$\begin{aligned} s_1 &= i\sqrt{\frac{2(1-\delta^2)}{lc}}, \\ s_2 &= s_1^*. \end{aligned} \quad (\text{A.11})$$

when the inductances l_1 and l_2 are parametrized according to Eq. (4.2). Here the $*$ indicates complex conjugation.

If the same process is repeated for the network in Fig. A.1c, and an expansion is performed to second order in δ and first order in $1/r$, the resulting eigenfrequencies are

$$\begin{aligned} s_1 &= -\frac{r}{l}, \\ s_2 &= -\frac{r}{l} + \frac{2\delta^2}{rc}, \\ s_3 &= -\frac{\delta^2}{rc} + i\sqrt{\frac{2}{lc}}\left(1 - \frac{\delta^2}{2}\right), \\ s_4 &= s_3^*. \end{aligned} \quad (\text{A.12})$$

The real and imaginary components of these eigenfrequencies indicate the dissipation and oscillation rates of the eigenmodes. Their quality factors are therefore the ratio of their imaginary and real parts. While the modes associated with s_1 and s_2 are purely dissipative, modes 3 and 4 have a linewidth that scales with the square of the imbalance in the bridges. Comparison with Eq. (A.11) shows that the imaginary components of the eigenfrequencies are Taylor expansions of the resistorless network's eigenfrequencies, to second order in δ .

Comparison with the group delay plotted in Fig. 4.2d can now be made. With $c = 1$ pF, $l_0 = 1$ pH, and $\delta = 0.2$, mode s_3 is resonant at 6.97 GHz and has an inverse linewidth of 1.25 ns, in agreement with the simulation.

Appendix B

Design rules of the NIST Nb trilayer process

Further details on the design space and design rules for the trilayer process are catalogued in Tab. [B.1](#).

Table B.1: Layer names, abbreviations and associated design rules for the NIST niobium trilayer process.

layer	notes	design rules
CE		minimum width is $2.5 \mu\text{m}$ minimum space (from other CE features) is $2 \mu\text{m}$ must be overlapped by BE by $1.25 \mu\text{m}$ must be overlapped by AL by $1 \mu\text{m}$ must be overlapped by CEO by $0.5 \mu\text{m}$
CEO		minimum width is $3 \mu\text{m}$
AL	Thickness ranges from 6 to 10 nm.	minimum width is $4 \mu\text{m}$ must be overlapped by BE by $0.25 \mu\text{m}$ must be overlapped by ALO by $0.5 \mu\text{m}$

ALO		minimum width is 4.5 μm
BE	200 nm thick.	minimum width is 2 μm minimum space (from other BE features) is 1 μm
R1	Thickness ranges between 135 and 225 nm, allowing sheet resistances between 2 and 1.2 Ohms/square (AuPd) and 100 and 60 mOhms/square (Au). Au has stronger temperature dependence than AuPd—if this is an issue, and resistor footprint is not a constraint, interdigitation of AuPd resistors allows for fabrication of low-resistance, temperature-independent resistors.	minimum width is 2 μm minimum space (from other R1 features) is 4 μm minimum overlap with BE is 1 μm

I1	<p>Thickness ranges from 300 to 500 nm.</p> <p>Relative dielectric constant of SiO₂ is $\epsilon_r = 3.9$. Loss tangent is temperature and power dependent [144]. With high-power measurements of test resonators at 300 mK we estimate it to be 3×10^{-3}. SiN [144] and amorphous silicon [100] are reported to have lower loss tangents, though amorphous silicon has poor etch selectivity with Nb. This was only recently overcome [100].</p>	<p>must overlap with BE, CE, or W1</p> <p>minimum width is 0.8 μm in junctions</p> <p>minimum width is 1 μm otherwise</p> <p>must be overlapped by CE by 0.75 μm</p> <p>must be overlapped by BE by 1 μm</p> <p>must be overlapped by W1 by 1 μm</p>
W1	<p>When possible use BE for wiring, as the Nb in that layer is higher quality.</p>	<p>minimum width is 2 μm in junctions</p> <p>minimum space (from W1 features) is 1.5 μm</p> <p>minimum space (from BE edges) is 0.3 μm</p>
I2 or I1X	<p>400 nm thick. In practice, this is the layer that covers W1.</p>	
W2	<p>When possible use BE for wiring, as the Nb in that layer is higher quality.</p> <p>350 nm thick.</p>	<p>minimum width is 2 μm in junctions</p> <p>minimum space (from W2 features) is 1.5 μm</p> <p>minimum space (from BE edges) is 0.3 μm</p>

I2X	This is the layer that covers W2.	
-----	-----------------------------------	--

Appendix C

Measurement details

A detailed schematic of the experimental setup is shown in Fig. C.1. A single-pull double-throw switch, a cross-over switch (Pasternack PE7152), and a directional coupler (MAC C3205-20) allow for measurement of the four accessible scattering parameters with an Agilent ENA5071C network analyzer. For measurements of the transmission spectrum, a Tektronix RSA6100A spectrum analyzer serves as the microwave detector.

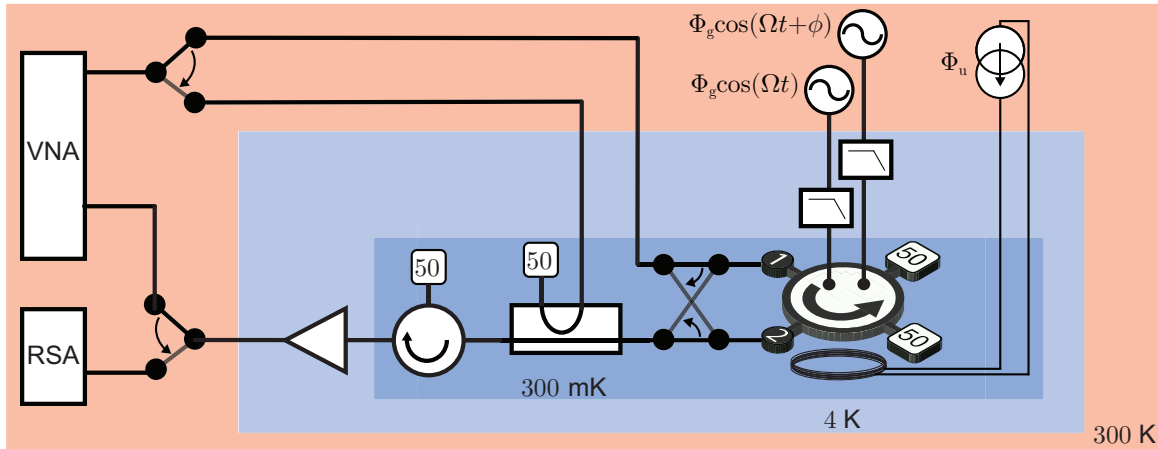


Figure C.1: Detailed experimental schematic for the measurements discussed in Ch. 5 and Ch. 6.

A Yokogawa 7651 current source provides the current for an off-chip, home-wound electromagnet, which creates the uniform flux Φ_u . A two-channel arbitrary waveform generator (Agilent 33500A), creates a pair of radio-frequency bias signals at frequency Ω , with phase difference ϕ , providing the gradiometric flux Φ_g .

Both (transmission and reflection) input lines are attenuated by 20 dB at the 4K plate, and an additional 20 dB at the 300 mK base plate of the ^3He cryostat, allowing for a noise temperature T_n as low as

$$\begin{aligned}
 T_n &> 300 \text{ K} \times 10^{-4} + 4 \text{ K} \times (1 - 10^{-2}) \times 10^{-2} + 300 \text{ mK} \times (1 - 10^{-2}) \\
 &\approx 370 \text{ mK}
 \end{aligned}
 \tag{C.1}$$

The probe signals are then routed to the microwave receiver, where they propagate through an isolator (Raditek RADC-4-8-Cryo-(30mK-4K)-S23-1WR-MS-b) and are amplified by a Caltech HEMT amplifier (CRYO 4-12) at 4 K and a room temperature amplifier (Miteq AMF-3F-04000800-07-10P). Bias lines are filtered with 350 MHz low-pass powder filters, and have a noise temperature of roughly 300 K.

Appendix D

Calibration of network parameter measurements

In this appendix we describe the calibration procedures used for analysis of the network parameter measurements described in Ch. 6.

D.1 Transmission calibration

To remove the gain of the measurement chain in transmission measurements, a bypass switch (formed from two Radiall 570443000 single-pull double-throw switches) is mounted at the base of the cryostat, which routes fields through a 5 cm SMA cable instead of the circulator. We also use dedicated through measurements, (made in a separate cooldown) in which the circulator chip is exchanged for a like-sized circuit board traversed by a single 50 Ohm transmission line. Using these techniques, the reference plane for transmission measurements is moved (approximately) to the edge of the chip.

D.2 Reflection calibration

To remove the gain G from reflection measurements, we measure the reflection R_{bal} off the circulator when no bias current is applied to the on-chip bias lines. In this unbiased state, all four inductor bridges are balanced, and the reflection coefficient Γ_{bal} is the diagonal entry in each row of the balanced scattering matrix \mathbf{S}_{bal} . The matrix \mathbf{S}_{bal} may be calculated by setting $\delta_0 = 0$ in Eq. (4.11) and substituting the resulting admittance matrix into Eq. (4.23). This procedure yields

$$\Gamma_{\text{bal}} = \frac{i\omega l + 2Z_0}{i\omega l - 4Z_0}. \quad (\text{D.1})$$

As

$$R_{\text{bal}} = G\Gamma_{\text{bal}}, \quad (\text{D.2})$$

and the gain G of the reflection measurement chain is assumed to be independent of the circulator's state, the reflection coefficient Γ_{op} at arbitrary operation points is related to the measured reflection R_{op} by

$$\Gamma_{\text{op}} = \frac{R_{\text{op}}}{G} = \Gamma_{\text{bal}} \frac{R_{\text{op}}}{R_{\text{bal}}}. \quad (\text{D.3})$$

To account for geometric inductance in the bridges, the inductance l in Eq. (D.1) is estimated using measurements of the unbalanced circuit's resonant frequency, the capacitance design value of 1 pF, and Eq. (4.7).

D.3 Calibration of group delay

Preparing the circulator for operation requires correctly setting the duration τ of the resonant delay. Measurements of the circulator's group delay are used for this purpose. To separate the non-resonant delays of the finite-length measurement chain from the resonant delay τ , we multiply the measured transmission data by $e^{i\omega\tau_d}$, where $\tau_d = 62$ ns is the time required for an off-resonant microwave field to propagate through the measurement chain. In the absence of circuit resonances, this multiplication makes the phase of the transmission flat as a function of frequency, zeroing the group delay.